Technische Universität München
Fakultät für Physik

Graduation paper from the Master of Science in Physics

Characterization of the Electron Response of a TRISTAN Silicon Drift Detector in the KATRIN Monitor Spectrometer

Charakterisierung der Elektronenantwort eines TRISTAN Silizium-Drift-Detektors im KATRIN Monitor-Spektrometer

Lena Elisa Johanna Wunderl
03670328

23 June 2022

Max-Planck-Institut für Physik

Abstract

Searching for the origin of dark matter requires some hurdles to overcome. One is, for example, to find out for which particle to search. A possible particle is a sterile neutrino. This would be the right-handed partner of the active neutrinos occurring in the standard model of particle physics. Active neutrinos are part of the current research with the KATRIN experiment. The KArlsruhe TRitium Neutrino experiment located in Karlsruhe searches for the effective electron neutrino mass by investigating the endpoint of the tritium β decay spectrum.

The TRitium Investigations of STerile to Active Neutrino mixing (TRISTAN) project will be the detector upgrade of the KATRIN experiment to enable it to search for keV sterile neutrinos. It will search for a kink-like imprint deep inside the tritium β decay spectrum. This kink would originate from a sterile neutrino that should mix with the active neutrinos. The target sensitivity for the mixing angle will be of the order of $\sin^2 \theta_{14} < 10^{-6}$ [1]. This requires high count rates, for which the current KATRIN detector is not designed. To be able to handle these high statistics, a new TRISTAN detector will be built in. It will consist of 21 modules each carrying 166 pixels, which can accommodate rates of up to 100 kcps. This detector is a silicon drift detector and is developed by the Semiconductor Laboratory of the Max Planck Society (HLL) [2].

The main aim of this thesis is to investigate a TRISTAN detector module with 47 pixels in the KATRIN monitor spectrometer in order to characterize the detector's electron response. The monitor spectrometer is a smaller version of the KATRIN experiment and works equally. This enables measurements under realistic conditions for the final operation in KATRIN, such as investigating electrons in a MAC-E filter environment. The cabling in the monitor spectrometer is similar to the final setup as well as the environment of the detector. It is surrounded by similar sensors and equipment such as vacuum pumps, temperature sensors, and analog electric and magnetic fields as in the final setup. The monitor spectrometer is a MAC-E filter and consists, among other things, of a spectrometer vessel surrounded by an air coil system, a magnetic system with two superconducting solenoids at the entrance and exit, and a high voltage supply to control the MAC-E filter. At the end, the detector is located. The electrons are guided adiabatically through the spectrometer by the MAC-E filter towards the detector. Two different calibration sources were used for this thesis, wall electrons and conversion electrons from a krypton source.

At first, a rough estimate of the detector response with wall electrons at different energies was carried out. The obtained data was calibrated with a special empirical model function considering dead layer effects. After the calibration, an empirical detector response was fitted to the energy spectra to determine parameters like the energy resolution. The FWHM values received are in the range between 300 eV to 400 eV for 30 keV electrons. For the electrons at 21 keV a FWHM of 336 eV was

determined. This energy resolution is worse than the required less than 300 eV at 20 keV for the TRISTAN detector. However, since the measurement was performed at 21 keV and in particular the detector was not cooled, the result is within the expected range.

The main analysis in this thesis was to test the feasibility of combining different datasets. For this purpose, a 66 h long time measurement consisting of 66 runs was performed with ^{83m}Kr.

First, the time stability was tested before stacking, then the characteristics of the detector response were determined with the empirical function after stacking the runs. It was found that the parameters with a deviation of the mean of less than 5 eV and of the FWHM of less than 3 eV were stable inside the precision. This small deviation led to the conclusion that stacking over time is possible and does not affect the fitting of the data and the mean energy resolution was with a value of (331.53 ± 0.06) eV FWHM even slightly better. For the TRISTAN project, it is important that the data can already be stacked before calibration, as this minimizes the computational effort. In addition, measurements are taken over a very long time, and the aim is to calibrate as rarely as possible.

The second step was to investigate the homogeneity among the 47 pixels. The peak positions of the L and the M line for the different pixels were about 1 keV distributed. Together with the high deviation of the FWHM of about 20 eV, it can be concluded that it is necessary to calibrate each pixel individually. Hence, the single spectra were calibrated before stacking. The reason why stacking the pixels is useful even after calibration is to reduce the free parameters and thus the computational time and effort. It was also recognized that the parameters have a large spread over the number of added pixels, which is why the reduced χ^2 deteriorates quickly during stacking. The final effective pixel had a FWHM of (335.3 ± 0.2) eV. After stacking the calibrated data of all pixels, it was found that the simple empirical model function no longer describes the data sufficiently well. One solution could be to group similar pixels or improve the empirical model.

Contents

1 Neutrino Physics

The neutrino is one of the most interesting particles because there are so many of them in the universe. It could explain some fundamental open questions, like why the universe looks the way it does, or what dark matter is. For this reason, we have to understand all features of this particle. The first chapter will give a rough overview of the theory of the neutrino. Then, after the active neutrinos are introduced, the sterile neutrinos and their meaning for the known physics will be explained shortly.

1.1 Active Neutrinos

Neutrinos are electrically neutral leptons that interact only via weak interaction. Leptons are a kind of elementary particles. As fermions, they have a half-integer spin. In the standard model, leptons are divided into three families. The three so-called neutrino flavors are the electron neutrino ν_e, the muon neutrino ν_μ and the tau neutrino ν_τ. Each of the neutrinos has an antiparticle [3].

1.1.1 Historical Overview

After it was found in 1930 by J. Chadwick [4] that the β decay produced a continuous spectrum contrary to expectations, the theory behind β decays was questioned. Two mono-energetic lines were expected in the case of β decay since a two-body decay was assumed. The obtained continuous spectrum led to two possible conclusions. Either the conservation of energy and angular momentum was violated, or a third particle existed, which could not be detected yet. To save the law of conservation of energy and the law of conservation of angular momentum, two of the cornerstones of physics, Wolfgang Pauli postulated the third particle in the β decay, later called the neutrino. [5]

The name was suggested by Enrico Fermi, who also proposed the first draft of a theory on the weak interaction [6]. Today it is known that in beta decay the neutron n decays into an electron e^- and an electron antineutrino $\bar{\nu}_e$, while in the process a

proton p is produced as shown in equation 1.1.

$$n \rightarrow p + e^- + \overline{\nu}_e \tag{1.1}$$

After a first hint in the experiment performed at Hanford in 1953, Cowan and Reines confirmed the existance of a neutrino with this experiment in the Savannah River Plant of the U.S. Atomic Energy Comission in 1956 [7]. The neutrinos were detected via inverse β decay (see equation 1.2 and section 1.1.3 for more information about the detection) and came from an intense neutrino flux from a nuclear reactor [7].

$$\overline{\nu}_e + p \rightarrow e^+ + n \tag{1.2}$$

1.1.2 Neutrinos in the Standard Model of Particle Physics

The standard model of particle physics summarises all known elementary particles and interactions. Among matter particles, a distinction is made between quarks and leptons [8]. Leptons are classified in three flavors: the electron e, the muon μ, and the tau τ. Each particle has an associated neutrino, the electron neutrino ν_e, the muon neutrino ν_μ and the tau neutrino ν_τ. These neutrinos do not interact via the strong or electromagnetic interaction. [9]
The neutrinos in the standard model only occur left-handed [10]. The reason is that the exchange particles of the weak interaction only couple on left-handed particles and right-handed antiparticles. It is unusual that there is only the left-handed particle, as particles typically occur in left- and right-handed states. Without the right-handed partner, the neutrino does not have a Dirac mass term m_D and therefore is massless [11]. In this case, the handedness is equal to the helicity. The helicity is the spin projection onto a particle's momentum vector. This means that the spin is either parallel or antiparallel to the momentum. [8]

1.1.3 Neutrino Mass

Going beyond the standard model of particle physics, it can be recognized that the neutrino must have a mass after all.
Between 1970 and 1992, one of the first experiments investigating the neutrinos was the Homestake experiment [12]. Its purpose was the observation of the total solar neutrino flux via the inverse β decay. The detection method was based on equation 1.3.

$$^{37}Cl + \nu \rightarrow e^- + \,^{37}Ar \tag{1.3}$$

Solar neutrinos are produced in the Sun by different reactions in the pp chains and CNO-cycle. It is important to mention that only electron neutrinos are produced

during these production cycles. [8]

In solar neutrino experiments like Homestake, lower rates in the solar electron neutrino flux than expected were detected. However, different deficits were found in different experiments, which suggests that the effect could be energy-dependent. This finding was called the solar neutrino problem, and the solar model was questioned. [13]

The Sudbury Neutrino Observation (SNO) experiment solved the problem by measuring all neutrino flavor fluxes via the neutral current interaction [14]. For the weak interaction, there exist two channels. One is the charged current interaction in which charges are exchanged via the W^+ or W^- bosons. With this channel, the electron neutrino flavor can be evidenced. The other interaction is via the neutral current. Here the Z boson works as a mediator without exchanging any current. The neutral current can be used to detect all neutrino flavors simultaneously.

The total measured neutrino flux agrees with the predictions of the Standard Solar Model, but the simultaneously measured electron neutrino flux rate is still lower than expected.

From this, it can be deduced that the electron neutrinos change their flavor on the way from the Sun to the Earth and can only be measured as muon or tau neutrinos via the neutral current as part of the total neutrino flux. This flavor oscillation has also been confirmed by experiments with atmospheric neutrinos, as in Super Kamiokande [15], with reactor neutrinos, as in Daya Bay [16], and with accelerator neutrinos, as in T2K [17].

It can be concluded that the electron neutrinos The change of neutrino flavor is called neutrino oscillation. These oscillations are time-periodic transitions [3]. With oscillation experiment one can only investigate mass differences and not absolute masses, but so it has been used to prove that at least two of the three known neutrinos must have a mass. Because the prerequisite for neutrino oscillations is the existence of neutrino mass eigenstates m_i ($i = 1, 2, 3$) which describe the propagation in the vacuum [3]. These mass eigenstates are not identical to the flavor eigenstates. In general, the mass eigenstates are a linear superposition of the flavor eigenstates and vice versa. This is illustrated in figure 1.1. Here, on the left side, the flavor composition of the three neutrino mass eigenstates is outlined. The different colors represent the flavor eigenstates and the boxes the mass eigenstates. The wider the colored bar inside the box, the more likely it is to find the corresponding flavor neutrino. On the right hand, the flavor eigenstates are represented by the big boxes, while the boxes with different grey shades represent the mass eigenstates. For this scenario, the normal mass hierarchy is assumed, meaning that $m_3 > m_1$. However, it is unclear if this is the correct order of the mass values because in neutrino oscillation experiments only the mass differences Δm^2 can be measured. Equation 1.4 describes
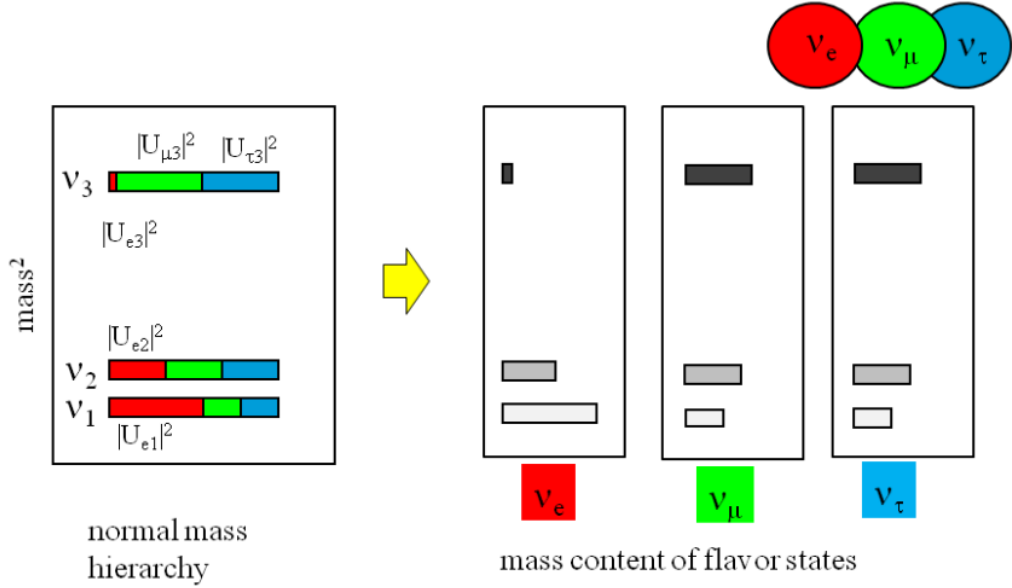
Figure 1.1: Illustration of the superposition of the neutrino flavor and mass eigenstates. The superposition of the flavor eigenstates (colored) building the mass eigenstates (boxes) is shown on the left side. The normal mass hierarchy is assumed. On the right side, the reverse scenario can be seen. The boxes present the mass eigenstate components of the flavor eigenstates in different shades of grey. The figure is taken from [18].

this mixing of the flavor and mass eigenstate.

$$\nu_\alpha = \Sigma_{i=1}^{3} U_{\alpha i} \nu_i \tag{1.4}$$

In the equation, ν_α stands for the flavor eigenstate of the neutrino, where α indicates the exact flavor (e, μ, τ). It results from the sum of the three mass eigenstates (ν_1, ν_2, ν_3) multiplied by the corresponding entry of the neutrino mixing matrix. This matrix is called Pontecorvo, Maki, Nakagawa, Sakata (PMNS) matrix U (see equation 1.5) and shows the relationship between the flavor and mass eigenstates [3].

$$\begin{pmatrix} \nu_e \\ \nu_\mu \\ \nu_\tau \end{pmatrix} = \begin{pmatrix} U_{e1} & U_{e2} & U_{e3} \\ U_{\mu1} & U_{\mu2} & U_{\mu3} \\ U_{\tau1} & U_{\tau2} & U_{\tau3} \end{pmatrix} \begin{pmatrix} \nu_1 \\ \nu_2 \\ \nu_3 \end{pmatrix} \tag{1.5}$$

In the case of two neutrino flavors, the resulting equation with the entries from the PMNS matrix is shown in equation 1.6.

$$\begin{pmatrix} \nu_e \\ \nu_\mu \end{pmatrix} = \begin{pmatrix} \cos\theta & \sin\theta \\ -\sin\theta & \cos\theta \end{pmatrix} \begin{pmatrix} \nu_1 \\ \nu_2 \end{pmatrix} \tag{1.6}$$

The transition probability from one flavor to another thus results in equation 1.7.

$$P_{\alpha \to \beta} = \sin^2(2\theta)\sin^2\left(\frac{1.27\Delta m^2[eV^2]L[km]}{E_\nu[GeV]}\right) \tag{1.7}$$

Here E_ν is the neutrino energy, θ is the mixing angle between the flavor eigenstates, Δm^2 is the difference of the squared masses of the eigenstates and L is the length of the path travelled [14]. From this it can be concluded that the oscillation probability is dependent on the mass difference of the mass eigenstates. In the case of three flavors, we learn that at least two neutrinos must have a mass. In the standard model of particle physics, the neutrinos do not have a mass, as explained in section 1.1.2.

A small extension of the standard model makes it possible to construct mass terms for the neutrinos. The lorentz invariant solution of the relativistic Dirac equation 1.8 is a wave function ψ.

$$\left(i\gamma_\mu \frac{\partial}{\partial x_\mu} - m\right)\psi = 0 \tag{1.8}$$

In this formula the index is $\mu = 1, ..., 4$, $x = (x_1, x_2, x_3, x_4) = (t, \mathbf{x})^3$ is a four vector, m is the rest mass and can take on any values. The four-component spinor ψ represents the wave function and solves the Dirac equation as a plane wave function with the four-momentum vector $p = (E, \mathbf{p})$. It depends also on the four-dimensional space-time vector $x = (t, \mathbf{x})$ and the energy $E = \sqrt{p^2 + m^2}$. The solution is shown in equation 1.9.

$$\psi(x) \propto \begin{pmatrix} u \\ (\eta\sigma)u \end{pmatrix} e^{-ipx} + \begin{pmatrix} (\eta\sigma)v \\ v \end{pmatrix} e^{+ipx} \tag{1.9}$$

Here $\eta = \mathbf{p}/E + m$ and σ are two-dimensional Pauli matrices. The first term represents the particle, the second the corresponding antiparticle state. This wave function gives the solution for the propagation of free neutrinos with a fixed mass through time and space. The eigenstates of mass must solve the relativistic Dirac equation. For a Dirac neutrino mass generated by the Higgs mechanism, the mass term of the Lagrange density L_D follows equation 1.10.

$$L^D = -\Sigma_{\alpha,\alpha'}\overline{\nu}_{\alpha R}M^D\nu_{\alpha' L} + h.c. \tag{1.10}$$

Here M^D is a complex 3×3 matrix and $\alpha' = e, \mu, \tau$. Since here both the left-handed and the right-handed partner couple to the Higgs field, the existence of the right-handed singlet field $\nu_{\alpha R}$ is decisive. The right handed field does not occur in the

standard Lagrange function of the weak interaction and therefore does not interact at all. Such a hypothetical particle is called sterile neutrino (see section 1.2).

A second possibility to extend the standard model and construct mass terms is for the approach of Majorana neutrinos, where the neutrino would be its own antiparticle. Here the right-handed singlet field $\nu_{\alpha R}$ is replaced by the antineutrino in the standard model. This violates the total lepton number conservation because the neutrino would be its own antiparticle and would only be possible for neutrinos because they carry no charge. [3]

However, it is not yet clear if the neutrino is a Dirac or a Majorana particle and which mass hierarchy, the normal one ($m_3 > m_1$) or the inverted one ($m_1 > m_3$), they follow because we do not know the absolute mass scale. In current experiments, mass limits are investigated for both the Dirac and the Majorana cases. The LEGEND experiment, for example, sets a mass limit for the effective Majorana mass m_M by trying to find the neutrino-less double β decay. More information on the LEGEND experiment can be found in [19]. Another experiment investigating the effective electron neutrino mass is the KATRIN experiment by looking into the β decay spectrum of tritium. It has only recently derived an upper limit for the effective neutrino mass of $m_\nu < 0.9\,\text{eV}$ (90% C.L.). This experiment will be shortly explained in section 2.

1.2 Sterile Neutrinos

As mentioned above, the neutrino mass can be derived by introducing a right-handed neutrino as an expansion to the standard model. Because they are not even interacting weakly, they are called sterile neutrinos. However, an advantage would be the mixing with the active neutrinos, which would make it possible to detect them. This detection could solve problems in particle physics and cosmology, as will be explained in the next section.

1.2.1 Light and Heavy Sterile Neutrinos

As derived in section 1.1.3, the mass of a sterile neutrino could have almost any value. The transition of an active (left-chiral) to a sterile (right-chiral) neutrino is described by the Fermion mass terms. The Lagrangian $\mathcal{L}$ can consist of more than one mass term. For the Dirac mass m_D the Lagrangian part $\mathcal{L}_D$ is shown in equation 1.11.

$$\mathcal{L}_D = -m_D \left(\overline{\nu_L} \nu_R + \overline{\nu_R} \nu_L \right) \tag{1.11}$$

If the Lagrangian also includes a Majorana mass term, it could follow equation 1.12.

$$\mathcal{L}_M = -\frac{1}{2} m_T \left(\overline{\nu_L} \nu_L^c + \overline{\nu_L^c} \nu_L \right) - \frac{1}{2} m_S \left(\overline{\nu_R} \nu_R^c + \overline{\nu_R^c} \nu_R \right) \tag{1.12}$$

Here, ν_L^c is the charge conjugated active neutrino field and ν_R^c is the charge conjugated sterile neutrino field. m_T is the Majorana mass of the active neutrino, while m_S is the Majorana mass of the sterile neutrino. Both terms, Dirac and Majorana mass, can contribute in the Lagrangian at the same time. If the sterile neutrino mass, represented by the singlet mass $m_S = 0$, the neutrino would be a pure Dirac particle [10]. The right-handed singlet field would not interact in the standard model except with an extremely small Higgs-Yukawa coupling. Another possibility is a Dirac mass of $m_D = 0$, which would make the neutrino a pure Majorana particle and enables it to take any mass value. It could not be detected because it would neither interact nor mix with the active neutrinos. A third possibility would be the case that $m_S << m_D$. This is called the pseudo-Dirac limit and is considered as a perturbation in the Dirac case. Lastly, the approach $m_S >> m_D$ and $m_T = 0$ is presented. Here a Dirac mass eigenstates of an active light neutrino and a Majorana eigenstate of a heavy sterile neutrino would exist. This is called the (minimal type-I) seesaw Limit [20]. The masses would be estimated via equations 1.13 and 1.14.[10]

$$|m_1| \sim \frac{m_D^2}{m_S} \tag{1.13}$$

$$m_2 \sim m_S \tag{1.14}$$

These mixed mass terms originate from the seesaw mechanism. This theory makes it able to treat the mass of the singlet neutrino m_S as a free parameter. In this model, right-handed neutrino fields ν_R are added to the standard model and couple to the left-handed, standard model neutrinos. This coupling happens in the same way as for charged particles [10]

Because the sterile neutrino mass can take any value, only a few important mass scales are shortly analyzed. The first and lowest range is $m_S = O(eV)$. In this case, the expected mixing of active and sterile neutrinos with the same chirality does not occur for pure Dirac or Majorana particles or the conventional seesaw mechanism. A reasonable approach would be the minimal mini-seesaw that relates the mixing angle and the masses ($m_T = 0$ und $m_D << m_S \sim O(eV)$). Sterile neutrinos in this or higher ranges would leave a kink or lines in, e.g., the β decay. The next range is the $m_S = O(keV)$ range that will be explained in more detail in section 1.2.2. Another possible energy range is $m_S = O(MeV - TeV)$. From astrophysics, many constraints were already made, mainly by investigating weak decays and same-sign dilepton production at the LHC. For masses higher than the TeV range ($m_S >> TeV$), the Yukawa coupling of the sterile neutrino would be comparable with the coupling of quarks and charged leptons. Here, the canonical minimal type-I seesaw range would take effect. The last range treated here is $m_S \sim M_P$, where the mass of the sterile neutrino would be on the Planck scale of $M_P \sim 10^{19}\,GeV$.

Also, in cosmology, there is some motivation to search for a sterile neutrino on

different mass scales. In mass ranges of $m_S = O(eV)$ the sterile neutrinos could be produced together with the active neutrinos in the early universe. With the photons and the active neutrinos, relativistic sterile neutrinos could contribute to the radiation content. The matter density could be influenced by non-relativistic sterile neutrinos and therefore left an imprint in structure formation. [10]

A motivation for sterile neutrinos in the $m_S = O(keV)$ range will be described in section 1.2.2. In the $m_S = O(MeV - TeV)$ range, the sterile neutrinos could be created by mixing with the active neutrino in the early universe and decayed into lighter neutrinos. For a higher mixing angle, the heavier sterile neutrinos reach equilibrium before decoupling at higher temperatures than active neutrinos. For smaller mixing angles, the sterile neutrinos could be produced via decoherence on the generation process of active neutrinos. [10]

The mass range $m_S >> GeV$, meaning TeV, sterile neutrinos could explain the matter-antimatter asymmetry in our universe. Cosmological short-living neutrinos decay and leave C and CP violations caused by a cosmic lepton asymmetry. This violation would suggest more than one sterile neutrino. For decay during the primordial nucleosynthesis, that means before decoupling of the active neutrinos, the lepton asymmetry could be converted to the baryon asymmetry and therefore explain the over-occurrence of matter. [10]

1.2.2 Sterile Neutrinos on the keV-Scale

Sterile neutrinos in the $m_S = O(keV)$ are of special interest in physics. They could explain the origin and composition of dark matter [10]. However, they are only suitable for the case when their production is via the active-sterile mixture and the weak interaction [21].

A distinction is made between two cases of dark matter, depending on their cosmological production. Warm or moderate cool dark matter could be produced from relativistic sterile neutrinos that cool down and become non-relativistic during the radiation dominated universe. This dark matter could explain the low-scale structures that are observed. [10]

A minimal extension of the standard model is called the neutrino minimal standard model (νMSM) and would only need three sterile neutrinos. One would need to be in the keV mass range to produce dark matter, and two could be much heavier to give the active neutrinos their mass via the seesaw mechanism. [10]

Sterile neutrinos would not be absolutely stable. They could decay in a lighter, active neutrino through mixing. A controversial hint to such a decayed sterile neutrino could be found in a stacked XMM-Newton spectrum of 73 galaxy clusters [22]. Here an unidentified emission line was found at about 3.56 keV, and a mixing angle of about 10^{-11} could be concluded. Further research will explore if this line exists and could come from a sterile neutrino. Another explanation for the emission line could

be that they come from a complex of K XVIII lines around 3.5 keV. These lines are emission lines of the element potassium. [23]

In addition to this detection method, sterile neutrinos are also searched for in other ways. The various experimental possibilities are described in section 1.2.3.

1.2.3 Experimental Searches

Although the right-handed neutrino carries no charge and therefore does not participate in any interaction, it can still be detected because of its mixing with the active neutrinos. This detection can happen in three different ways.

The first option is indirect detection. Here, the already mentioned XMM-Newton spectra are based on. It is searched for hints of a decay line of a sterile neutrino. [24]

The second option is direct detection. Experiments like MiniBooNE [25], investigate the disappearance of an active neutrino flavor into a sterile neutrino flavor at high Δm^2 [26]. Another possibility of direct detection is an inelastic scattering of the sterile neutrino at bound electrons. Experiments such as XENON1T and DARWIN focus on this approach [21]. In experiments like DUNE [27] the area behind the β decay spectrum is investigated to look for a peak caused by an inverse β decay with a sterile neutrino.

The third way of detecting sterile neutrinos could be the production of this particle. During β decay, an energy that can be large enough to produce a sterile neutrino mass eigenstate is released. This signal could be detected because of the deformation of the β decay spectrum. It is a weighted superposition of the single neutrino mass eigenstates of the electron neutrino flavor, as explained in section 1.1.3. In theory, the electron neutrino flavor should also consist of a portion of the sterile neutrino mass in the keV range. Therefore, it should be detectable in the β decay spectrum [21]. Further information on the TRISTAN experiment that will use these techniques and the imprint of the sterile neutrino in the β decay spectrum is given in section 3 and section 3.1, respectively.

2 The KATRIN Experiment

KATRIN stands for KArlsruhe TRItium Neutrino experiment and is located at the Karlsruhe Institute of Technology (KIT). Its main goal is the measurement of the effective electron neutrino mass by examining the endpoint of the tritium β spectrum. The KATRIN collaboration consists of over 150 scientists, engineers, technicians, and students from a total of "12 institutions in Germany, the United Kingdom, the Russian Federation, the Czech Republic, and the United States" [28].

This chapter will give a short overview of the KATRIN experiment. First, the experimental setup will be described in section 2.1. Then the measuring method used in KATRIN will be explained in section 2.2.

2.1 Experimental Overview

An overview of the experiment with its sectors is shown in figure 2.1. The KATRIN experiment has a total length of 70 m beamline. For the investigation of the tritium β decay spectrum, the experiment uses a gaseous T_2 source [29]. Five main systems build the experiment and will be shortly explained in the following. The electrons are guided from the left side, upstream, to the right side, downstream.

Windowless Gaseous Tritium Source

The windowless gaseous tritium source (WGTS) is situated in the source system of the experiment. Here, up to 10^{11} tritium β electrons are produced per second with very high stability. The tritium is located in a source magnet cryostat with a source tube of 10 m length. Also, the rear wall (RW), the β-Induced X-Ray Spectroscopy (BIXS) system, and the tritium inner loop system are present. The BIXS is used to monitor the tritium source strength. Inside the inner loop system, up to 40 g of pure tritium are processed per day. [30]

The T_2 gas injected into the loop system is continuously directed to the center of the source system, where it arrives cold. The gas diffuses in both directions, hitting the
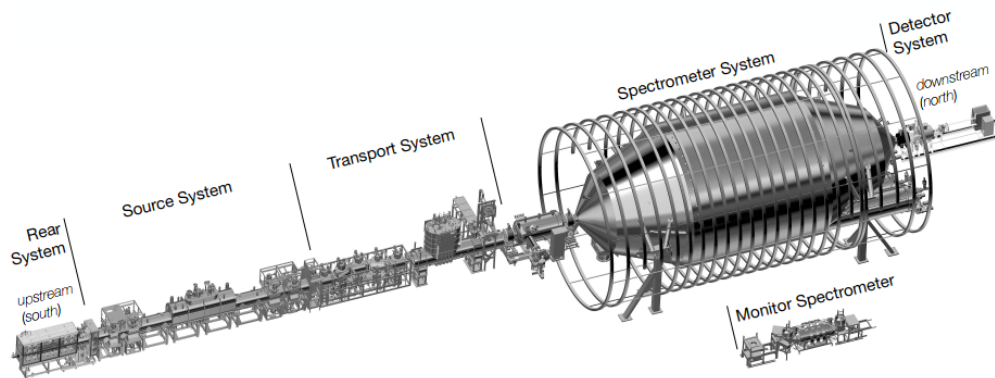
Figure 2.1: Overview of the KATRIN experiment. The different sections are marked. The monitor spectrometer is described in section 4. The electrons are guided from the source section towards the detector section. Figure taken from [30].

first pumping stages downstream. On the way, part of the T_2 molecules decay via β decay inside the source beam tube, releasing β electrons isotropically. [29]

Transport Section

The generated β electrons emitted in the downstream direction are guided adiabatically by magnetic field lines. They follow their way through two pumping stages from the source to the spectrometer [29].
These pumping stages reduce the flux of neutral tritium by about 14 orders of magnitude to reduce the background rate of the detector caused by tritium decaying in the main spectrometer (MS). This rate is set to be less than 1×10^{-3} cps. Therefore the first pumping stage, the Differential Pumping Section (DPS), is a combination of turbo-molecular pumps (TMPs) and reduces the flux by about 5 orders of magnitude. The second pumping stage is the Cryogenic Pumping Section (CPS). This aims to reduce the flux by a further 7 orders of magnitude. It uses a cold argon frost system at 3 K to 4 K to absorb the tritium [30].

Spectrometers

The electrons from the transport section encounter a tandem-spectrometer pair with large volumes. These spectrometers are based on the magnetic adiabatic collimation with electrostatic filter (MAC-E filter) principle [29].
The working principle of a MAC-E filter is shown in figure 2.2. Here the blue lines show the course of the magnetic field lines inside the vessel that guide the electrons
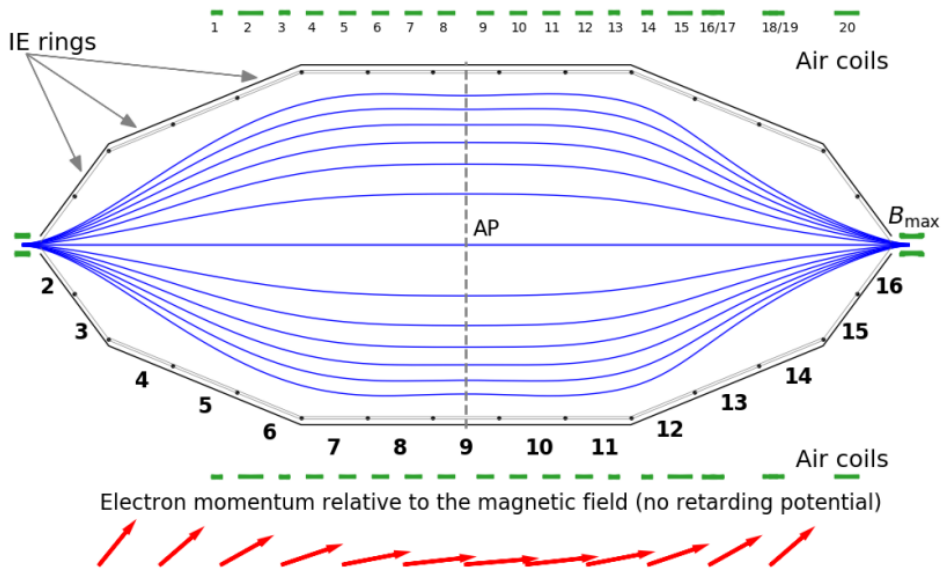
Figure 2.2: Sketch of the main spectrometer of the KATRIN experiment. It works according to the MAC-E filter principle. A high magnetic field at the tritium source guide the electrons into the spectrometer on the left. Inside the spectrometer, they are guided adiabatically along magnetic field lines. These magnetic field lines are shown in blue. In the center of the spectrometer, the magnetic field is small to reach this adiabatic motion. The red arrows at the bottom show the electron momentum's evolution. They follow this course because of the conservation of the orbital magnetic moment. It only occurs like this without an applied retarding potential. The dashed grey line marks the point where the momentum is almost aligned with the magnetic field lines. Two superconducting magnets (green, on the left and right) influence the course of the magnetic field lines. One magnet is located at the entrance and one at the exit of the spectrometer. 20 air coils surround the vessel. They are shown in green bars over and under the tank. The figure is taken from [31].

adiabatically through the tank from the entrance magnet to the exit magnet that define the magnetic field inside the monitor spectrometer. On their way along the magnetic field lines, the electrons also follow a cyclotron motion around those lines [32]. The magnetic field strength B decreases towards the center of the spectrometer tank to reduce the kinetic energy of the electrons perpendicular $E_\perp$ to the magnetic field lines [29]. The orbital magnetic momentum μ in equation 2.1 in the

non-relativistic limit is then conserved for an adiabatic motion of the electron.

$$\mu = \frac{E_\perp}{B} \tag{2.1}$$

Due to the conservation of the total kinetic energy E_{tot}, see equation 2.2, there is an acceleration for large incident angles, mainly on the parallel kinetic energy component $E_\parallel$ of the electrons.

$$E_{tot} = E_\perp + E_\parallel \tag{2.2}$$

The incident angle θ describes the angle between the magnetic field B and the electric momentum **p** at the starting point of the electrons. With equation 2.3, the parallel energy component of the total energy can be calculated for different incident angles [29].

$$E_\parallel = E_{tot} \cdot \cos\theta \tag{2.3}$$

The minimum of the magnetic field is at the same position where the perpendicular kinetic energy of the electrons reaches its minimum if no electric field is applied to the vessel. The value of the minimal magnetic field is typical of the order of 1 mT. For high voltages U applied on the spectrometer vessel, an energy threshold of qU can be set. Here q is the charge of one electron, and the typical setting of the high voltage U is 18.6 kV because it is close to the endpoint of the tritium β decay spectrum. While the magnetic field in the center of the spectrometer becomes minimal, the potential here reaches its maximum. This so-called analysing plane works as a barrier for the incoming electrons with kinetic energies $E_\parallel < qU$. [29] Equation 2.4 gives the filter width ΔE of the spectrometer with the minimal magnetic field B_{min} setting used in the spectrometer and the maximal magnetic field B_{max} setting applied at the exit magnet.

$$\Delta E = \frac{B_{min}}{B_{max}} \cdot E \tag{2.4}$$

The electron is transmitted with energy E [29].

The first spectrometer in the KATRIN experiment is the pre-spectrometer (PS). Its retarding voltage is set to -18.3 kV to reject all electrons from the tritium source that are not in the region of interest. This region is situated near the endpoint E_0 of the tritium β decay spectrum [29]. A low magnetic field of about 20 mT is present in this pre-spectrometer that transport the electrons adiabatically in each retarding potential setting [30].

The main spectrometer (MS) has a design filter width of $\Delta E = E \cdot 0.3\,\text{mT}/6\,\text{T} \approx 1\,\text{eV}$ for energies in the region of interest. By scanning the retarding potential U in this region, the β spectrum can be measured. A high-precise, high voltage supply

produces it. This device comes with a distribution and monitoring system. This ensures high stability and precision of the voltage in the spectrometer tank and the inner electrode (IE) until the ppm level of 10^{-6}. This inner electrode system takes care of the fine-shaping of the retarding potential profiles along the symmetry axis of the spectrometer to ensure the needed transmission properties. Both the cylindrical part of the vessel and the inner electrode carry a homogeneous potential to minimize the magnetic field along the analyzing plane. The resulting gradients of the magnetic fields need to be small to guarantee an adiabatic motion of the electrons. [29]

It is necessary to obtain high statistics for a precise measurement of the shape of the tritium endpoint but only a small number of electrons can reach the detector via the retarding potential. These high statistics can be obtained by increasing the activity of the tritium source. The luminosity is, however, limited by the electron scattering in the source. Another way to improve the measurement quality is to reduce background. Electrons colliding with residual gas in the main spectrometer can be prevented by applying a vacuum of 10^{-11} mBar [29].

A system of air-cooled magnet coils (air coils) surrounding the main spectrometer allows for fine-tuning the magnetic field. A high-sensitive Magnetometer system monitors the magnetic fields at different external positions during the measurement. [29]

Detector section

The electrons enter the detector section by leaving the spectrometer through the exit magnet. The Focal Plane Detector (FPD) lying here counts all arriving β and background electrons coming from the main spectrometer. It can handle high count rates of 1 Mcps order of magnitude distributed over the entire detector. In addition to systematic investigations of the entire KATRIN experiment, it is also used for tests and calibration measurements with other sources like ^{83m}Kr. Also, time resolutions of < 100 ns for time-of-flight mode measurements are possible. [10]

Rear system

Lastly, the rear system is located at the beginning, meaning upstream of the source system. An electron gun is placed in this section for calibration measurements and monitoring purposes. A superconducting magnet guides the electrons from the electron gun in the WGTS. Important operation parameters like the composition of the source gas, the source activity, and the main spectrometer's high voltage stability can be monitored with its help. [30]

2.2 Neutrino Mass Mode

The standard operating mode of the KATRIN experiment is the neutrino mass mode. In this mode, the retarding voltage of the main spectrometer can be adjusted in the range of $[E_0 - 40\,\text{eV}; E_0 + 50\,\text{eV}]$ [30] while tritium is injected in the source section. The Measurement Time Distribution (MTD) defines the voltage and time spent in each setting. A single run is typically lasting between 20 s and 600 s, which leads to a total scan at all energies in the range of about 2 h [30].

For analyzing the energy of the β electrons with a resolution of about 1 eV in this mode, the energy resolution is set to 2.77 eV for 18.6 keV electrons in the main spectrometer. Energy discrimination on a similar level presupposes a sensitivity to the neutrino mass of less than this 1 eV. [29]

The statistical sensitivity can be improved by modifying the nominal magnetic flux inside the spectrometer. Also, to reduce the background of a factor of 2, the maximum of the absolute retarding potential and the minimal magnetic field are shifted towards the detector. [30]

An example of the integrated spectrum investigated by KATRIN in the neutrino mass mode is shown in figure 2.3.

The mass distribution between the three light neutrino mass eigenstates is too
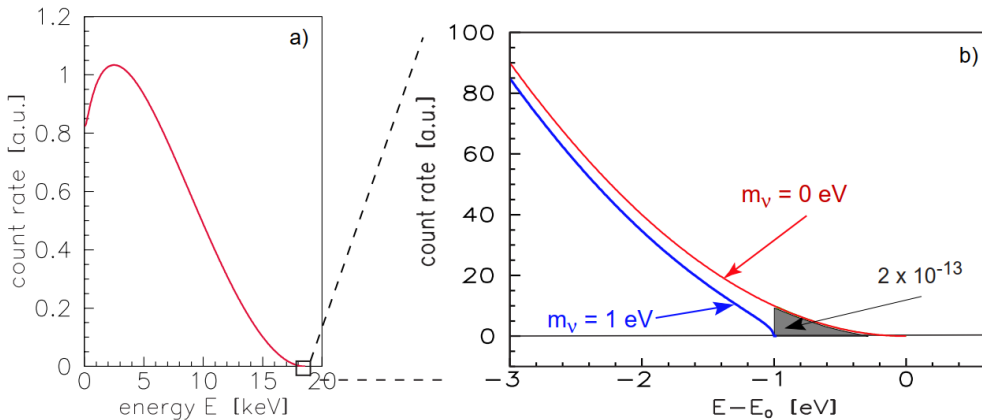
Figure 2.3: Figure taken from [33] a) shows the entire energy spectrum of the tritium β decay. b) is a zoom into region around the endpoint E_0. The effective neutrino mass m_ν is given for 0 eV in red and for 1 eV in blue.

small to be resolved in any current experiment. The KATRIN experiment, searches therefore for lower limits for the effective light neutrino mass (see equation 1.4). A small part of this standard neutrino mass mode runs are used to search for sterile neutrinos. However, since this search involves scanning in much deeper areas of

the spectrum, in the keV range, a new detector system is currently being developed to replace the Focal Plane Detector in the future. This new detector system will be introduced in section 3.

3 The TRISTAN Project

3.1 Sterile Neutrino Search in Tritium β Decay

One possibility to search for sterile neutrinos in the keV mass range is via single β-decay. Here a neutron n decays, into a proton p and an electron e^- emitting an electron anti-neutrino $\bar{\nu}_e$

$$n \rightarrow p + e^- + \bar{\nu}_e. \qquad (3.1)$$

A good candidate for this is the spectrum of the beta decay of tritium. The energy of the emitted electron is measured, and the number of electrons with respect to their energy are counted. From this, one obtains the energy spectrum. [3]
As explained in Section 1.1.3, the spectrum of each mass eigenstate (m_1, m_2, m_3) of the neutrinos is weighted by the mixing amplitude $|U_{ei}|$ of the electron flavor. These single spectra are superimposed and form the β spectrum. If there was a (right-handed) sterile neutrino ν_s with an associated mass m_s in the keV mass range, then also the electron neutrino would contain a small admixture of the new mass eigenstate m_4. This mixture would contribute to the overlaid β spectrum resulting in a kink-like imprint inside the spectrum. In the case of a neutrino in the keV mass scale, this kink-like imprint can be much deeper inside the spectrum than the imprint of the neutrino mass of the active neutrinos in the endpoint region of the spectrum. For this, the whole spectrum should be investigated. Such a kink-like imprint is shown in figure 3.1 with an exaggerated mixing angle of $\sin^2 \theta = 0.2$. The figure shows the β spectrum for the case 1) if there is no sterile neutrino and 2) if the sterile neutrino had a mass of 10 keV. Here the mixing angle has been chosen higher for visual purposes. In reality this mixing angle is searched for on the order of $\sin^2 \theta < 10^{-6}$ [1].

The formula describing the β-decay spectrum in the presence of a keV-sterile neutrino [35] is given by the equation 3.2.

$$\frac{d\Gamma}{dE} = \cos^2 \left(\frac{d\Gamma}{dE} \right)_{m_{\nu_e}} \theta(E_0 - E - m_{\nu_e}) + \sin^2 \left(\frac{d\Gamma}{dE} \right)_{m_s} \theta(E_0 - E - m_s) \qquad (3.2)$$
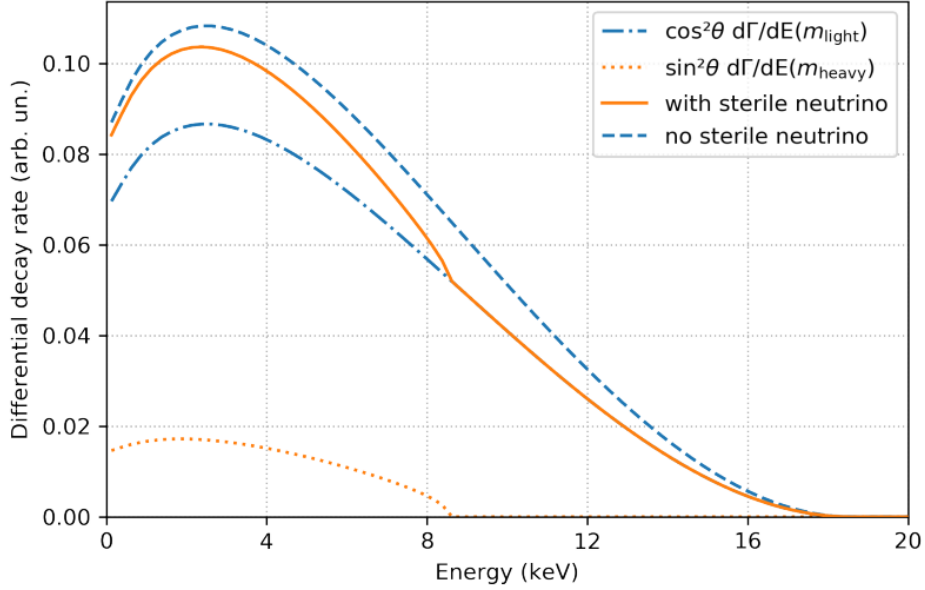
Figure 3.1: Tritium β-decay spectrum. The dashed blue line shows the spectrum without the active and sterile neutrino mixing. The solid orange line represents a spectrum with a mass of 10 keV for the sterile neutrino. The mixing angle is chosen to be $\sin^2 \theta = 0.2$ to see the kink-like signature clearly. This kink also distorts the shape of the β spectrum. The orange dotted line shows the spectral contribution of the sterile neutrino that ends at $E_{\text{kink}} = E_0 - m_s$ and the dashed-dotted blue line represents the contribution of the active neutrinos. Here the energy smearing from atomic, thermal, or scattering effects is neglected. Figure taken from [34].

with θ as the active-sterile neutrino mixing angle and the kinetic energy E of the emitted electron. E_0 is the theoretical endpoint energy of the spectrum, the superposition of the active neutrino spectrum and the sterile neutrino spectrum shows a kink at the energy $E_0 - m_s$.

There are many advantages of using tritium. First, the decay is super-allowed, i.e. tritium will very likely decay via this process and the spectral shape can be described theoretically with high precision [36]. Second, tritium has a relatively short half-life of about 12.3 years, so a small amount is needed while getting high signal rates. Another important point in the sterile neutrino search is to have relatively high endpoint energy in mass ranges of astrophysical interest. With a value of 18.575 keV, tritium is a good candidate. This gives a larger range to search for the sterile neutrino mass. [10]

3.2 Detector Requirements

The TRISTAN project aims to upgrade the KATRIN detector section by, among other things, a new detector, new readout electronics, and a new DAQ system after the neutrino mass measurements are completed. With this detector upgrade the KATRIN experiment will search for keV-sterile neutrinos up to a target sensitivity of $\sin^2 \theta < 10^{-6}$, see figure 3.2.

There are several reasons the new detector with other features is required. A total of 10^{16} electrons have to be collected to reach a parts-per-million (ppm)-level statistical sensitivity, resulting in 10^8 cps on the entire detector over three years. In TRISTAN, about 10^5 cps per pixel are planned to reduce the probability of pile-ups. With these prerequisites, more than 1000 pixels are needed for the detector to handle these high rates by distributing the whole count rate among the pixels.

To reach this goal the parameter space of the mixing angle has to be understood to the ppm level. One of the most suitable detector technologies to which almost all following properties apply is the so-called silicon drift detectors (SDD), which will be explained in more detail in section 3.3. This ppm-level can be achieved by getting high statistics, having an excellent energy resolution, and an excellent understanding of the detector response.

   In figure 3.2, the grey lines with different opacity show the targeted limit for
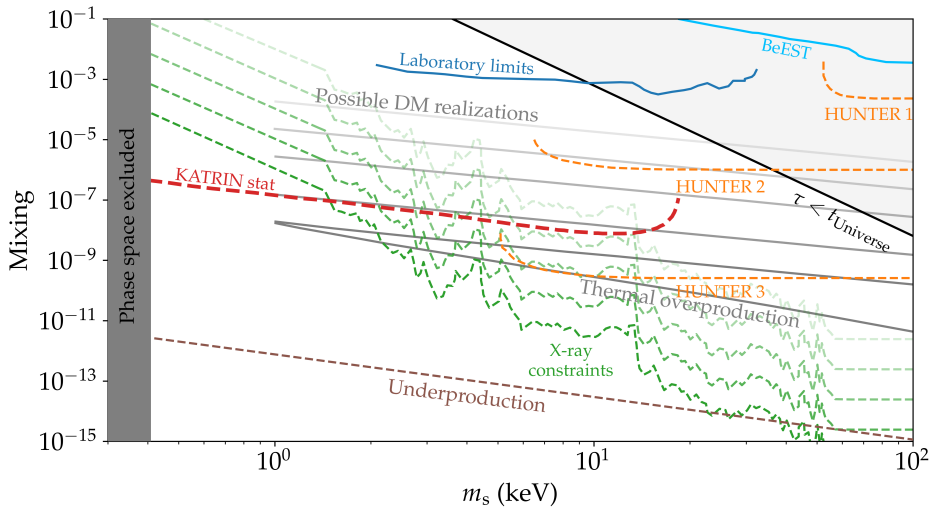
Figure 3.2: Current sensitivity limits of different experiments. The laboratory limits and thermal over- and underproduction are also shown. The grey lines show the possible dark matter realizations that are also reached for with the different TRISTAN phases. For sterile neutrino masses lower than the keV-range the phase space is excluded.

the different TRISTAN phases. The dashed red line shows the goal of the current KATRIN setup measuring over seven days. Here, the signal rate needs to be reduced. The more sensitive phases of TRISTAN will be operated in the differential mode (grey lines) and will have a total statistics of 10^{16} electrons over a measurement time of 3 years and a signal rate of 10^8 cps.

The current KATRIN source strength also depends on the MAC-E filter. The electron rate at the detector is about 1 electron per second for a retarding potential qU of 1 eV above the endpoint Q. That would lead to more than 10^{10} electrons per second at TRISTAN [35]. Without applying a retarding potential, the number of electrons would be too high to handle for the equipment.
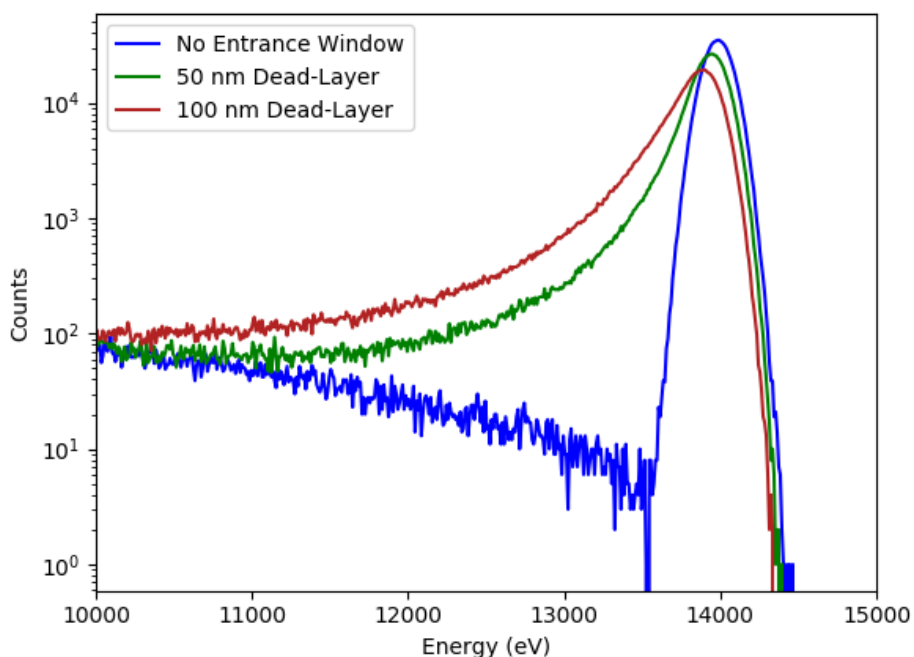
Figure 3.3: Simulation of dead layer effects on the energy spectrum for mono-energetic electrons at 14 keV. The electrons interact with a silicon detector. For the energy spectrum, the assumption is a detector with a noise of 220 eV FWHM, and electrons that can backscatter and leave the detector. In blue, the energy spectrum without effects of the entrance window is shown, while green and red represent the effects of a dead layer with different thicknesses. The simulation was done with KESS [37]. The figure is taken from [35].

The entrance window is one important consideration for the detector system

to improve the energy resolution. The energy deposition of electrons in matter is continuous, which means that they can deposit a large amount of their energy in the small or non-sensitive volume of the entrance window. The simulation in figure 3.3 taken from [35] shows mono-energetic electrons at 14 keV under consideration of a dead layer.

The blue line represents the energy spectrum when no effects of the entrance window were taken into account, while the red and the green curves show the effect of a dead layer with different thicknesses. Here the electrons interact with the silicon detector and can backscatter, leaving the detector. A noise of 220 eV FWHM at 14 keV is assumed. It can be seen that the total shape of the spectrum changes with different dead layer thicknesses and gets shifted to lower energies, as shown in figure 3.3. One danger is that the energy resolution is so bad that the kink in the β-spectrum can not be resolved and gets smeared out. So a resolution better than 300 eV FWHM at 20 keV is needed. Both the shaping time τ and the energy resolution over the serial or voltage noise Q_{series} are connected via the formula 3.3.

$$Q_{\text{series}} = \sqrt{4kTR_{\text{s}} + e_{\text{na}}^2} \cdot \frac{C_{\text{d}}}{\sqrt{\tau}}. \tag{3.3}$$

The capacity C_{d} of the detector and the noise e_{na} of the amplifier, have to be very small, resulting in a better energy resolution. By cooling the detector the noise in the system can be reduced as can be seen in the formula (temperature T). The serial resistance R_{s} of the detector and the Boltzmann constant k play a role in the calculation of the serial or voltage noise.

This also affects the energy resolution as can be nicely seen in figure 3.4. The effects on the energy spectrum and, therefore, on the value of the FWHM depend not only on different noise widths and different dead layer thicknesses but also on the incoming electron energy. For electrons with lower energy, these effects increase because of the decrease of the mean free path and the more frequent interaction near the surface. Therefore, the thickness of the dead layer or entrance window needs to be as thin as possible. From the simulation, a maximum thickness of 55 nm is found [35].

It is of utmost importance to fully understand the detector response to investigate the parameter space of the mixing angle up to the ppm level. Therefore a precise understanding of the calibration is mandatory. The calibration will be addressed further in chapter 5.

Another important prerequisite is to understand detector effects such as charge sharing and backscattering. The first one is the effect of charge transfer from one pixel to another by diffusion of electrical charges. This charge sharing can be minimized by increasing the pixel area while not affecting the energy resolution and the charge collection time. Backscattering means the reflection of particles on the detector surface. Three aspects have to be considered to reduce the probability of
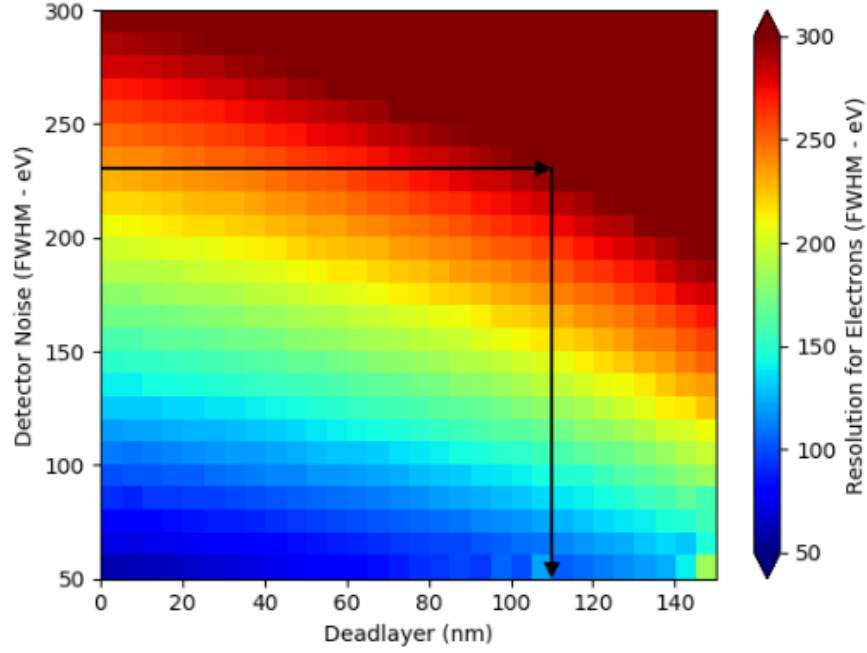
Figure 3.4: Detector noise versus deadlaer. The colorbar indicates the energy resolution with regard to the FWHM, different noise and different dead layer thicknesses are shown for mono-energetic electrons at 20 keV. In dark red, the energy resolutions higher than 300 eV can be seen. It can be observed that the maximum dead layer thickness can be 110 nm [35]. This simulation was done with KESS [37]. Figure is taken from [35].

backscattering. Firstly, when choosing a pitch angle (angle between the momentum vector of the electron and the magnetic field) of $\theta_{det} < 20$ at the detector and not less than maximal

$$\theta_{max} = \arcsin \left(\sqrt{\frac{B_{det}}{B_{max}}} \right) \tag{3.4}$$

with $B_{max} = 6$ T, the magnetic field of the detector B_{det} is smaller than the maximum magnetic field in the system, a minimum of $r_{det} \gtrsim 6$ cm for the detector surface can be found and the backscattering probability gets minimized. Secondly, a magnetic field at the detector of $B_{det} < B_{max}$ lets the electrons reflect back on the detector surface [38].

The readout electronics have to meet some criteria as well. For example, it needs to operate at short shaping times τ to reduce pile-up effects and increase the processable

rate.

A simulation carried out in [39] taken into account all the considerations described above, shows that the optimal pixel diameter for a detector with 3500 pixels is 3 mm, and the detector surface has a value of

$$A = \pi \cdot (10 \text{cm})^2. \tag{3.5}$$

The magnetic field of the detector should have 0.7 T [38]. The low noise, even for large pixel diameters and high count rates, as well as the small or non-sensitive volume at the surface and the resulting charge collection efficiency at the entrance window or dead layer, make them the perfect candidates to search for keV-sterile neutrinos.

3.3 Silicon Drift Detectors

In cooperation with the Semiconductor Laboratory of the Max Planck Society (HLL) [2], new Silicon Drift Detectors (SDD) are developed for the TRISTAN project. These SDDs can handle high rates with an excellent energy resolution near the Fano-limit [38]. The Fano-limit specifies the best achievable energy resolution of a detector, taking into account statistical fluctuations of the signal processing. SDDs can detect ionizing radiation like photons, electrons, and other charged particles and are a special kind of semiconductors.

In this section, firstly, the working principle of semiconductors in general and then specifically of Silicon Drift Detectors will be explained in section 3.3.1 and section 3.3.2, respectively.

Finally, the module design (section 3.3.3) of the TRISTAN detector will be presented.

3.3.1 Basic Semiconductor Principle

Materials are generally divided into three types: Metals are conductive, while insulators are not conductive. Semiconductors, as the name implies, are conductive under certain circumstances. Between all three types, there is a smooth transition. Semiconductors are crystals with a well-structured periodic placement of atoms. The smallest pattern that can be found without the atoms is called a primitive cell and can build the entire crystal. The two most interesting structures in terms of semiconductors are diamond and zincblende lattice structures. Both are face-centered lattice types. Those tetrahedral phases are characterized by the fact that each atom is surrounded by four equally close neighbors lying in the corners of the tetrahedron. Essential to understanding the processes inside semiconductors is the energy-momentum conservation of the charge carriers. Like scattering, interactions between

photons and phonons lead to electron-hole pairs from which the concept of energy gaps is derived. The energy-momentum relation can be used to obtain the band structure of a crystalline solid by solving the Schrödinger equation for one particle in a potential [40]. The Bloch function gives the solution to this equation. One of the most important theorems for the band structure, the Bloch theorem, states that the potential energy is periodic in the direct lattice space. [41]

There is a forbidden energy zone in each semiconductor where no states are allowed. This leads to energy bands over or under this so-called energy gap. The upper band is called the conduction band, and the lower band is called the valence band. A comparison of the bands in metals, semiconductors, and insulators is shown in figure 3.5. The conduction and the valence band in metals touch each other or
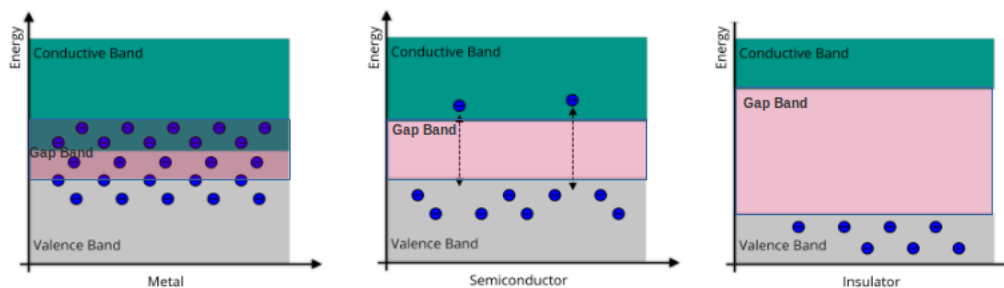
Figure 3.5: Band structures of metal, semiconductor and insulator. In metals, the valence and the conduction band touch each other or even overlap, while insulators have a large bandgap. The first has many free-charge carriers. The latter has all electrons in the valence band, which means there is no conductivity. For semiconductors, conductive properties can be reached by changing the temperature or by doping. The figure is taken from [35].

even overlap, while those bands in insulators are far separated. Semiconductors lie between metals and insulators and are neither good nor bad conductors. Because of their relatively small bandgap, electrons from the valence band can be excited even by thermal oscillations. This mostly happens at room temperature or by absorption of light quickly into the conduction band. As a result, the electrons leave holes in the valence band. Holes in the valence band and electrons in the conduction band are called free charge carriers. By changing the temperature or doping, the semiconductor's conductivity can be influenced. The valence band gets more occupied at lower temperatures, and the conduction band is empty. For higher temperatures, semiconductors have a higher conductivity because the probability of thermal excitation of the electrons from the valence band into the conduction band rises, and more free charge carriers are available.

It is crucial to use detectors with high conductivity to detect particles. Therefore the number of free charge carriers in the detector material needs to be reduced. Then conductivity only appears when an electron-hole pair is created by an external particle that deposits energy within the detector. One way to make semiconductors more conductive is to dope the material with different types and purity concentrations. With this procedure, the resistance can be varied. The interface between those doped materials is called pn-junction. Here energy is deposited in the depleted zone, a space charge zone with a lack of charge carriers. This leads to local electron-hole pairs. Those are separated when an electric field is applied and cannot recombine. When moving to the non-depleted areas, they can be measured as a reversed current in the diode. In figure 3.6, the pn-junction is illustrated schematically. The depleted area is yellow, the n-type region is blue, and the p-type region is red.
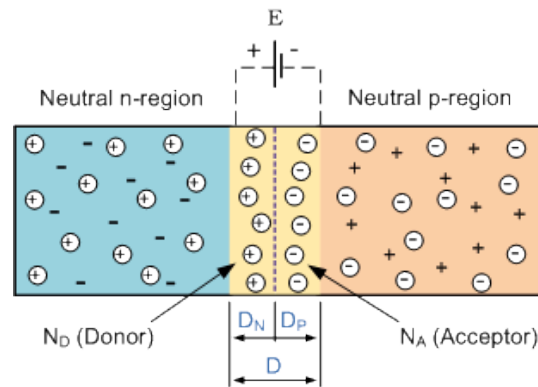
Figure 3.6: In this sketch of a pn-junction, the n-type region is shown in blue, the p-type region in red and the depleted area in yellow. Taken from [42].

3.3.2 Silicon Drift Detectors

Silicon Drift Detectors, short SDDs, are precisely such doped semiconductors. The basis is the type IV material silicon of the periodic table. This element does have many advantages. It is very abundant, and due to its low energy threshold of $3.6\,\text{eV}$ to create an electron-hole pair, it has a higher resolution and a higher count rate than other materials [35]. In ultra-pure silicon at room temperature, only about 1 of 10^{12} silicon atoms are ionized. The silicon can get doped to increase this ionization.
The n-type silicon is typically doped with the type V material, phosphorus. In contrast to silicon, this element has five valence electrons and does not match the structure of silicon crystal, serving as an electron donor. The p-type silicon is doped with a type III element, for example, boron, that only has three valence electrons and serves as an electron acceptor. In figure 3.7, an example of silicon doping can be seen,

where the leftmost picture shows the intrinsic silicon with four covalent bonds at each silicon atom, and the middle one shows the n-type silicon with phosphorus as the donor, giving one electron to the conduction band. The right picture presents the p-type silicon with boron as an acceptor that contributes with a positively charged hole in the valence band. The doped impurities usually have energy levels inside the energy gap.
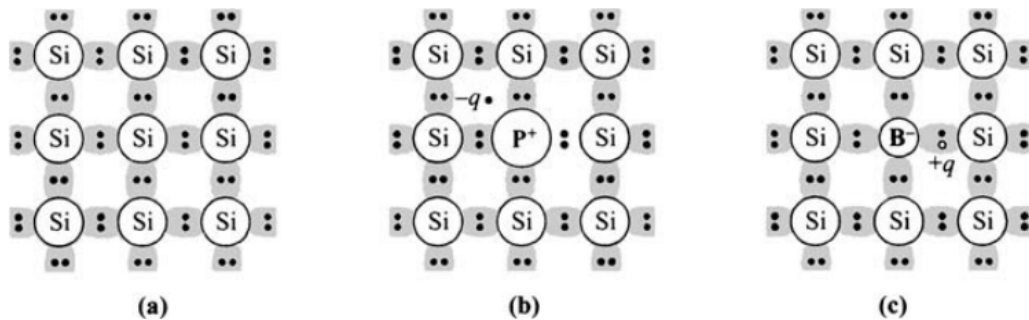
Figure 3.7: Doping of silicon a) intrinsic and pure silicon. b) n-type silicon with phosphorus as the donor. c) p-type silicon with boron as acceptor. [41]

The surface charge carriers move to the opposite regions, recombine and leave fixed charged doped atoms. An electric field against the movement of the free charge carriers prevents further diffusion and is therefore called diffusion voltage $U_{diffusion}$. This leads to a dynamic equilibrium in the transition area without free charge carriers, as shown in figure 3.6 and is called the depleted zone. The depleted zone can be increased when an additional external voltage U_{bias} is applied in the same direction as the diffusion voltage [43].

Incoming particles interact within the depleted zone by forming a charge cloud consisting of electron-hole pairs. The electrons move against the electric field to the n-type silicon side and are read out. This site is also called the anode. The holes move towards the cathode to the p-type silicon side. The collected charge is proportional to the deposited energy of the particles. The depleted zone has a thickness of $D_N + D_P$ and depends on the densities of the donor and the acceptor in the silicon. This so-called pin-detector is only sensitive to charge deposition inside its depleted region.

For pin-diodes, the anode must have the same size as the pixel. This results in higher noise for larger pixel sizes because the noise is proportional to the size of the anode. For this reason, a unique principle was developed to ensure a smaller anode with the highest depletion. This is called sidewards depletion. Figure 3.8 shows an ideal way of achieving this sidewards depletion. The p^+ electrode extends over
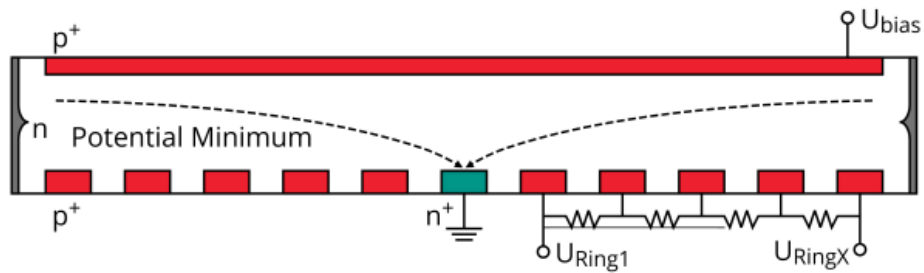
Figure 3.8: In the scheme of sidewards depletion, the p^+ electrode (red) extends over the whole surface of one side of the detector. The white region is depleted and the separated electrodes at the bottom together with a drift voltage U_{Ring_X} to U_{Ring_1} cause the electrons to drift towards the small n^+ anode (green). Also a high enough voltage U_{bias} is applied for full depletion. Taken from [35]

the entire surface of one side of the detector, while the n^+ anode only takes a small part on the opposite side. With the separated electrodes at the side of the anode and a drift voltage $U_{Ring_X} = -110\,V$ to $U_{Ring_1} = -20\,V$, the electrons drift towards the anode, and inside the sensor, the area is depleted [43].
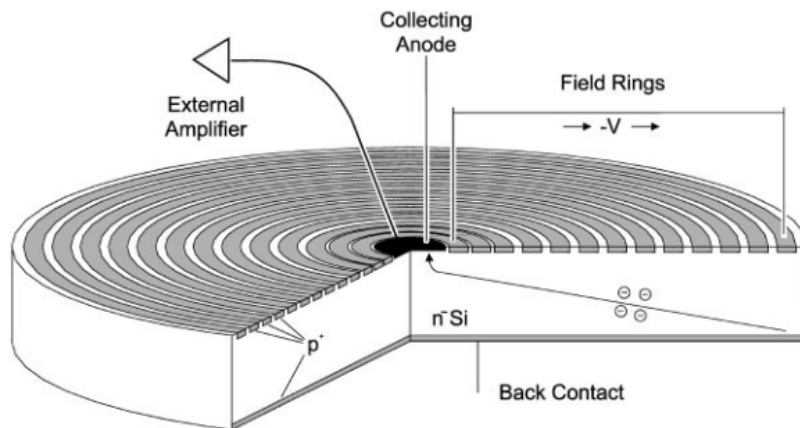
Figure 3.9: Cross-section of a circular SDD detector with thirteen drift rings and a small anode in their middle. An electric field guides the electrons towards the n-type anode and collects them. The entrance window on the bottom, as well as the drift rings, are p-type silicon. From [44]

The final design of the SDDs for the TRISTAN project is shown in figure 3.9. At the bottom lies the p-doped entrance window, and at the top, the p-type drift rings and the small n-type anode can be seen. The electrons created inside the depletion zone are led to the anode caused by the radial component of the electric field that comes about through the voltage in the drift rings. SDDs have low noise and a high processing rate due to their low anode capacity. They can be up to several mm^2 or even cm^2 in size.

3.3.3 Module Design

The final TRISTAN detector will consist of 21 modules, each hosting 166 pixels. The entire detector will then have a diameter of 20 cm. [45]. An exemplary picture 3.10 shows the final detector setup.
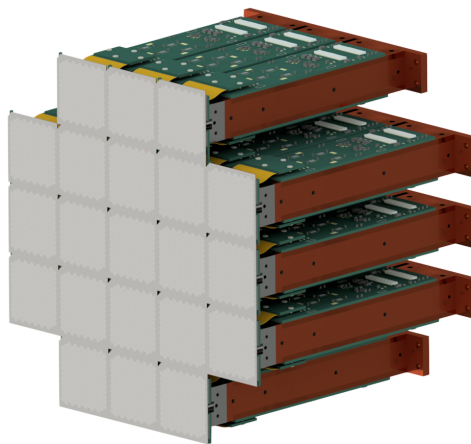
Figure 3.10: Example of the final TRISTAN detector for phase-2. It consists of 21 modules with each 166 pixels.

The very first 166-pixel module shown in figure 3.11 had a $3.8 \times 4.0\,cm^2$ silicon chip on top. This silicon chip consists of 166 pixels with each a diameter of 3 mm. They were produced by the HLL [2]. The silicon chip on top of the column is 450 μm thick and is glued on a custom-made carbon fiber reinforced silicon carbide together with a thin, rigid-flex cable to route the signals in a $90°$ bend and therefore can operate as a 3D module. The pixels on the modules are arranged in a hexagonal

Rigid flex PCB ETTORE ASICs

166-pixel SDD

Copper cooling and
holding structure

Silicon carbide (CeSiC)
thermal link
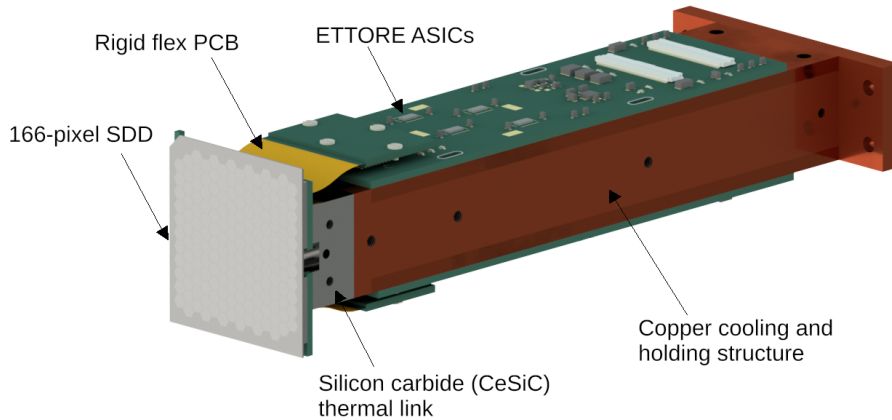
Figure 3.11: Example of first 166 pixel module. The silicon chip with the 166 pixels is mounted onto the silicon carbide thermal link that is installed on a copper block. Also an ETTORE ASIC board is placed on this copper block and is connected with the silicon chip via an rigid flex PCB.

shape, like a honeycomb, and are lying on the detector board. There is no space between the pixels with this pixel shape, so the non-sensitive area is minimized. Also, it has all the advantages of a radial design. [45]

Because it is important to amplify the signals of the SDDs as soon as possible to guarantee the best energy resolution, the Field Effect Transistor (FET) is integrated into the SDDs and the ETTORE ASIC amplifier is as close as possible placed on the ASIC board. This is then screwed onto a copper block to cool the detector to -50° C to reduce the leakage current. [1]

After the first amplification on the ASIC board, the signal is again amplified in the bias board to be passed on to the data acquisition (DAQ). The bias board resets the signal at the ASIC-CUBEs, to discharge them. A typical waveform can be seen in figure 3.12. The increasing ramp is caused by the leakage current that throughout charges the input of the CUBEs. The sharp dropping edge comes from the reset pulse to discharge the ASICs. Otherwise, it would reach saturation, and the signal could not be amplified anymore. A signal like a photon or a charged particle shows a step on the ramp. The height of the step corresponds to the deposited energy. When two particles hit the detector within a time interval shorter than the peaking
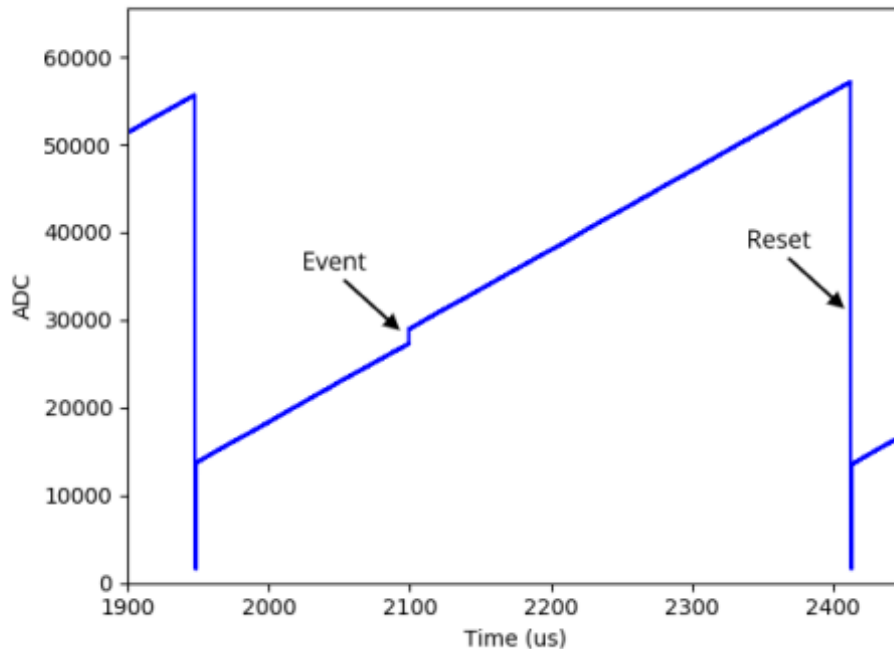
Figure 3.12: Typical waveform of the SDD. Leakage current causes the ramp because it charges the CUBEs. Before it reaches saturation, the ASICs have to be discharged by a reset pulse, which causes a sharp dropping at the end. A signal stands out through a step on the ramp. This points to a photon or a charged particle because it charges the ASICs faster than the leakage current. From [43].

time of the filter, pile-ups can occur, which must be treated carefully. [43]
Different modules were designed for the different phases of TRISTAN to test out the upscaling behavior of the electronics. In phase-0, a stepwise integration is performed. In 2021 the 47-pixel 3D prototype was successfully integrated into the monitor spectrometer. This thesis data is based on what was taken with this prototype detector. The next step would be to incorporate a 166-pixel SDD 3D module in the MoS.
For phase-1, nine modules with about 1500 pixels in total are planned to be built and tested inside the monitor spectrometer. The final phase-2 will then consist of 21 modules with each 166-pixels integrated into the KATRIN experiment to search for sterile neutrinos.

4 Monitor Spectrometer

Although the initial purpose of the monitor spectrometer was to monitor the high voltage of the main spectrometer, it is now also used for measurements and improvements of the experiment. It is based on the former Mainz neutrino mass experiment [34] transported to KIT and optimized to fit the KATRIN experiment better. With this, a new detector for the TRISTAN project can also be tested and characterized. In this chapter, an overview of the experimental setup will be given. Then, the different electron sources will be presented.

4.1 Experimental Setup

The Monitor Spectrometer (MoS) is essentially a smaller version of KATRIN. The idea is to monitor the long time stability of the high voltage of the main spectrometer of the KATRIN experiment. This second MAC-E filter is galvanically connected to the high voltage network of KATRIN and, therefore, has the same vessel voltage that is powered by the same power supply. For this reason, data can be taken simultaneously. Thereby the monitoring in real-time is easier. To understand the integral β spectrum, it is of great importance that the retarding potential of the MAC-E filter is precisely understood and the high voltage measurement is stable on the ppm level. That means even a tiny variation of the retarding voltage of 3 ppm at -18.6 kV, can shift the observed neutrino mass squared of about -0.007 eV^2 [30].

The monitor spectrometer measures the K$_{32}$-line of ^{83m}Kr with a very high resolution to investigate the detector performance. More information on ^{83m}Kr is given in section 4.2.3. [46]

The monitor spectrometer consists of the spectrometer, the vacuum system, the heating system, the high voltage supply, the magnetic system, the air coils, and the readout system. These components are described in more detail in the following.

Spectrometer The most significant part of the monitor spectrometer is the stainless steel vessel. It is 1 m in diameter and 3 m in length. An ultra-high vacuum of about $9 \cdot 10^{-11}$ mbar can be achieved [30]. In the monitor spectrometer, the tank encloses a

set of cylindrical and conic stainless steel solid electrodes and stainless steel wire electrodes that form the electromagnetic field in the spectrometer. The tank itself is grounded, and the wire electrode has a possible potential difference of 5 kV to the cylinder electrode. [46]

In picture 4.1 the setup of the Monitor spectrometer with the big spectrometer tank can be seen. On both ends, magnets are used to focus the electrons. The detector is placed in a vacuum chamber on the outer right side, while the source lies upstream on the outer left side [47].
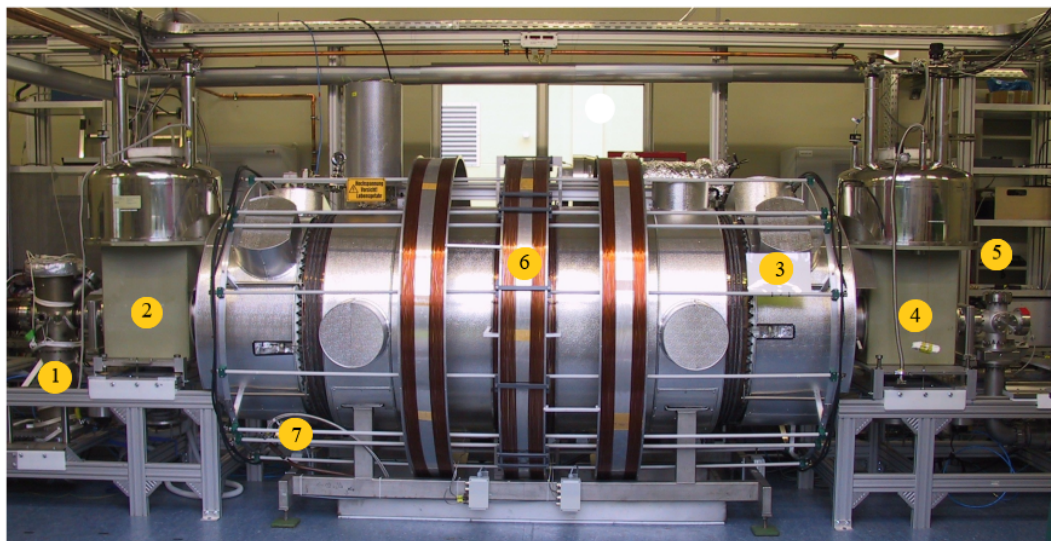
Figure 4.1: Photography of the monitor spectrometer. The calibration source is located on the outer left side (1). The electrons pass a magnet (2) before entering the spectrometer tank (3) in the middle. When they leave the tank, they again pass a magnet (4) and hit the detector on the outer right side (5). The copper-colored coils build the Low Field Compensation System (LFCS, 6). Horizontally surrounding the tank is the Earth Magnetic Field Compensation System (EMCS, 7). This picture is taken from [46].

Vacuum system   An ultra-high vacuum system was installed to reduce the background and prevent the electrons inside the monitor spectrometer from being scattered at air molecules. The pressures in the spectrometer reaches $1 \cdot 10^{-9}$ mBar or better. [46]

Heating system   The heating system includes heating cables on the vessel hull, the detector, and the source chamber. It serves to back out the spectrometer at $200°$ C to

reach a better vacuum in the tank. Three regions can be controlled separately. Many PT100 sensors that are special thermometer resistors monitor the entire system. [46]

High voltage supply   The cylindrical vessel is connected to cables providing up to 35 kV and also to an additional ground electrode [46]. There are two possible operation modes. One is the standalone mode, where the local power supply and a high voltage splitter are used for precise surveillance of the voltage. The other one is the parallel mode. Here a remote switch of the main spectrometer of the KATRIN HV system comes into use. It is regulated with a high-precision KATRIN K35 and K65 divider and read out by two precise voltmeters. The electron source can be biased with a separate power supply at a potential up to -1 kV. It is then read out with a commercial divider and voltmeter. The result is an integrated spectrum acquisition by increasing the voltage stepwise at the retarding potential or the source. [47]

Magnetic system   As can be seen in figure 4.1, two superconducting magnets are placed at the entrance and on the exit region of the monitor spectrometer. Each magnet has about 36500 windings to create an axial symmetrical magnetic field [47]. The maximum magnetic flux density is 8.6 T at 71.48 A. Figure 4.2 illustrates the magnetic field lines for a magnetic field strength of 7.2 T. The magnetic system is
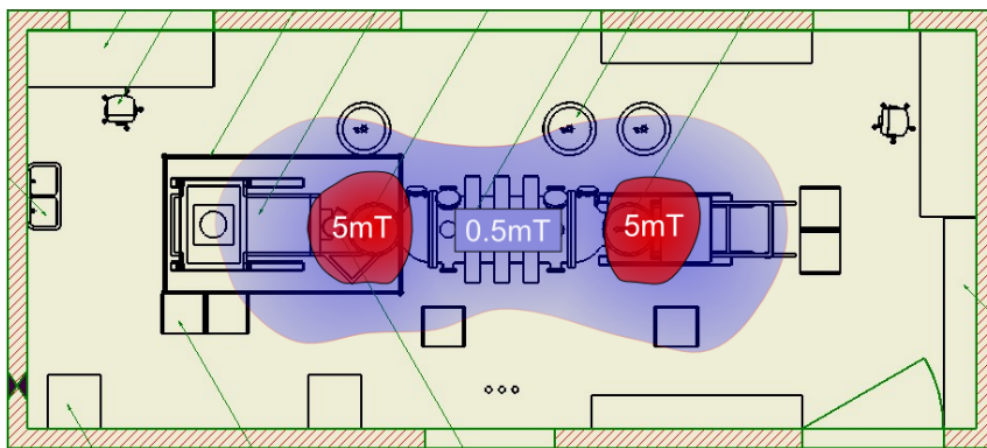
Figure 4.2: Magnetic field in the monitor spectrometer for a magnetic flux density of 7.2 T at the center of the magnets is illustrated. The blue area shows the region in which the field reaches more than 0.5 mT. Directly at the magnets, the field exceeds 5 mT. This region, shown in red, does not yet damage normal devices [46]

operated at 4.2 K with liquid helium and set so that the energy resolution is similar

to the one of the main spectrometer of the KATRIN experiment. The relative energy resolution is defined by equation 4.1.

$$\frac{\Delta E}{E} = 5.8207 \cdot 10^{-5} \tag{4.1}$$

This corresponds to ΔE = 1.04 eV for the K-32 energy of E = 17.83 keV. [47] Four air coils supplement both the magnets at the ends of the vessel with average conductivity in between [30]. The distance of the magnets to the detector plane is 2.01 m. The monitor spectrometer is typically not operated at its maximum field settings. This means the magnetic flux density is about 6.014 T at 50 A. [46]

Air coil system   Two air coils surround the vessel mainly to compensate for the Earth's magnetic field. The Earth Magnetic Field Compensation System (EMCS) is made from horizontal white copper tubes and shields the magnetic background coming from the Earth, about 50 μT. These tubes run perpendicular to the spectrometer axis building a horizontal and also vertical magnetic field to conserve the axial symmetry [47]. The Low Field Compensation System (LFCS) consists of four air coils around the vessel, each having a few dozen windings. This system prevents the electrons inside the vessel from hitting the walls of the spectrometer and, therefore, restricts the magnetic field lines to the inside of the spectrometer tank. [46]

Readout system   Depending on the particular measurement campaign, different readout systems are being used. For the measurement presented in this thesis, the KERBEROS system developed at Politecnico di Milano has been used [48]. The new KERBEROS system, shown in 4.3, with 160 × 220 mm in size, has been particularly developed for measurements with the TRISTAN detector in the monitor spectrometer. This Analog Pulse Processing (APP) is suitable to read out many channels with a high data rate density because of its low power consumption, low costs per channel, and small dimension. Compared to a Digital Pulse Processing (DPP), the disadvantage of this APP is a lower throughput, and it is not possible to record raw waveforms [49]

The APPs used for KERBEROS are based on application-specific integrated circuits (ASICs), so it is an ASIC-based multi-channel pulse processing and data acquisition system with 48 channels to read out large arrays of SDDs. The 48 channels are distributed among three so-called SFERA ASICs, each of them covering 16 analog channels. They have a ninth order semi-Gaussian sharper, a programmable filter for the time from 5% of the maximum to the maximum, called peaking time [50]. It can be set between 0.5 and 6 μs [48]. More information about the SFERAs can be found in [51].

In TRISTAN, the Polling-Gamma mode is implemented to use the full-matrix burst

readout strategy. Here all channels acquire the data simultaneously when a physical event is recognized.

The SFERA ASIC can cover an extensive energy range because of the inherent
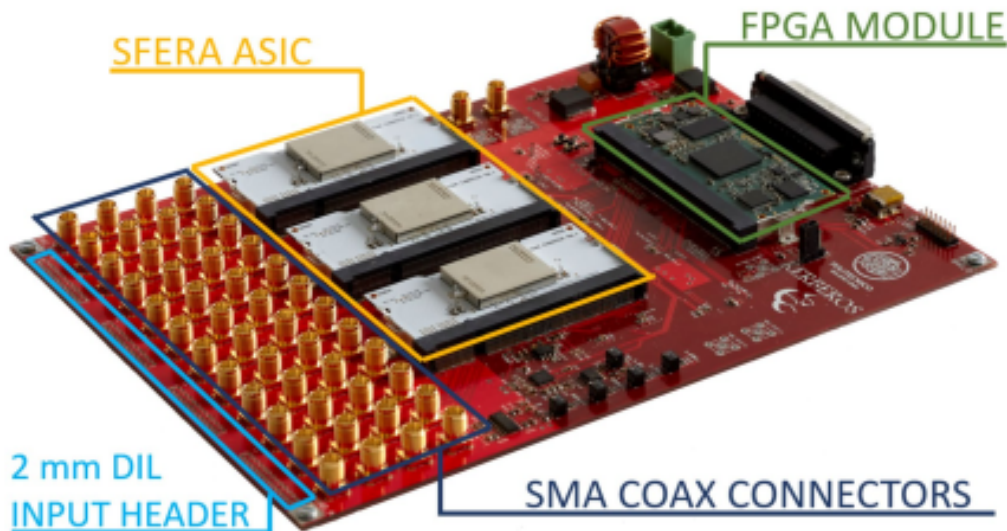
Figure 4.3: Photography of the KERBEROS DAQ system (dimensions $160 \times 220\,\text{mm}$) used in the monitor spectrometer to read out a TRISTAN detector module. The DAQ mainly consists of three SFERA ASICs, an FPGA module and several connectors. [49]

capability of the FPGA to be re-programmable. The FPGA transmits the data to a PC. [48]

Figure 4.3 also illustrates the two different Input connectors. One consists of the 48 individual SMA coaxial input, while the other is a four 24-pin dual-in-line 2 mm header. They are connected to a filtered power supply with two different voltage regulators to separate between analog and digital domains. The supply voltage is 6.0 V. The supply current is 1.4 A, resulting in the total power of 8.4 W, which leads to 175 mW per channel [49].

The input is routed to the analog chip, the SFERA, and gets processed and filtered via a semi-gaussian shaping filter with adjustable peaking times of $0.5\,\mu\text{s}$, $1\,\mu\text{s}$, $2\,\mu\text{s}$, $3\,\mu\text{s}$, $4\,\mu\text{s}$, and $6\,\mu\text{s}$. The SFERA Peak Stretcher circuitry and the Pile Up Rejection (PUR) circuitry detect the peaks and exclude partly overlapping pulses, i.e., pileup events. The chip also features a fast shaping filter with a shaping time of $0.2\,\mu\text{s}$. After transmitting the data as a single complex signal (multiplexing), they are forwarded to an external ADC by Linear Technology. The communication between the different components and the implementation of the different readout multiplexing strategies,

as well as the transmission of the data to the host-PC, is realized via the Artix-7 FPGA module.

When an event in one channel is registered, all three SFERA ASICs are triggered simultaneously, and the whole matrix freezes and gets readout. This makes it possible to get the complete map of the detector at the time of the event. A study and a correction of partially energy deposition phenomena like backscattering and charge sharing events can be performed. The maximum input count rate of the KERBEROS is 166 kilo counts per second (kcps), and its maximum data throughput is 34 MB/s. [48]

4.2 Electron Sources

For the monitor spectrometer, three different electron sources are available. The most important source for this thesis is the krypton source that is described in section 4.2.3. After its commissioning in September 2021, it is now possible to generate electron beams with the new electron gun (e-gun). This device will be presented in section 4.2.2. In section 4.2.1 the principle of using wall electrons is explained based on a measurement performed in June 2021 and analyzed in this thesis.

4.2.1 Wall Electrons

Wall electrons are electrons emitted by the spectrometer electrode. The assumption is that electrons are generated by the impact ionization of positive helium ions. These helium ions originate from the decay of remaining elements in the spectrometer [50]. The produced secondary ions and electrons are accelerated by a potential difference and influence the flux pressure of the beam by collision with air molecules. The acceleration away from the electrode causes the electrons to reach the detector with energies similar to the retarding potential of the spectrometer.

In June 2021, measurements were done without an applied magnetic field and for

Table 4.1: High voltage settings of the monitor spectrometer and corresponding wall electron energies. The difference between the values comes from the challenge of fine-tuning the high voltage settings.

High voltage setting (kV)	Wall electron energy (keV)
8.998	9
17.998	18
20.999	21
24.998	25
29.999	30

different high voltages listed in table 4.1. The detector used for this measurement was the 47-pixel 3D prototype S0-47-3. Figure 4.4 shows the total count rate for the wall electron measurement at a high voltage setting of 30 kV.

The cyclotron motion of the electrons results in a band-like structure on the detector.
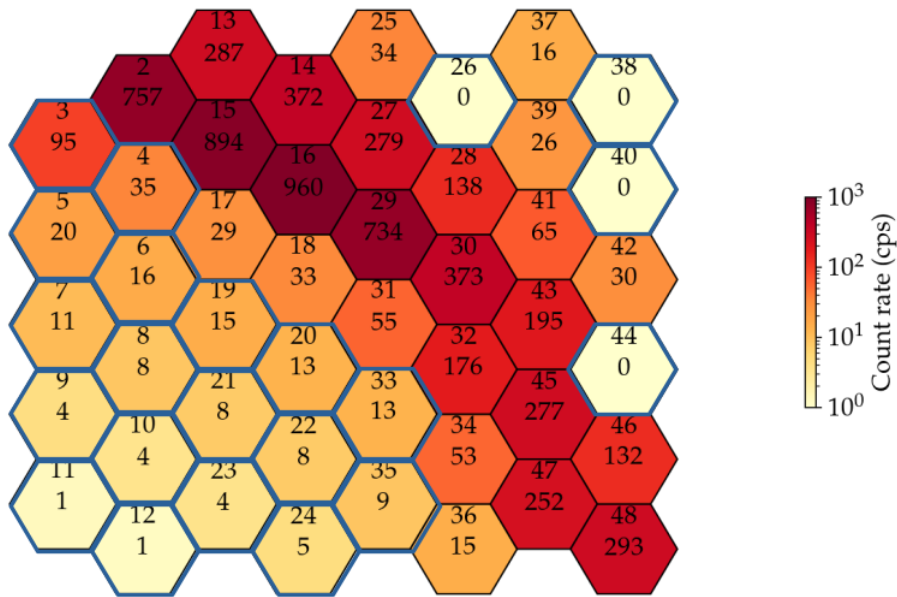
Figure 4.4: Detector pixel map showing the total count rate in counts per second (cps) of a wall electron measurement taken in June 2021. The blue-bordered pixels had a low count and were therefore excluded from other analyses. Some pixels were broken from the start; these are shown in white. The cyclotron motion of the electrons caused by the magnetic field of the detector magnet leads to a band-like structure on the detector.

The measurements done in June were test measurements with wall electrons. Each measurement lasted 3×5 minutes. Wall electrons with different high voltage settings (see table 4.1) provide a rough estimate of the detector performance. Turning off all magnets except for the source magnet enables the focus of the electrons from the wall onto the detector. The detector magnet is operated at a reduced current of about 1/3 of the normal operation mode.

The EMCS compensates for the Earth's magnetic field in the spectrometer but at a low current of 1.68 A for one coil and 19.5 A for the other coil. Therefore, the central field lines point to the high voltage electrode, as shown in figure 4.5.

Figure 4.6 shows the energy spectra acquired with a 47 channel TRISTAN SDD
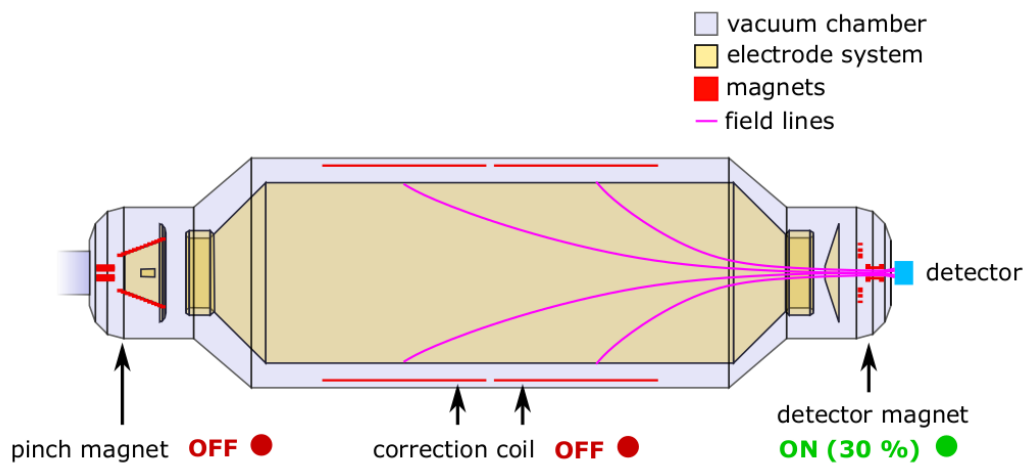
Figure 4.5: Schematic view of the monitor spectrometer for measurements with wall electrons. The pinch magnet is turned off in this configuration while the detector magnet is turned on. The field lines point from the detector to the main electrodes. The correction coils are turned off as well. Only the EMCS prevents the Earth's magnetic field lines break the symmetry of the detector magnetic field lines. [50]

of the pixels 16 and 34. The detector was oriented such that pixel 16 is directly exposed to the beam of the wall electrons, while pixel 34 is located outside of the beam. Therefore, the count rate of pixel 34 with 53 cps is much lower than the count rate of pixel 16 with 960 cps.

Four characteristics can be observed in the energy spectra of the wall electrons. The first feature is the main peak. This peak represents the electrons that deposit their entire energy in the detector. The second feature, the so-called silicon escape peak (SEP) is visible in the energy spectra with energies above 18 keV for pixel 16. This SEP originates from an electron being knocked out of the K-shell by the deposited energy of the incoming radiation. An M-shell electron fills the resulting hole in the K-shell of silicon, emitting a photon with an energy of about 1.74 keV. This energy corresponds to the K_α line of the silicon [35]. The third characteristic, the backscattering tail, is caused by backscattered electrons. This will be explained in detail in section 5.3.2.
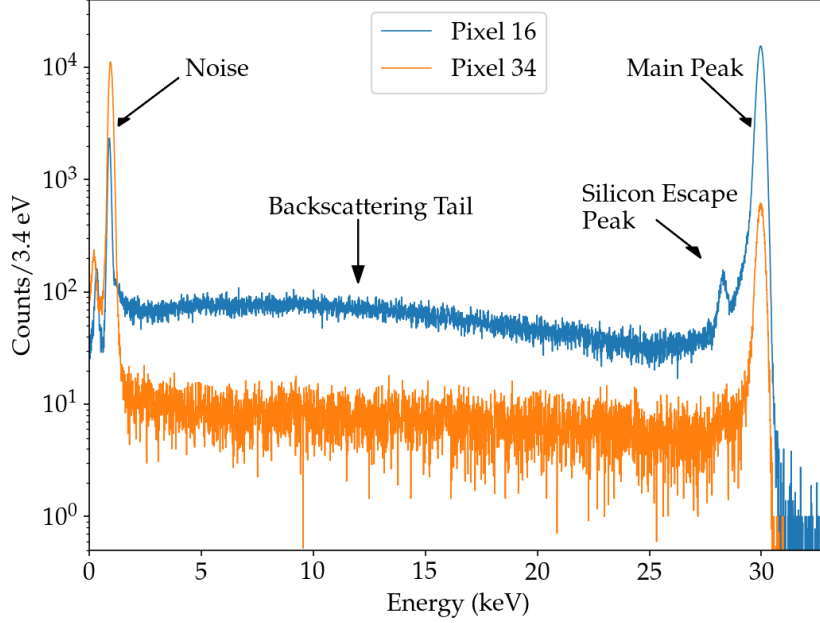
Figure 4.6: Comparison of the energy spectra obtained by wall electrons of 30 keV for two pixels of a TRISTAN prototype detector. The figure shows the typical features of the electron energy spectra. The noise is located close to zero energy. The backscattering tail is approximately constant between the noise and the silicon escape peak. About 1.74 keV shifted from the silicon escape peak lies the main peak, containing most of the deposited energy of the incoming electrons.

The last feature is the noise. The peaking time filter discards all events with energies below a certain threshold, and their energies are set to zero. Therefore, a peak appears there in the spectrum. The energy spectra of the wall electrons were calibrated with a special empirical model function, shown in equation 4.6, which will also be used and explained in the later analysis (see section 5.3.2).

$$I_G(E) = A_G \cdot \exp \frac{-(E - E_0)^2}{2 \cdot \sigma^2} \tag{4.2}$$

$$I_D(E) = A_D \cdot \exp \left(\frac{E - E_0}{\beta_D} \right) \cdot \mathrm{erfc} \left(\frac{E - E_0}{\sqrt{2} \cdot \sigma} + \frac{\sigma}{\sqrt{2} \cdot \beta_D} \right) \tag{4.3}$$

$$I_B(E) = A_B \cdot \left(\frac{E}{E_0 - a} \right)^b \cdot \left(1 - \frac{E}{E_0} \right)^c \tag{4.4}$$

$$I_{\text{esc}}(E) = A_{\text{esc}} \cdot \exp\left(\frac{-(E_0 - \Delta E_{\text{esc}} - E)^2}{2\sigma^2}\right) \tag{4.5}$$

$$I_{\text{Calibration}}(E) = I_{\text{G}}(E) + I_{\text{D}}(E) + I_{\text{B}}(E) + I_{\text{esc}}(E) \tag{4.6}$$

The calibration fit for pixel 16 at the different high voltages is shown in figure 4.7.
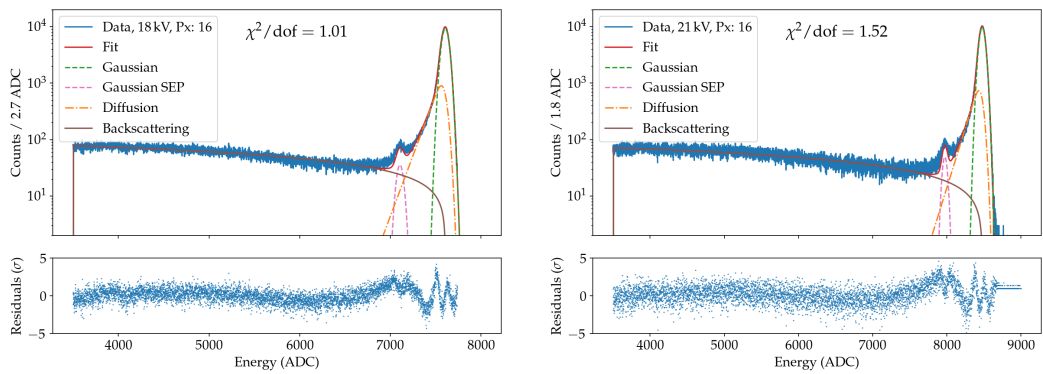
(a) Energy spectrum of pixel 16 of wall electrons at 18 kV high voltage setting.

(b) Energy spectrum of pixel 16 of wall electrons at 21 kV high voltage setting.
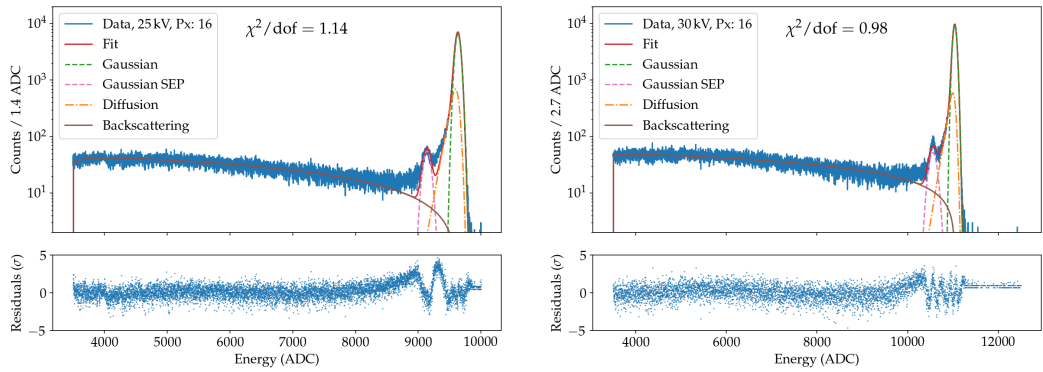
(c) Energy spectrum of pixel 16 of wall electrons at 25 kV high voltage setting.

(d) Energy spectrum of pixel 16 of wall electrons at 30 kV high voltage setting.

Figure 4.7: Uncalibrated energy spectra of pixel 16 for the different high voltages. The data is binned to reduce noise and fitting time. Besides the empirical model fit (see equation 4.6), the four characteristics are marked in the spectra. Also the value of each reduced χ^2 is shown. In the lower part of the plots, the residuals are shown.

Here, also the four characteristics and the value of the reduced χ^2 can be seen. The data is binned differently for the different high voltage settings to reduce noise and the fitting time. The binning is shown on the y-axis label. The same was done for pixel 34 in figure 4.8 while here the bin width is much larger, because of the lower statistics. The larger noise in pixel 34 is caused by the worse signal to noise
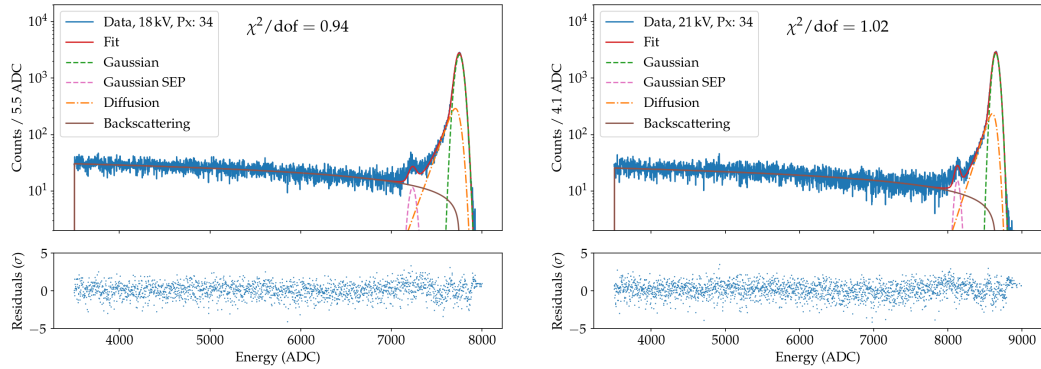
(a) Energy spectrum of pixel 34 of wall electrons at 18 kV high voltage setting.

(b) Energy spectrum of pixel 34 of wall electrons at 21 kV high voltage setting.
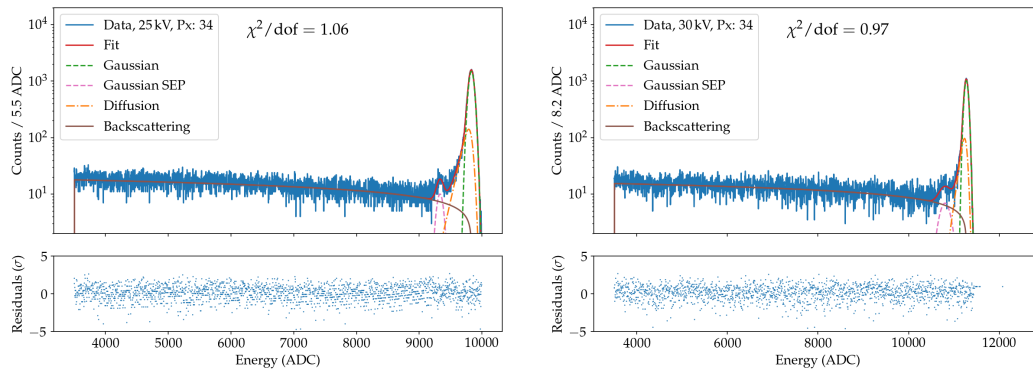
(c) Energy spectrum of pixel 34 of wall electrons at 25 kV high voltage setting.

(d) Energy spectrum of pixel 34 of wall electrons at 30 kV high voltage setting.

Figure 4.8: Uncalibrated energy spectra of pixel 34 for the different high voltages. Besides the empirical model fit (see equation 4.6), the four characteristics are plotted in the spectra. Also, the value of each reduced χ^2 is shown. The data is binned to reduce noise and fitting time. Because of the overall worse signal to noise ratio, the binning is chosen to be larger, and also, the silicon escape peak can not be seen as clearly as for pixel 16. In the lower part of the plots, the residuals are shown.

ratio compared to pixel 16. An effect of the lower statistics is a more smeared silicon escape peak for pixel 34. All fitting parameters at the different high voltage settings for pixels 16 and 34 are shown in figures 4.9 and 4.10. In both figures, the fitting parameter is plotted against the energy in ADC for pixel 16 and 34, representing all working pixels.
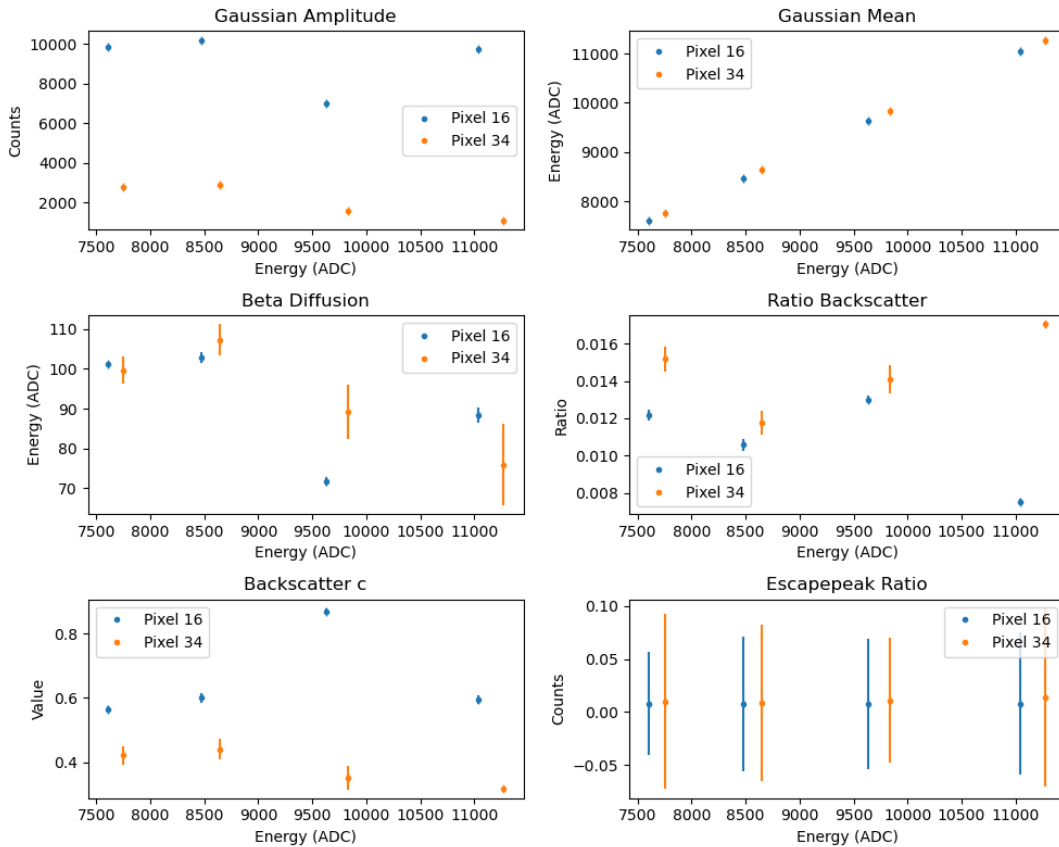
Figure 4.9: Part one of the fitting parameters for pixels 16 and 34 at different high voltage settings given in energy (ADC). These parameters were used for the empirical model function (see equation 4.6) before the calibration.

For the analysis, the high voltage setting at 9 kV is rejected because of the influence of the dead layer onto the energy. At this setting, the electrons scatter more often in the detector entrance window, therefore shift the measured energy and distort the calibration. This effect is not linear with the energy and therefore much larger for low energies. This shift is shown in figure 4.11a, where the energy shift at 9 kV and at 18 kV is plotted for each working pixel. The spectra were calibrated with the measurements at 21 kV, 25 kV and 30 kV. The mean values obtained by the empirical
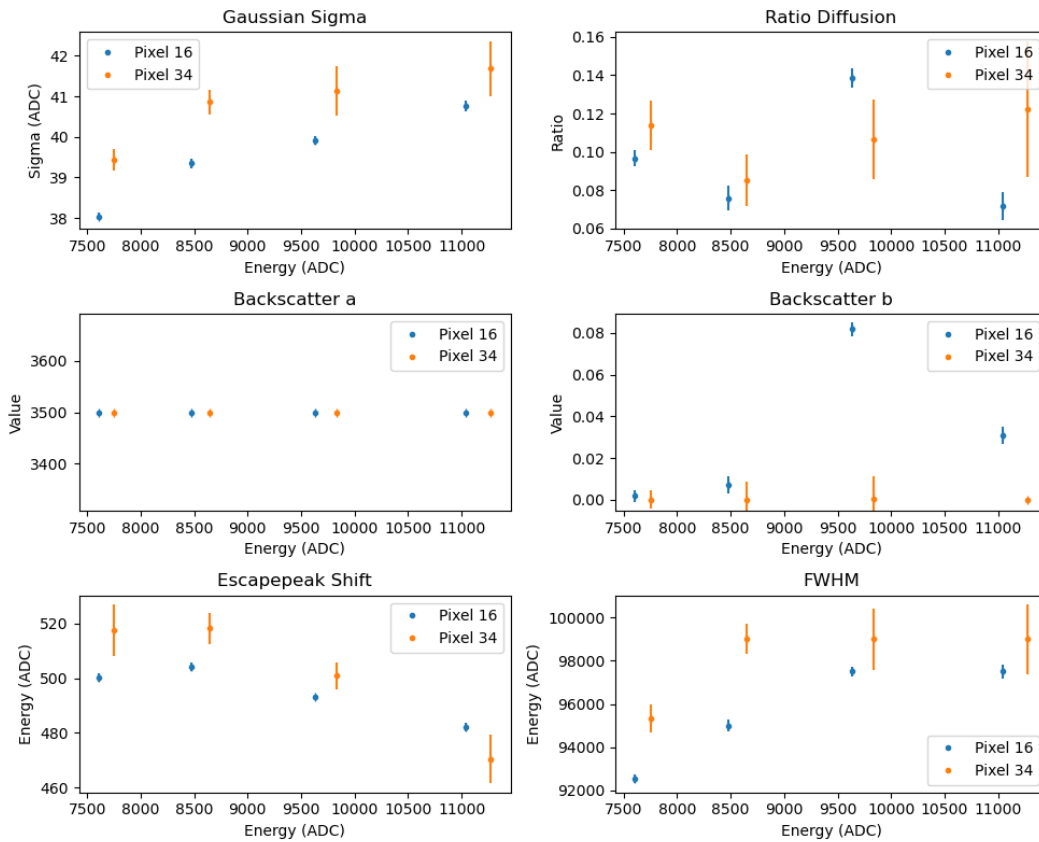
Figure 4.10: Part two of the fitting parameters for pixels 16 and 34 at different high voltage settings given in energy (ADC). These are the remaining parameters used for the empirical model function (see equation 4.6) before the calibration.

model function fitted in the energy spectra of 9 kV and 18 kV were then converted with the calibration parameters from ADC to keV. The deviation of these values to the calibrated value, 9 kV and 18 kV respectively was determined. This calibrated value is not taking the effects of the dead layer into account. The weighted means are (129.06 ± 3.66) eV at 9 kV and (88.09 ± 3.67) eV at 18 kV. The wide spread at 9 kV is caused by the effects of the entrance window. These effects are larger for lower energies, because the electrons have less energies. Therefore, they deposit more of their energy in the dead layer and the mean peak gets shifted. Comparing the obtained energy shift with a simulation [35] investigating the effects of the dead layer, leads to a dead layer of about 80 nm. The results of the simulation are shown in figure 4.11b for different electron energies. Because of the large energy shift at 9 kV, this high voltage setting was not used for further analysis.

(a)

(b)
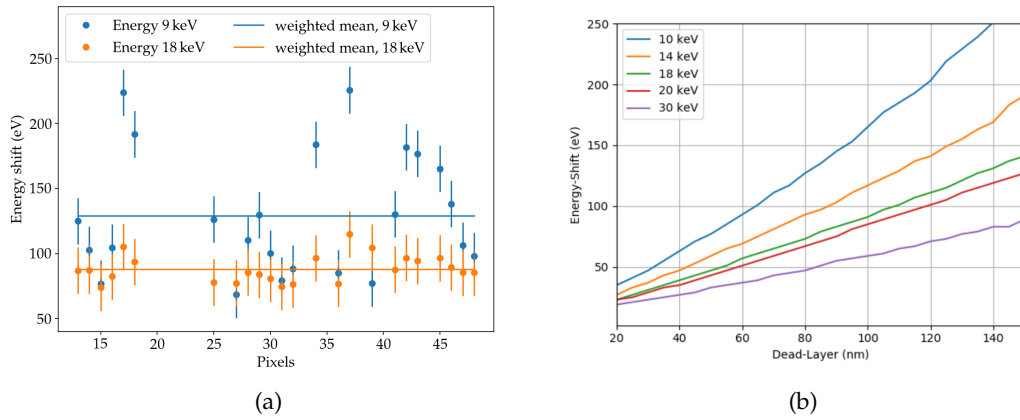
Figure 4.11: Energy shift at two different high voltages. After calibrating with the high voltage settings 21 kV, 25 kV and 30 kV, the energy shift at 9 kV and at 18 kV was determined. a) The energy shift is plotted against the pixels for two different high voltage settings. The spread of the energy shift at 9 kV is caused by larger effects of the dead layer at lower energies. The mean energy shift at 9 kV is (129.06 ± 3.66) eV and at 18 kV is (88.09 ± 3.67) eV. A comparison with the simulation b) taken from [35] indicates a dead layer of about 80 nm. Here the energy shift is plotted against different dead layer thicknesses for five different electron energies.

After fitting the empirical function in the spectra for the different high voltages, the means of the peaks were then used for the linear function (equation 4.7).

$$E_{\mathrm{keV}} = \frac{E_{\mathrm{ADC}} - \mathrm{Offset}}{\mathrm{Slope}}. \tag{4.7}$$

This linear fit is shown in figure 4.12 for pixels 16 and 34. The fit parameters can be found in table 4.2.

Table 4.2: Parameters of the linear fit function for pixels 16 and 34.

Pixel	Slope (eV/ADC)	Offset (ADC)
16	3.515 ± 0.025	-8.813 ± 0.241
34	3.435 ± 0.0296	-8.729 ± 0.295
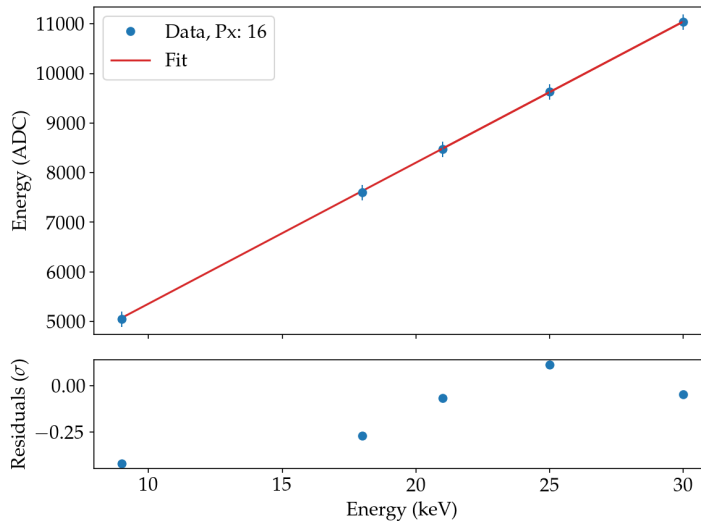
(a) Linear Fit through 18 kV, 21 kV, 25 kV and 30 kV for calibration of pixel 16.
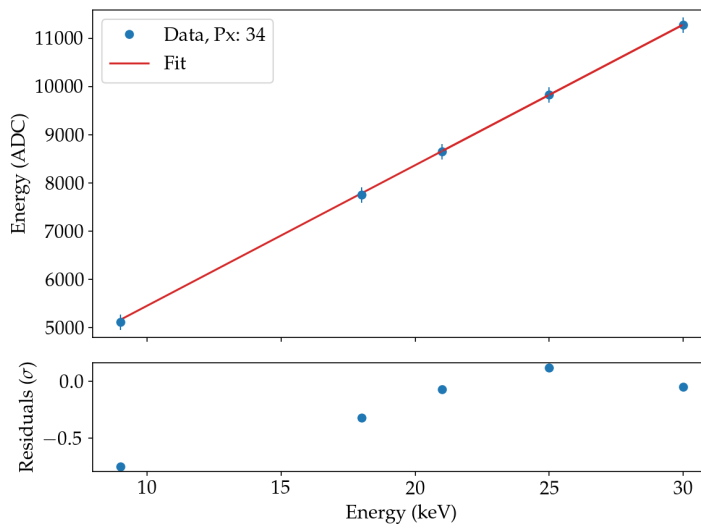
(b) Linear Fit through 18 kV, 21 kV, 25 kV and 30 kV for calibration of pixel 34.

Figure 4.12: Linear fit obtained with the different high voltages for pixels a) 16 and b) 34. For the calibration with this fit the high voltage settings at 18 kV, 21 kV, 25 kV and 30 kV were used. The data taken at 9 kV were still plotted in the figure for comparison. At this lowest setting, the energy shift due to the entrance window can not be neglected.

The high voltage setting at 9 kV was plotted to compare its offset to the linear fit with the other data points and again to illustrate the effects of the dead layer. The obtained fitting parameters for the linear function were used to convert the energy spectra of the wall electrons from ADC to keV. The energy spectra for pixels 16 and 34 for all high voltage settings used for the calibration are plotted in figure 4.13 on top of each other.
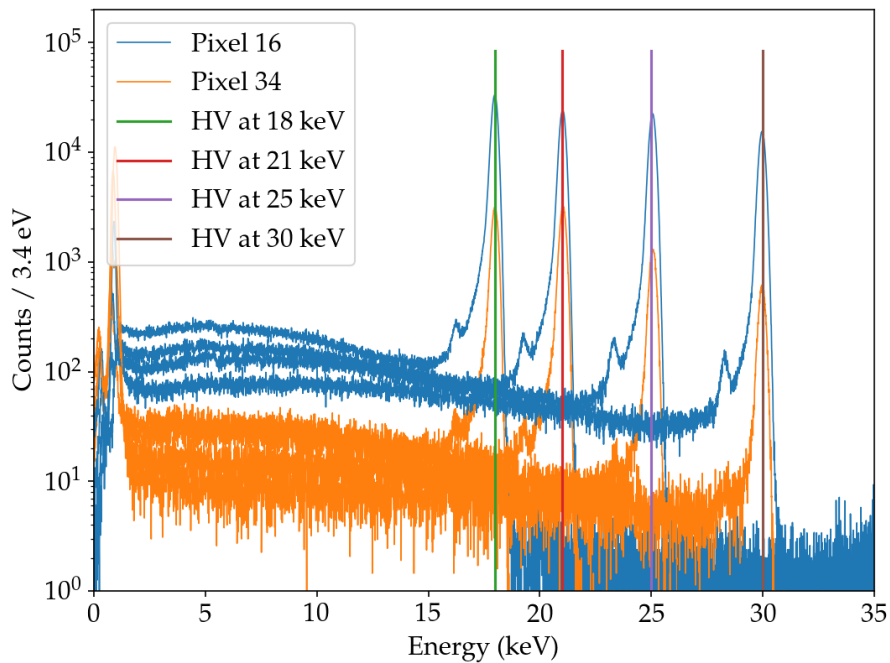
Figure 4.13: Calibrated energy spectra taken with pixels 16 and 34 at all high voltage settings used for the calibration.

Since the primary goal of the wall electron measurement was a rough estimation of the detector response, the energy resolution in terms of the full width at half maximum (FWHM) was determined. In order to obtain this FWHM in eV, the empirical model function (equation 4.6) was now fitted in the calibrated energy spectrum. This renewed fit was done to keep the uncertainties as minimal as possible. Thus, there is no need to consider uncertainty propagation, which would increase the uncertainty when converting the FWHM from ADC into keV. The fitting parameters obtained at the different high voltage settings are plotted against the electron energy in figures 4.14 and 4.15.
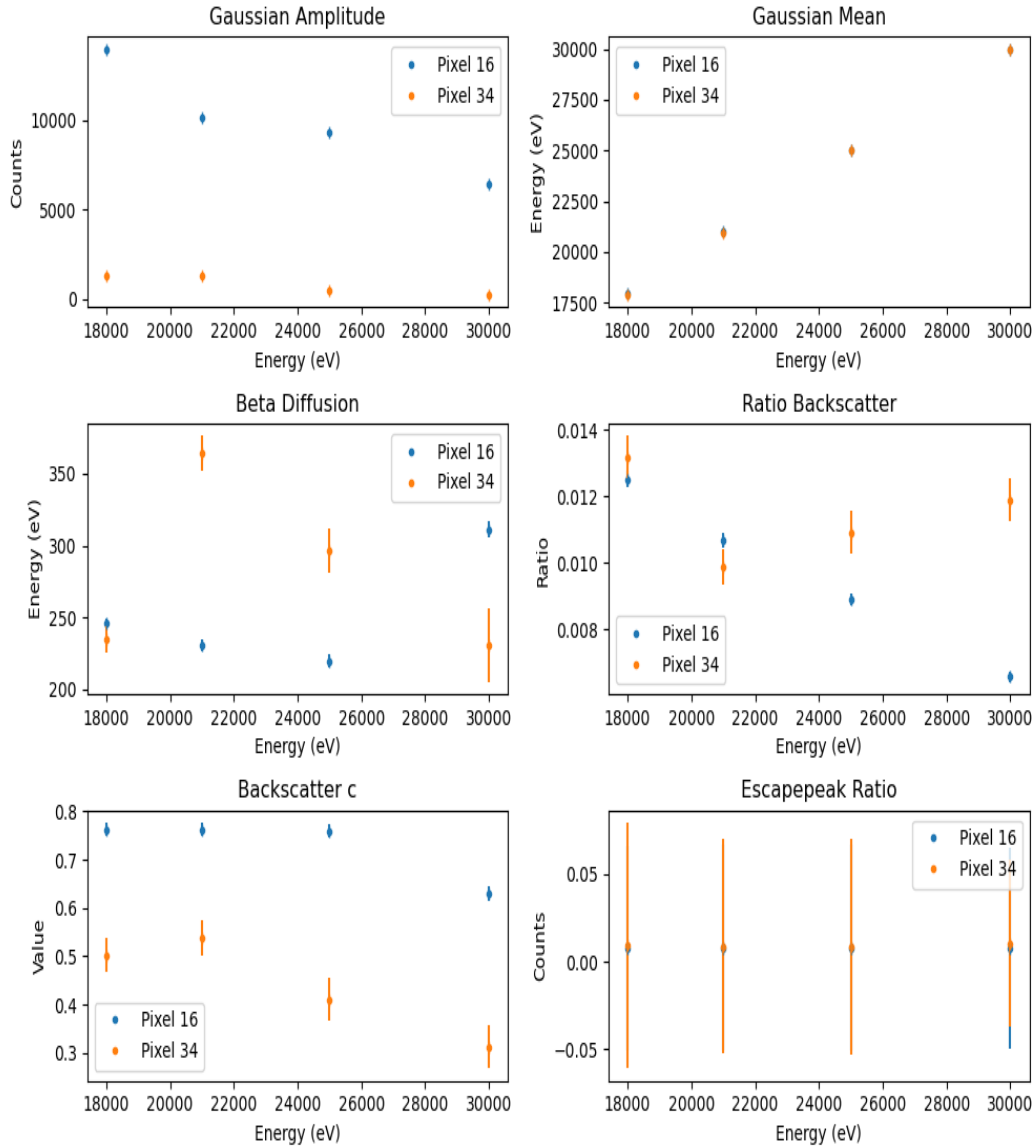
Figure 4.14: Part one of the fitting parameters for pixels 16 and 34 at different high voltage settings given in energy (keV). These parameters were used for the empirical model function (see equation 4.6) after the calibration.
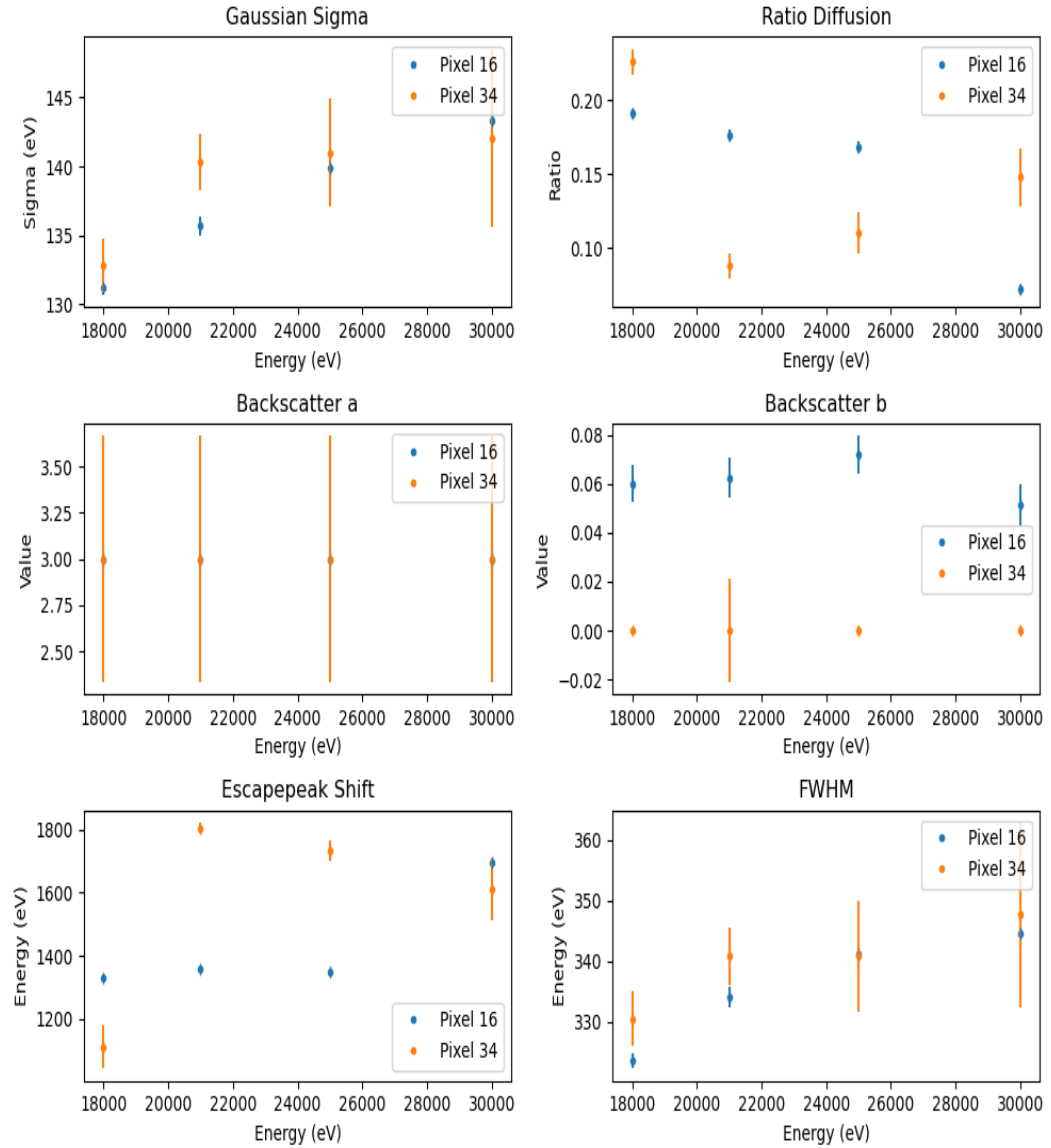
Figure 4.15: Part two of the fitting parameters for pixels 16 and 34 at different high voltage settings given in energy (keV). These parameters were used for the empirical model function (see equation 4.6) after the calibration.

Here again pixels 16 and 34 represent all working pixels. The resulting energy spectra at the different high voltage settings with the fitted empirical model function is shown in figure 4.16 for pixel 16 and in figure 4.17 for pixel 34.
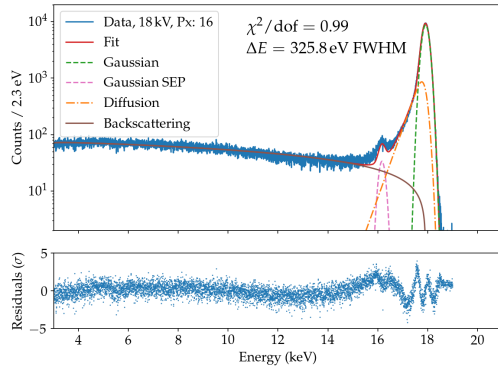
(a) Calibrated energy spectrum of pixel 16 of wall electrons at 18 kV high voltage setting.
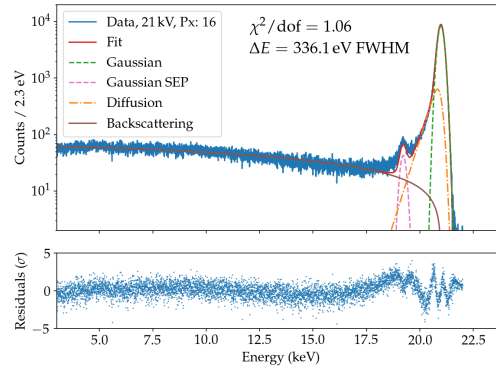
(b) Calibrated energy spectrum of pixel 16 of wall electrons at 21 kV high voltage setting.
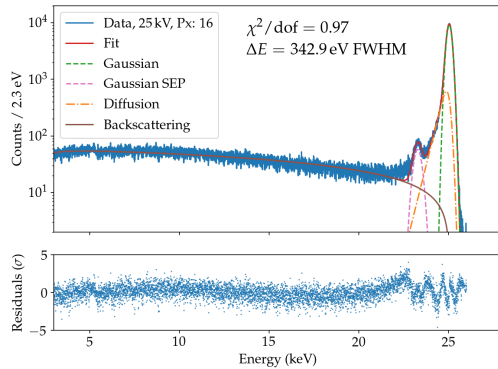
(c) Calibrated energy spectrum of pixel 16 of wall electrons at 25 kV high voltage setting.
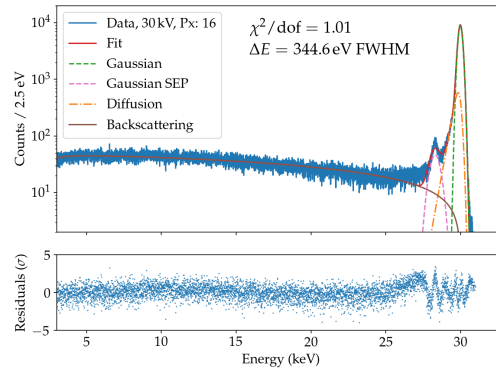
(d) Calibrated energy spectrum of pixel 16 of wall electrons at 30 kV high voltage setting.

Figure 4.16: Calibrated energy spectra of pixel 16 for the different high voltages. Besides the empirical model fit (see equation 4.6), the four characteristics are plotted in the spectra. Also the value of each reduced χ^2 and the FWHM is shown. The data is binned to reduce noise and fitting time. In the lower part of the plots, the residuals are shown.
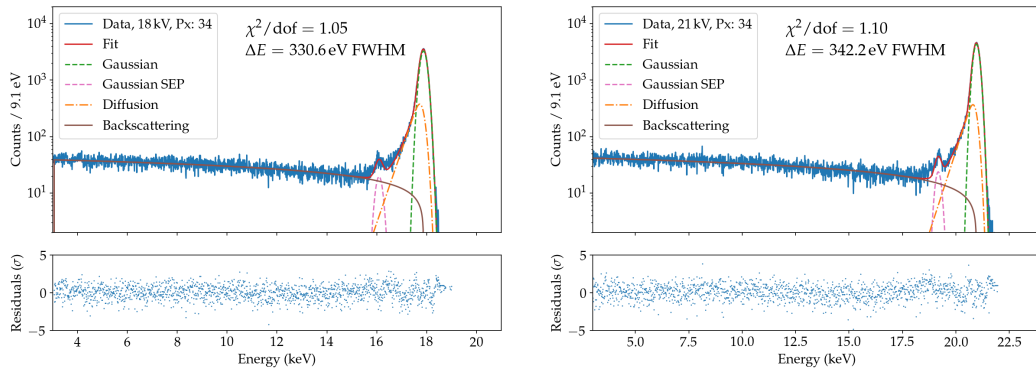
(a) Calibrated nergy spectrum of pixel 34 of wall electrons at 18 kV high voltage setting.

(b) Calibrated energy spectrum of pixel 34 of wall electrons at 21 kV high voltage setting.
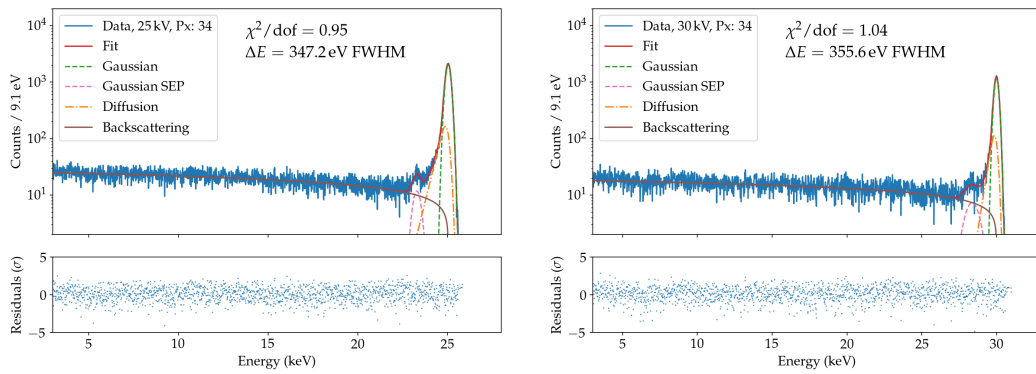
(c) Calibrated energy spectrum of pixel 34 of wall electrons at 25 kV high voltage setting.

(d) Calibrated energy spectrum of pixel 34 of wall electrons at 30 kV high voltage setting.

Figure 4.17: Calibrated energy spectra of pixel 34 for the different high voltages. Besides the empirical model fit (see equation 4.6), the four characteristics are plotted in the spectra. Also the value of each reduced χ^2 and the FWHM is shown. Because of the overall worse signal to noise ratio, the binning is chosen to be larger and also the silicon escape peak can not be seen as clearly as for pixel 16. In the lower part of the plots, the residuals are shown.

A pixel map at 30 kV high voltage with the FWHM for all pixels with a suitable energy spectrum was created and can be seen in figure 4.18. All pixels have an FHWM in a narrow energy range between 300 eV and 400 eV.
For the calculation of the lower limit of the energy resolution for a semiconductor, the Fano-statistic is used. This approach states, that the total width σ of the Gaussian distribution consists of statistical fluctuations σ_{Fano} of the charge carriers and an
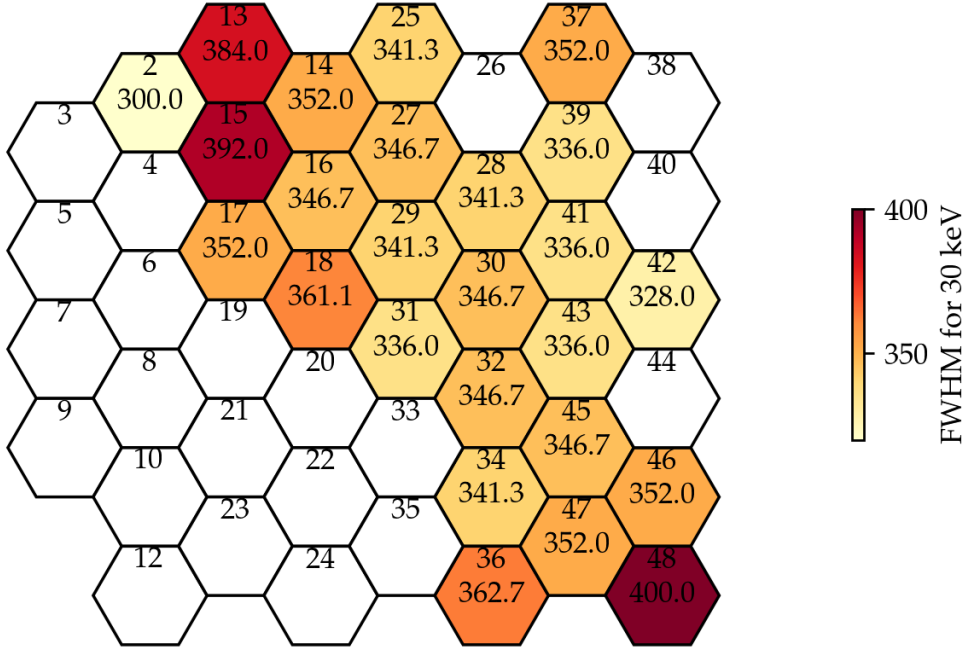
Figure 4.18: Full Width at Half Maximum (FWHM) of energy spectrum with wall electrons at 30 keV energy, color-indexed. The energy spectrum of the white pixels had not shown a clear main peak. Therefore, no FHWM could be determined. The mean energy resolution is (348.67 ± 0.92) eV.

electronic noise σ_{el} [52]. The Fano-limit is calculated with equation 4.8.

$$\sigma_{Fano} = \sqrt{F \cdot w \cdot E_0} \tag{4.8}$$

It depends on the Fano-factor F, which measures the dispersion of a probability distribution, the electron-hole pair generation energy w, and the energy of the electrons E_0 [52]. In detector physics, instead of the total width of the Gaussian distribution, the FWHM is given as a characteristic. Therefore, σ_{Fano} can be converted to $\sigma_{Fano,FWHM}$ with equation 4.9.

$$\sigma_{Fano,FWHM} = 2\sqrt{2\ln 2}\sigma_{Fano} \approx 2.355\sigma_{Fano} \tag{4.9}$$

Both formulae 4.8 and 4.9 only apply if no electronic noise σ_{el} exists. Taking this σ_{el} into account, equation 4.10 is obtained [52].

$$\sigma_{Fano+Noise} = \sqrt{F \cdot w \cdot E_0 + \sigma_{el}^2} \tag{4.10}$$

53

Also this value can be expressed in terms of FWHM, showed in equation 4.11.

$$\sigma_{Fano+Noise} = 2\sqrt{2\ln 2}\,\sigma_{Fano+Noise} \tag{4.11}$$

The detector was not cooled in this measurement, therefore, a Fano-factor of $F = 0.12$ at $T = 300\,\text{K}$ was used to calculate the Famo-limit. With an electron-hole pair energy of $w = 3.64\,\text{eV}$ at this temperature and an energy of the incoming electrons of $E_0 = 30\,\text{keV}$, the Fano-limit results in

$$\sigma_{Fano} = \sqrt{F \cdot w \cdot E_0} = 114\,\text{eV}. \tag{4.12}$$

From this a $\sigma_{Fano,FWHM}$ of

$$\sigma_{Fano,FWHM} = 2\sqrt{2\ln 2}\,\sigma_{Fano} \approx 269.56\,\text{eV} \tag{4.13}$$

is received.
The electronic noise of the TRISTAN detector at $T = 300\,\text{K}$ is estimated to $\sigma_{el} \approx 104\,\text{eV}$. The Fano and noise limit is then resulting in equation 4.14.

$$\sigma_{Fano+Noise} = \sqrt{F \cdot w \cdot E_0 + \sigma_{el}^2} \approx 155\,\text{eV} \tag{4.14}$$

The electronic noise was calculated by subtracting $\sigma_{Fano,FWHM}$ from the FWHM coming from the data. This can also be called $\sigma_{Fano+Noise,FWHM}$.

$$\sigma_{Fano+Noise,FWHM} = 2\sqrt{2\ln 2}\,\sigma_{Fano+Noise} \approx 364\,\text{eV}. \tag{4.15}$$

Figure 4.19 shows the calculated Fano-limit with the obtained FWHM of two exemplary pixels. The FWHM in terms of resolution is plotted against the different electron energies. Therefore equations 4.9 and 4.11 are used. The data lies in a similar range as the theoretical values. The deviation could be caused by the simplified assumptions when calculating the theory values. Another possibility is a deviation because of the energy dependence of the electronic noise.

4.2.2 Electron Gun

In general, an electron gun (e-gun) in the KATRIN experiment can be used for commissioning purposes of several parts of the beamline. It is based on the emission of electrons coming from a metallic photo cathode illuminated by UV light and emits electrons by photo emission. The electrons are emitted in a pulsed, point-like beam with small energy and narrow angle distribution, and a strong electric field accelerates them non-adiabatically. It has a homogeneous electric acceleration field, and by tilting it against the magnetic field lines, the generated electrons can be forced into a precisely defined tilt angle. [32]
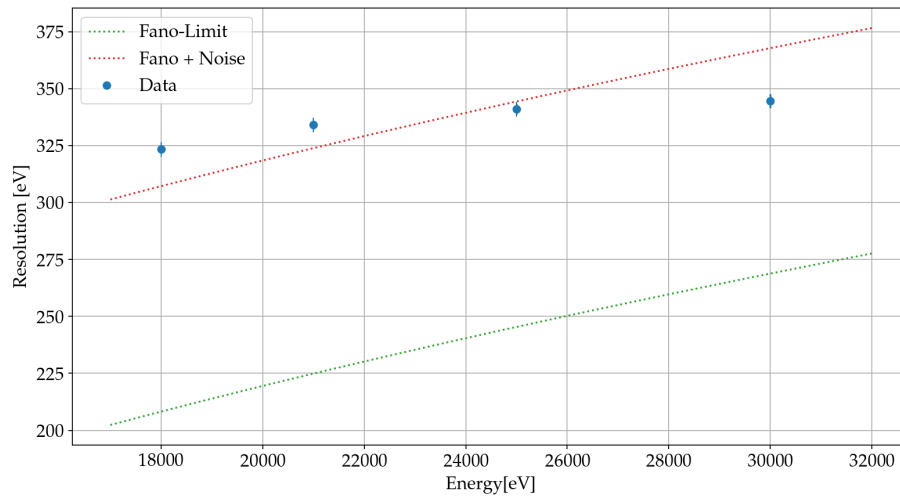
(a) Fano-limit of pixel 16.
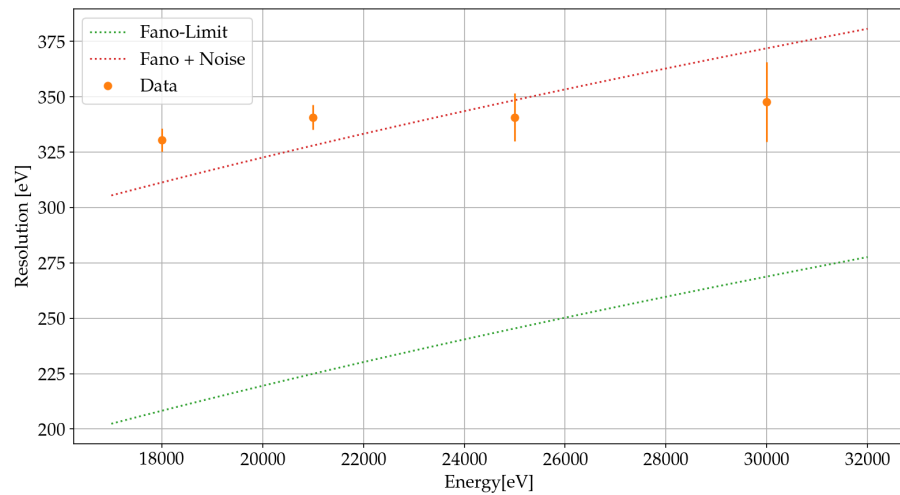
(b) Fano-limit of pixel 34.

Figure 4.19: Fano-limit of the TRISTAN prototype detector. The FWHM as the resolution of a) pixel 16 and b) pixel 34 are plotted against the energy of the incoming electrons. Also the Fano-limit and the Fano and electronic noise limit are shown in terms of the FWHM.

Figure 4.20 shows a sketch of the detailed structure of the electron gun. The planar photo cathode gets illuminated from the backside with UV light coming from a single optical fiber. The wavelength in the electron sources can be set to the work
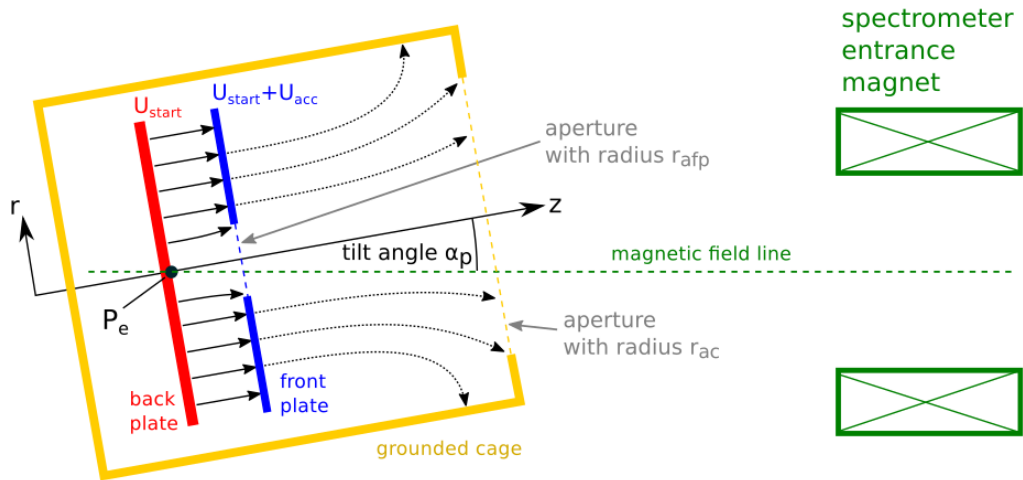
Figure 4.20: This drawing shows the path of the electrons inside the electron source. A photo cathode emits electrons by photo emission. Those electrons are accelerated non-adiabatically by a strong electric field. The solid arrows between the back and the front plate represent the electric field lines. The plate capacitor is placed inside a grounded cage to avoid external influences. The dotted arrows stand for the acceleration between the front plate and the cage. The electrons reach their nominal kinetic energy. The entire setup can be tilted against the magnetic field lines to force the electrons into a precisely defined tilt angle. Image is taken from [32].

function Φ of the photo cathode material oriented to equation 4.16

$$\lambda \lesssim \frac{hc}{\Phi} \qquad (4.16)$$

with h as the Planck constant and c as the speed of light. The work function is the minimal thermodynamic work or energy that an electron needs to leave a solid to the vacuum close to the surface.

For the metallic surfaces used for the integrated electron source, the work function is $\Phi < 5\,\text{eV}$ [32]. With the emission point p_e on the back plate set on a high electric negative potential typically at $U_{\text{start}} = -18.6\,\text{kV}$ [30] the kinetic energy of the generated electrons is defined by equation 4.17.

$$E_{\text{kin}} = qU_{\text{start}} \qquad (4.17)$$

The energy distribution of the emitted electrons is defined over the photon energy (see equation 4.18) and the work function Φ (equation 4.19)

$$h\nu = \frac{hc}{\lambda}. \qquad (4.18)$$

In this equation ν stands for the frequency. With this one obtains

$$0 < E_e \le h\nu - \Phi = \frac{hc}{\lambda} - \Phi. \tag{4.19}$$

The observed or effective work function can be significantly reduced by surface roughness and impurities caused by absorbed gas molecules.

For a slightly larger photon energy $E_\gamma = h\nu$ than work function Φ, emitted electrons have a smaller, narrowly distributed energy in the 1 eV range. The electropolished front plate is $d_{fp} = 2$ mm thick and its aperture has a radius of $r_{afp} = 3$ mm. The also electropolished backplate has a thickness of $d_{bp} = 3$ mm and the possibility to build a photo cathode holder in the center. Both plates have a radius of $r_p = 30$ mm and a distance of 10 mm from each other [32]. This photo cathode holder features an aperture for an optical fiber and has a diameter of 200 μm. Both plates are isolated against each other and are placed inside a grounded cage to shield them against disturbances. The cage consists of polyether ether ketone (PEEK).

A precise high voltage supply minimizes the fluctuations and leads to a constant electrical acceleration field at the photo cathode. This remains even when the plate setup is tilted a few degrees against the magnetic field at the emission point. It allows covering a certain range of electron inclination angles between $\theta = 0°$ to $90°$ at the tilt magnet. The electrons get therefore accelerated adiabatically towards the ground potential at the spectrometer entrance, as explained in section 2.1, and reach their maximum kinetic energy of about 18.6 keV [30]. One of the main characteristics of the electron gun is the angular sensitivity that defines a definite tilt angle between the electron momentum p and the magnetic field B. The entire setup can be tilted mechanically against the direction of the magnetic field direction. [32]

The Lorentz equation 4.20 describes the domination of the electrostatic acceleration over the electron propagation because of their low kinetic energy directly after the emission.

$$\mathbf{F} = q(\mathbf{E} + \mathbf{v} \times \mathbf{B}) \tag{4.20}$$

The electrons with charge q follow a $\cos \theta$ angle distribution with small velocity $\mathbf{v}$ which leads to a small Lorentz force $\mathbf{F}$ influenced also by the electrostatic field $\mathbf{E}$ and the magnetic field $\mathbf{B}$ [30]. This initial energy distribution defines the energy spread in the entrance magnet and shifts the kinetic energy by qU_{start} while the spectral form of the initial distribution remains unaffected. [32]

The main characteristic of the electron gun is not only the energy E and the tilt angle θ but also the electron rate R_g. This rate should be as stable as possible, meaning there should be $< 0.1\%$ fluctuations over several hours. Intensity changes of the UV-light source, like warm-up effects, cause those fluctuations in the electron rate and can worsen the energy resolution.

Another problem concerning the electron rate are stored electrons between the

spectrometer and the electron source. These electrons are reflected by the electrical retarding potential on the analyzing plane or by the magnetic field at the spectrometer entrance acting like a penning trap. The electrons can lead to problems like discharge in the photo cathode. A dipole electrode in the beamline between the source cage and the entrance magnet avoids these traps. It creates an induced electric field **E** causing the stored electrons to drift.
The operation of the electron gun under vacuum conditions is possible with the help of two air pressure linear motors outside the vacuum chamber. [32]

4.2.3 Krypton Source

The third electron source that can be operated inside the monitor spectrometer is a krypton source. The rubidium isotope ^{83}Rb serves as a generator for the isomer krypton ^{83m}Kr of krypton. The parent isotope rubidium converts to krypton via electron capture. The second excited state of ^{83}Kr has a half-life of $T_{1/2} = 1.83\,\text{h}$ and is created with a branching ratio of about 74(5) % [53]. As illustrated in figure 4.21, the captured electrons cause two electromagnetic transitions with energies of 32.2 keV and 9.4 keV, creating a large amount of conversion electrons.
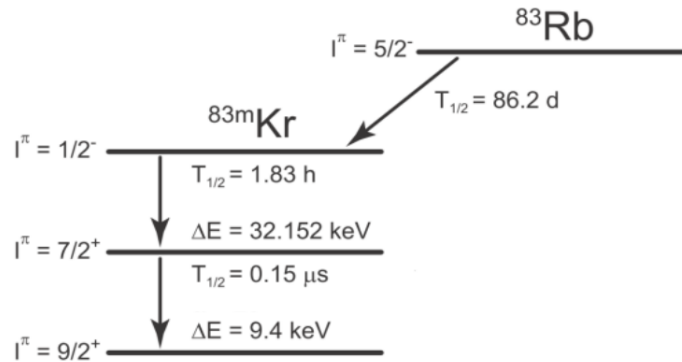
Figure 4.21: Conversion of ^{83}Rb into ^{83m}Kr by capturing an electron. The excited isotope releases two γs to reach the ground state. I represents the Isospin and $T_{1/2}$ the half-live. ΔE is the transition energy. Adapted figure taken from [46].

The ratio of conversion electrons to photon de-excitation is 2035 for the 32.2 keV transition and 17 for the 9.4 keV transition [47]. This high ratio makes the 32.2 keV transition more attractive as an electron source.
It is essential to know the precise kinetic energy of the conversion electron E_i emitted from the atom orbit i in equation 4.21.

$$E_i = E_\gamma + E_{\gamma,rec} - E_{e,rec} - B_i^{vac} \tag{4.21}$$

This energy is composed of the photon energy E_γ, the binding energy of the electron in the free atom B_i^{vac} and the recoil energies of the atom after emitting the gamma ray $E_{\gamma,rec}$ and the electron $E_{e,rec}$. In figure 4.22, the conversion electron energies and their intensity per ^{83m}Kr decay are shown. The nuclear transitions of the same
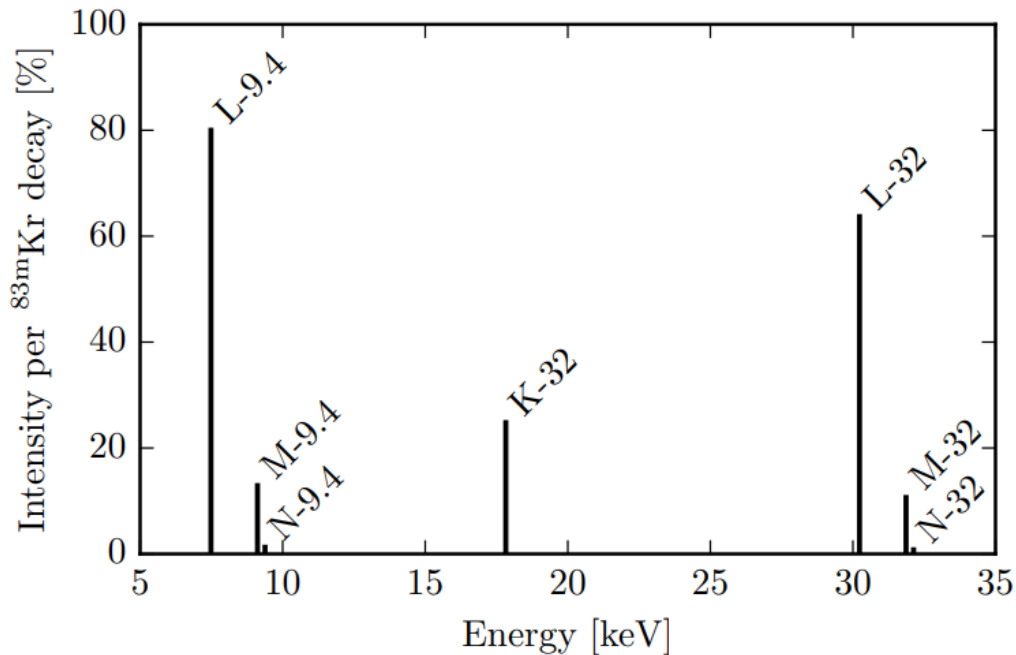
Figure 4.22: Discrete conversion electron spectrum of ^{83m}Kr. The intensities of the same nuclear transitions from the same electron shell are summed up. No Auger electrons are shown. Figure taken from [47].

electron shell are summarized. The $L - 32$ transition is the nuclear transition of the L shell and consists of transitions from three atom orbitals, L_1 from the $2s_{1/2}$ orbital, L_2 from the $2p_{1/2}$ orbital and L_3 from the $2p_{3/2}$ orbital. Because of the lower intensity of the L_1 transition compared to the L_2 and L_3 transitions, it is neglected in the formation of the mean value, later. The $M - 32$ line summarized five nuclear transitions of the M shell. The orbitals are $3s_{1/2}$, $3p_{1/2}$, $3p_{3/2}$, $3d_{3/2}$ and $3d_{5/2}$. Here because of their low intensities, the M_1, M_4 and M_5 transitions were neglected in the calculation of the mean value. The values of each single nuclear transition are shown in table 4.3.

For the usage in the monitor spectrometer, the ^{83}Rb is evaporated onto a thin layer of a Highly-Oriented Pyrolytic Graphite (HOPG) substrate. Surface effects of the HOPG substrate influence the kinetic energy of the conversion electrons. Therefore,

Table 4.3: Conversion electrons in ^{83m}Kr decay for nuclear transitions of the $L - 32$ and $M - 32$ shell. Values taken from [53].

Line	Conversion electron energy E_i (eV)	Intensity I_i per decay (%)
L_1	30226.8 ± 0.9	1.56 ± 0.02
L_2	30419.5 ± 0.5	24.3 ± 0.3
L_3	30472.2 ± 0.5	37.8 ± 0.5
M_1	31858.7 ± 0.6	0.249 ± 0.004
M_2	31929.3 ± 0.5	4.02 ± 0.06
M_3	31936.9 ± 0.5	6.24 ± 0.09
M_4	32056.4 ± 0.5	0.0628 ± 0.0009
M_5	32057.6 ± 0.5	0.0884 ± 0.0012

control and monitoring of the evaporated layer and minimization of contamination by remaining gas molecules is essential. [30]

The advantages of an evaporated source are the avoidance of contamination, its simplicity in handling because of its small size, and its reliability [46]. The sources are obtained from the BONIS facility in Bonn [47]. This facility only executes the mass separation and the implantation of the rubidium. The rubidium is then dissolved in water inside a cylindrical tungsten furnace. The furnace gets transported to Bonn and is placed inside an ion source. This ion source is under high voltage of about 30 kV to 40 kV. Due to the impact of electrons emitted by two coil-shaped tungsten electrodes, the furnace is heating up, and the rubidium evaporates at the bottom of the furnace. [47]

The source holder in the monitor spectrometer on an insulated tip of a long tube is welded into a base flange. The holder has space for four sources on a ceramic disc. Each of the four slots has its cable covered in polytetrafluoroethylene (PTFE). With this, up to -770 V can be biased to close the gap between the K-32 energy of about 17830 eV and the tritium endpoint at about 18600 eV. A cross-table moves the built-in base flange in the axial direction. Its latitude in the vertical and horizontal direction is ± 20 mm. [54].

The high intensity of the $L - 32$ line per ^{83m}Kr decay, as shown in figure 4.22, causes a minor background of higher lines such as $M - 32$ and $N - 32$ and is therefore suitable to investigate the line shape. This is one reason ^{83m}Kr is used for TRISTAN detector characterization measurements. Another reason is the high amount of emitted conversion electrons when decaying into the ground state. Those electrons have suitable energies and line width and are measurable in the MAC-E filter. Also, because of the short half-live of this isotope, there is no risk of contamination of the experimental setup. Further, the isotope is practically and in a sufficient amount producible.[47]

An exemplary [83m]Kr source that was used for the detector investigations in this thesis, is shown in figure 4.23.

Figure 4.23: Photograph of a krypton source used for calibration purposes in the KATRIN monitor spectrometer. The source is evaporated onto a Highly-Oriented Pyrolytic Graphite (HOPG) substrate. It has a diameter of about 12 mm and a thickness of 0.5 mm. Picture shown in [55].

5 Characterization of a TRISTAN SDD in the Monitor Spectrometer

The primary goal of the TRISTAN project is to improve the lower limit down to a sensitivity of $\sin^2(\theta_{41}) = 1 \cdot 10^{-6}$ for sterile neutrinos in the keV-mass range. To reach such a sensitivity, the detector needs to be understood to the same level. Therefore, the first characterization measurements with electrons were performed with the 47-pixel 3D prototype detector to understand the detector response better. The main task of this thesis was to analyze the electron response of this detector. An overview of the measurement campaign is given in section 5.1. In section 5.2 the selection of the data taken for further analysis is explained. The first step in the analysis was the calibration of the data (section 5.3). The two different methods used in this thesis are calibration with two simple Gaussian functions (section 5.3.1) and calibration with an empirical model function, explained in section 5.3.2.
The main part of the analysis was then a combination of the data to investigate the stability over time (section 5.4.1) and the stacking of the pixels (section 5.4.2).

5.1 Measurement Overview

In May 2021, a measurement of a ^{83m}Kr-source was started to investigate the stability of the detector by looking at the $L - 32$ and $M - 32$ line of ^{83m}Kr. The overall goal of this measurement was to understand the electron response of a TRISTAN detector in the MAC-E-filter environment. Influences on the detector are, amongst others, the magnetic field and the vacuum. Therefore, the 47-pixel 3D prototype and a krypton HPOG source were assembled in the monitor spectrometer (section 4.1). The measurement lasted about 66 h, recording one-hour timed spectra measurements with two seconds pause.
The source voltage is kept at $-1\,\mathrm{kV}$, and the vessel voltage was set to $-31.440\,\mathrm{kV}$, just about 25 V below the M line. The air coils were turned off for the measurements, and the EMCS was turned on at 11 G to compensate for the Earth's magnetic field.

The vacuum in the source chamber did not reach its initial value of $2.8 \cdot 10^{-7}$ mbar when the measurement was started but improved over time.

5.2 Data Selection

First, the count rates were determined after the first 15 h of measurement in order to be able to exclude any pixels that were not functional. The color-indexed figure 5.1 shows the total count rate of all pixels after 15 h.
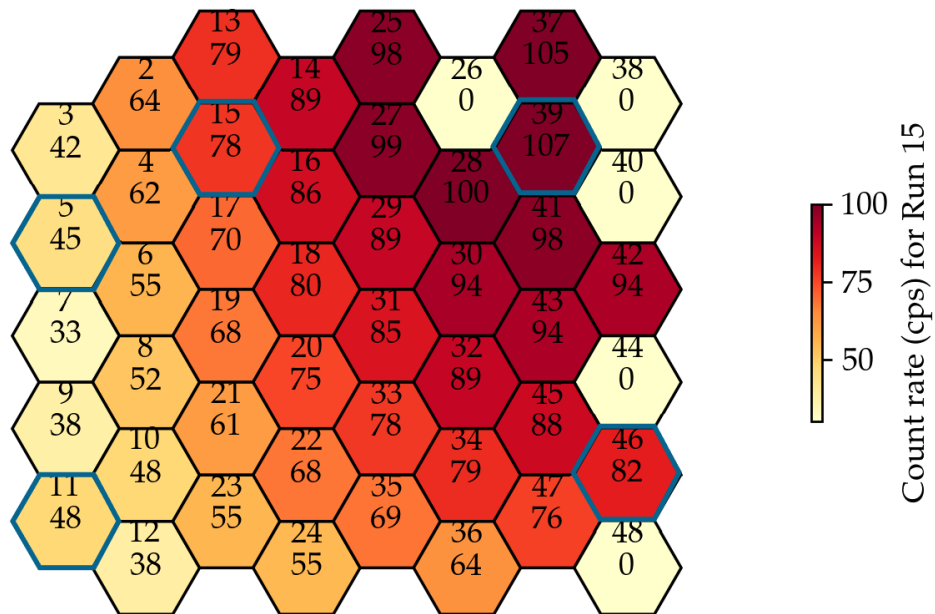
Figure 5.1: Total count rate of ^{83m}Kr recorded with a TRISTAN detector after 15 h of measurement. The plot is color-indexed, and the brightest pixels were disabled and showed no count rate and energy spectrum. The blue-bordered pixels showed nonphysical features and were therefore excluded from the analysis. The first pixel is missing because it was only the control pulser and did not exist on the detector.

The upper number in the pixel map stands for the pixel, while the lower one stands for the count rate. The brightest pixels had no count rate since they were disabled due to problems on the waveform level. In total, the pixels 26, 38, 40, 44, and 48 had issues with the waveform. For these pixels, no signal was visible, and therefore no spectrum was obtained.

A broad energy spectrum of ^{83m}Kr electrons taken with a working pixel at a retard-

ing potential of $-31.440\,\text{kV}$ is shown in figure 5.2. The highest peak in this spectrum
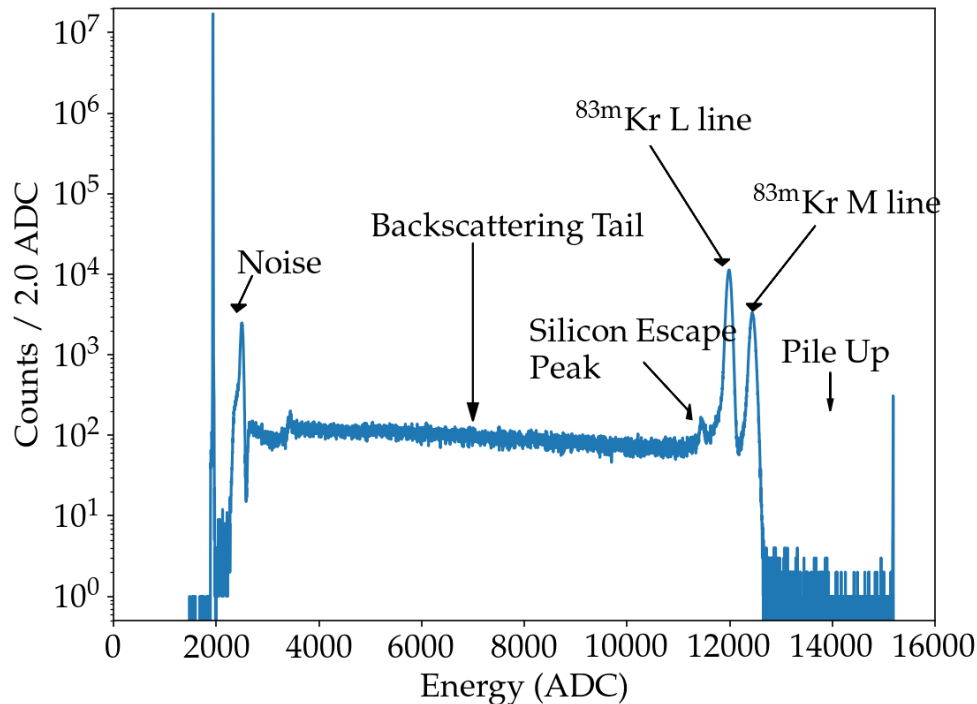
Figure 5.2: Energy spectrum of the L and M line of $^{83\text{m}}$Kr. Six distinct regions can be identified. The first three already occurred with wall electrons, the noise, the backscattering tail, and the silicon escape peak (SEP) in section 4.2.1. The two main peaks represent the nuclear transition of the conversion electrons at de-excitation in the $^{83\text{m}}$Kr. The first one shows the L line, and the second one is the M line. At high energies, the pileup region is present, where events occur faster than the fast filter can distribute them. So, the fast filter recognizes them as one event instead of separate ones with higher energy.

is the conversion electron line of the L while the last peak is the conversion electron line of the M transition [53]. The minor peak in the energy spectrum represents the silicon escape peak (SEP) coming from the L line. A second one from the M line is hidden in the L line peak. This silicon escape peak also occurs for wall electrons, so its origin is explained in section 4.2.1. The almost constant part following in the spectrum is the so-called backscattering tail (see section 4.2.2). It is mainly caused by electrons entering the detector, depositing only part of their energy, and leaving

the detector again. Because of the MAC-E filter, these electrons can hit the detector a second time and again deposit part of their energy in the detector. The noise peak is present at low energies, where all events with lower energy than the set threshold are collected. In the high-energy region of the spectrum, the pileup is located. Here are all the events that were too close together, so the fast filter could not distinguish them, sums them up, and does not recognize them as separate events. Further, the highest bin of the DAQ is located here. It collects all events with higher energies than the DAQ can read out.
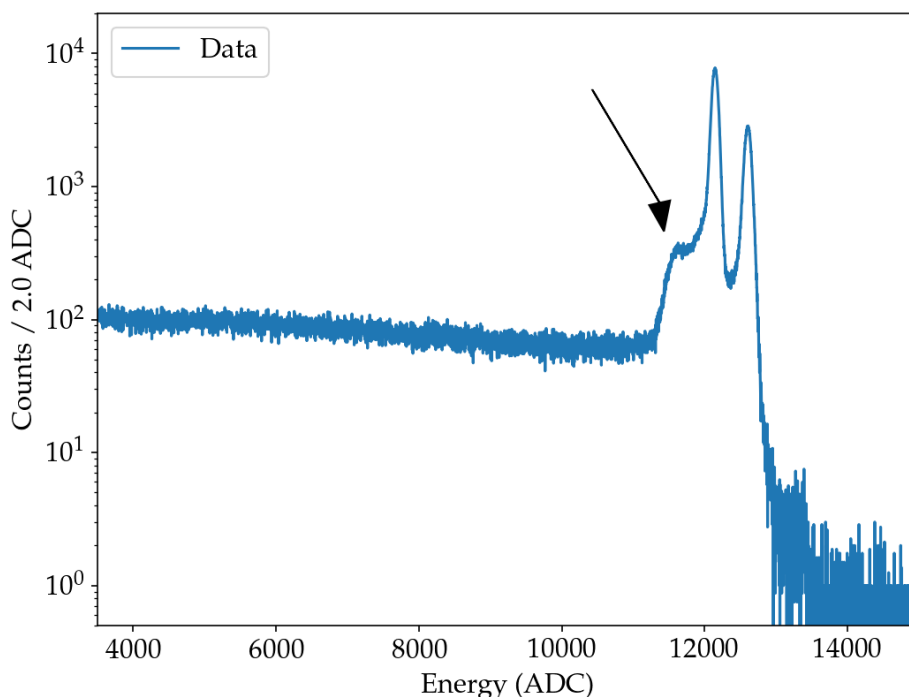
Figure 5.3: Energy spectrum of pixel 46 showing a nonphysical behavior. Instead of the silicon escape peak, a bump is visible. These pixels had issues with the DAQ settings. They are therefore not suitable for a precise analysis of the detector response.

The blue-bordered pixels in figure 5.1 showed some nonphysical features in their energy spectra. For example, like pixel 46 in figure 5.3, a bump occurred at the position of the SEP. This bump was caused by issues with the DAQ settings of these

pixels and was resolved in later measurements. Therefore they were excluded from the analysis.

After fitting the simple Gaussian functions in section 5.3.1 in the energy spectra of all working pixels, the obtained peak height of the L line was plotted against the time for each working pixel to analyze the stability of the measured count rate. The Gaussian amplitude represents this count rate. The different heights of the curves in figure 5.4 are caused by the different locations of the pixels in the beam.
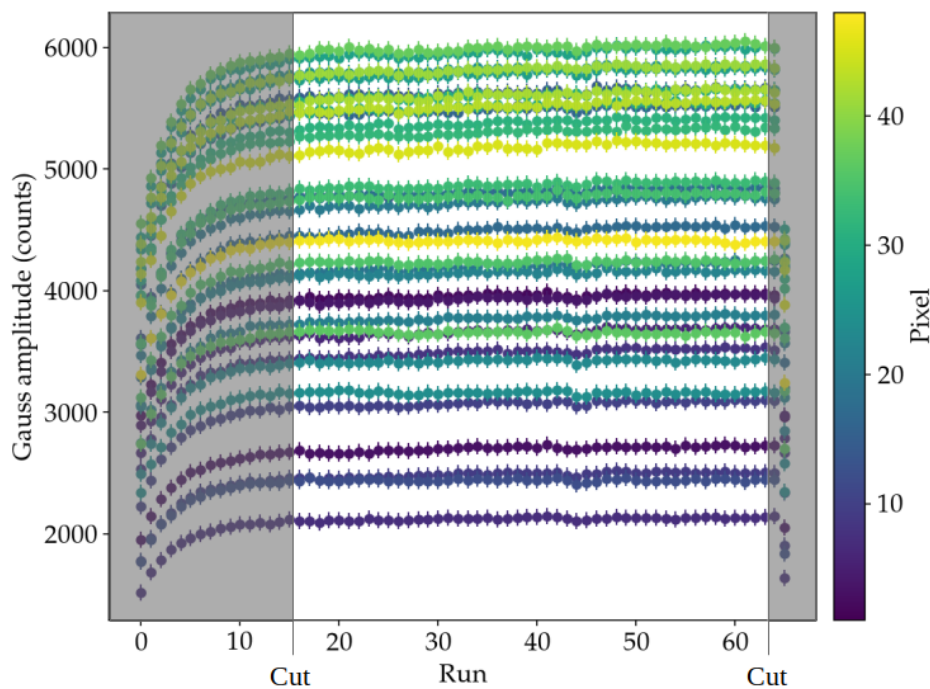
Figure 5.4: Counts represented by the Gaussian amplitude against time represented in runs for each pixel. Each run stands for one hour of data taking. The color denotes the pixel number. The grey areas show the runs that were cut off for the further analysis.

An increase in the counts for all pixels is visible in the first 14 h, while the number of counts drops rapidly in the last hour. The increased count number is not yet clarified and must be further investigated. Possibly the vacuum plays a role in how the electrons can scatter from air molecules. The low count number in the last run could occur from the measurement not lasting a full hour. For these reasons, the first 14 h, and the last 3 h were cut out to gain a constant region for stability analysis.

Another critical issue in stability measurements is the stability of the Gaussian
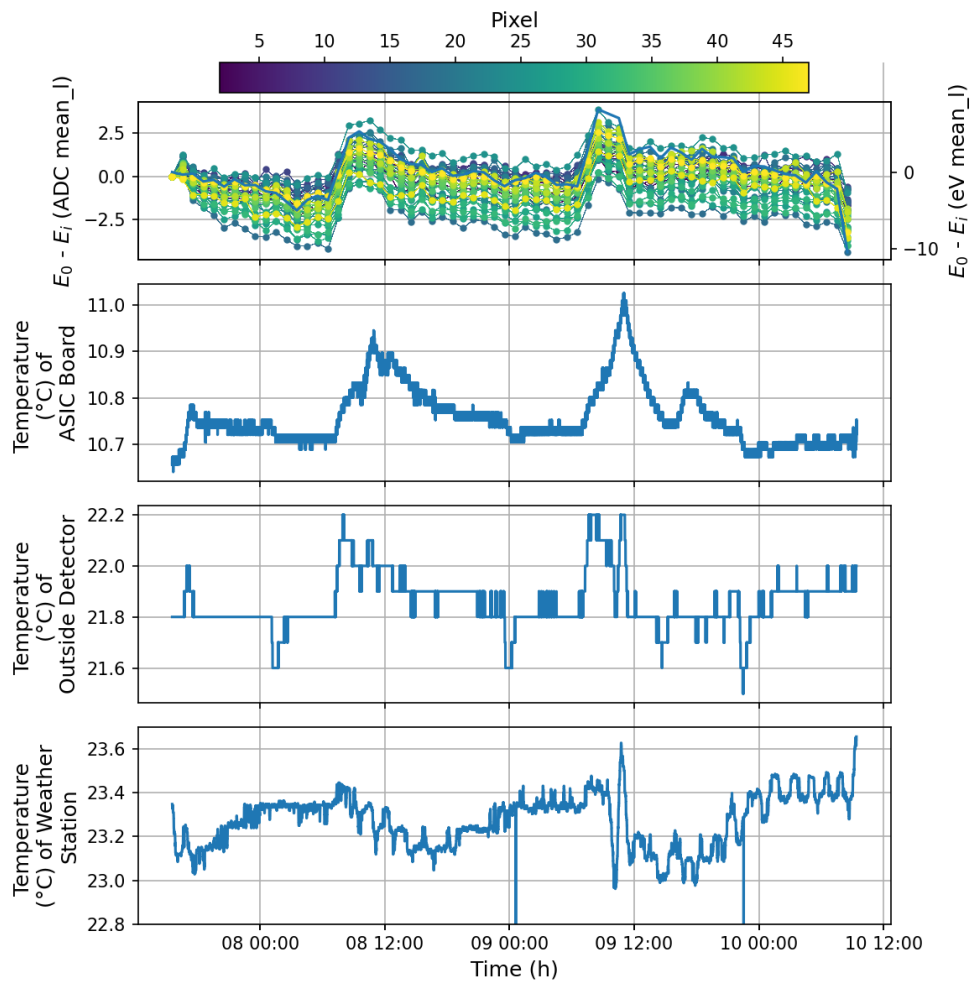
Figure 5.5: Gaussian mean of the L line over time and the different temperatures of the setup over time. There appears to be a correlation between the mean and the temperature. For this analysis, the mean fluctuation is negligible because it only varies about $\pm 10\,\text{eV}$ around the mean of a few keV. It can be concluded that with a variation of about $0.5°\,\text{C}$, the effect on the L line energy is small enough to neglect.

mean over time. The Gaussian mean of the L line represents the L line energy. Therefore possible influences have to be detected. For example, figure 5.5 shows a possible correlation between the temperature on the ASIC board, the temperature outside but close to the detector, and the temperature on the opposite side of the room.

For the analysis done in this thesis, the influence of temperature was negligible, as it caused the overall mean value to vary by only $\pm 10\,\text{eV}$. This is a small value compared to the L line energy of about $(31.4515 \pm 0.0004)\,\text{keV}$. This value is taken from [53] by calculating the mean weighted by the intensities I of the L_2 and L_3 line with equation 5.1.

$$L_{\text{weighted}} = \frac{E_{L_2} \cdot I_{L_2} + E_{L_3} \cdot I_{L_3}}{I_{L_2} + I_{L_3}} \tag{5.1}$$

It is essential to understand the effect of the temperature on the detector. Therefore it is crucial to further investigate a possible temperature correlation in the future. Nevertheless for the scope of this thesis, the effect of the temperature fluctuation on the peak position is negligible.
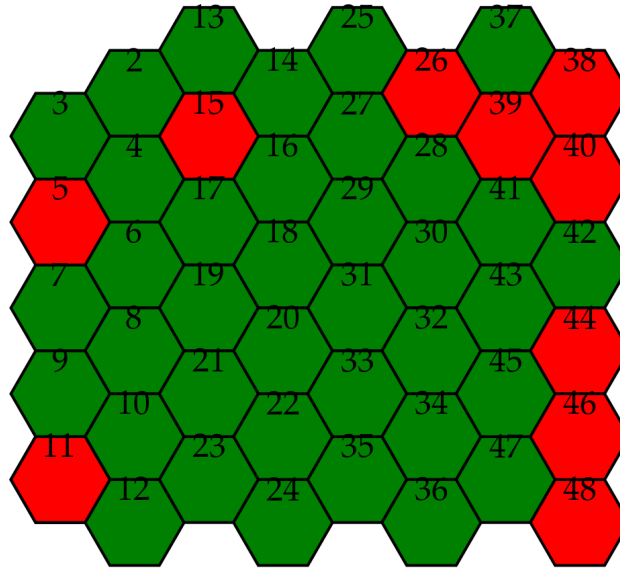
Figure 5.6: Pixel map of working and not working pixels. The green ones showed a suitable energy spectrum, while the red pixels either had no energy spectrum or showed a bump in the SEP region. They were therefore excluded from the analysis. The first pixel was only the control pulser and did not count into the detector module. Therefore it is not shown in the pixel map.

A pixel map with used and unused pixels was created following these before mentioned considerations. It can be seen in figure 5.6. The green pixels had a reasonable energy spectrum, while the red pixels were either broken or had nonphysical issues.

5.3 Data Calibration

Further analysis was done using only the working pixels with a constant count rate for the stable measurement period (see section 5.2). For the complete analysis, two different calibration methods were considered. At first, the recorded energy spectrum was calibrated with a simple Gaussian function in section 5.3.1. Then it was calibrated again with a different empirical function in section 5.3.2. This was applied separately for all 66 runs and all 37 working pixels. In section 5.4.1 the time stability of the pixel calibration was investigated. The reason two different calibration methods were used, was to compare the more robust Gaussian fit to the more precise empirical model fit.

Finally, the stability of calibration over the pixels by staking the data over all working pixels is shown in section 5.4.2. All fits performed in this thesis were carried out with the python fitting package *lmfit*. The working principle of the developed fitting script is explained appendix A.2.

5.3.1 Calibration with Gaussian Functions

The first step in the analyzing process was the calibration with two simple Gaussian functions (equation 4.2). These were fitted over the $L - 32$ and the $M - 32$ lines to determine the peak positions. Using the calibrated and the determined peak values, the calibration was then performed using a linear function (see equation 4.7). The energy of the L line was set to (31.4515 ± 0.0004) keV, and the M line energy of (32.9339 ± 0.0005) keV. The source voltage of 1 kV was considered by adding it onto both lines. Both values are taken from [53] by calculation of the mean weighted by the intensities of the L_2 and L_3 line and of M_2 and M_3, respectively with equation 5.1.

The fitted Gaussian functions are shown in figure 5.7 for three pixels with different count rates. Pixel 28 lies on the same plane as the krypton source and has therefore a high count rate of 100 cps. The other two pixels used as examples, pixel 16 with a count rate of 86 cps and pixel 23 with a count rate of 55 cps do not lie at the exact plane of the source. The entire peaks of the spectrum cannot be described by a simple Gaussian, only the range narrow around the peak was taken as fit region, since here the effects of, for example, the diffusion part are small.

With both the peak positions obtained through the Gaussian fits, a linear function (see equation 4.7) could be fitted through these points (see figure 5.8). The found fit parameters are shown in table 5.1 for all three pixels.
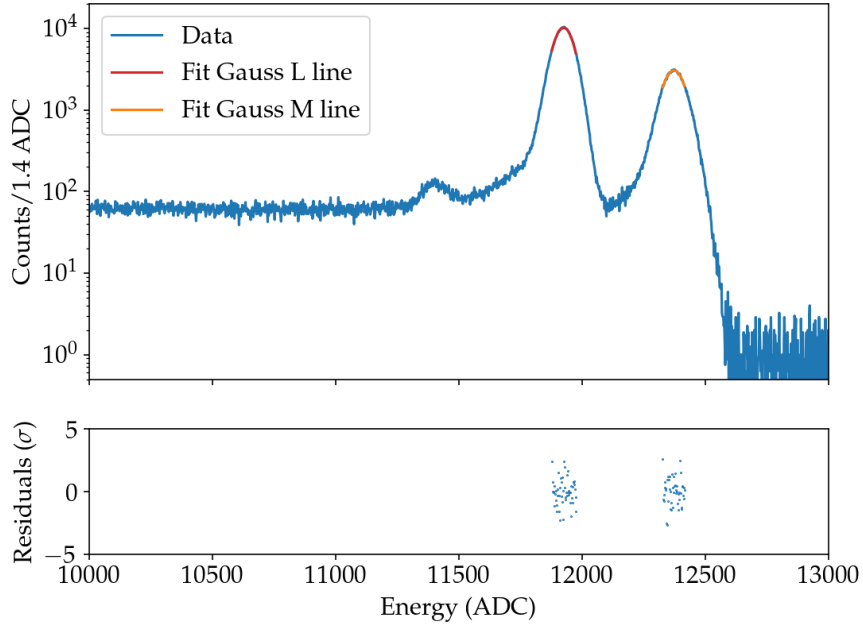
(a) Gaussian function fitted in the L-32 and M-32 lines of the energy spectrum for pixel 16.
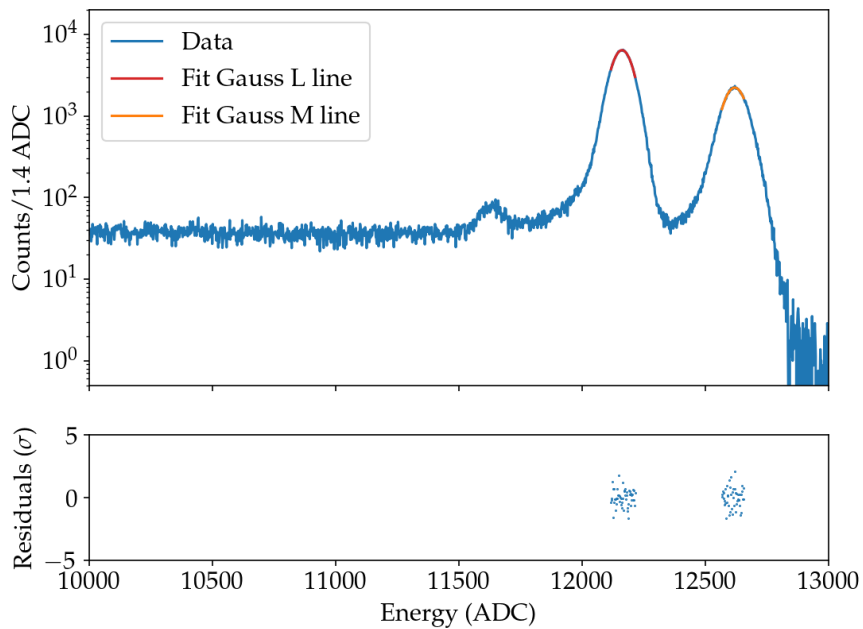
(b) Gaussian function fitted in the L-32 and M-32 lines of the energy spectrum for pixel 23.
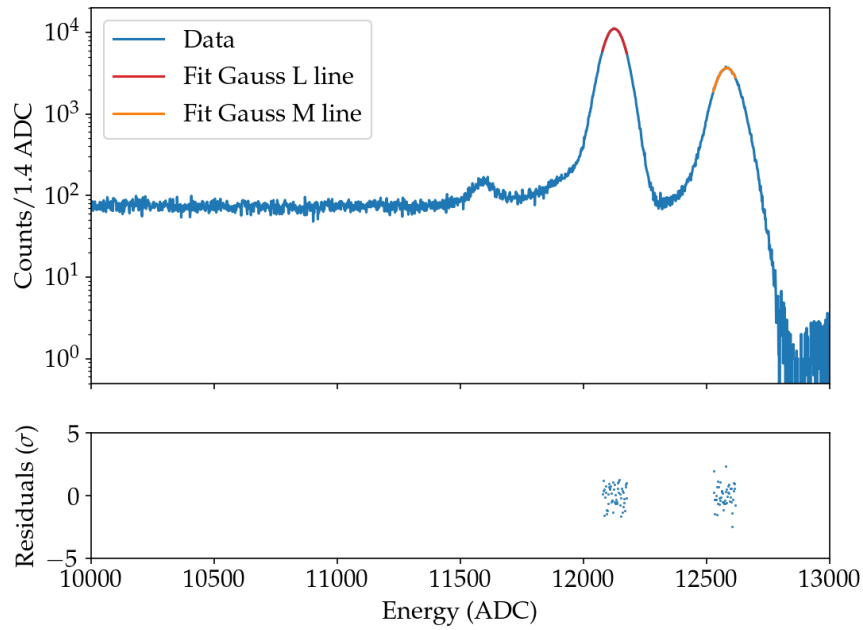
(c) Gaussian function fitted in the L-32 and M-32 lines of the energy spectrum for pixel 28.

Figure 5.7: Gaussian function fitted in the L-32 and M-32 lines of the energy spectrum for three pixels at different positions in the electron beam of the ^{83m}Kr source.

Table 5.1: Parameters of the linear fit function for pixels 16, 23 and 28.

Pixel	Slope (eV/ADC)	Offset (ADC)
16	3.30732584642309(3)	$-7.9853326492204(4)$
23	3.24348754434288(3)	$-7.9932475166632(4)$
28	3.24454707146101(3)	$-7.8872366051675(3)$

Since the calibration parameters are in a similar range, it could be concluded that the different pixels basically work similarly, but the differences are not negligible. The uncertainty of the parameters is so small because the theoretical values have only minor uncertainties and the linear fit through two points gives only a small uncertainty.
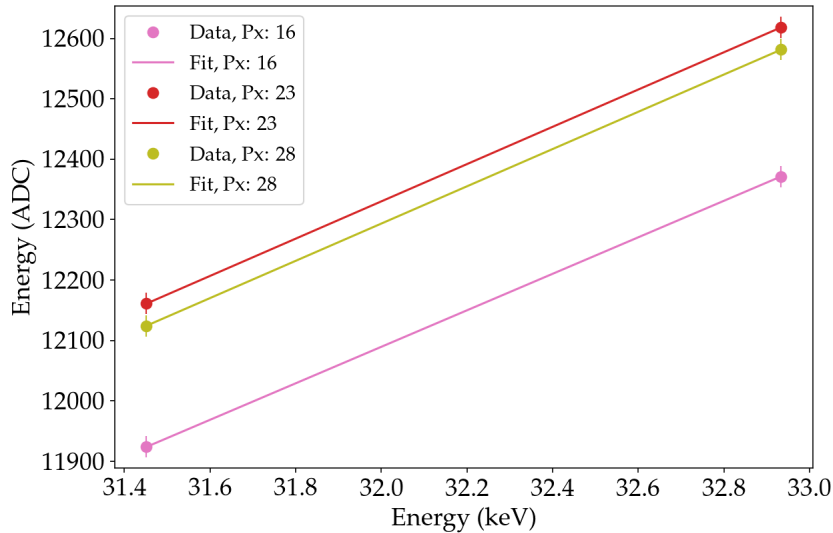
Figure 5.8: Linear Fit for three pixels. The peak positions of the L and M line were obtained with two Gaussian fits (see equation 4.2) in the energy spectrum.

With this slope and offset the spectra were then converted from ADC to keV, as shown in figure 5.9. Here are the measured spectra shown without binning in the area of the interesting features of the spectrum.

After calibrating all working pixels, the electron response could be investigated. Therefore, the empirical function (see section 5.3.2) was fitted into the calibrated energy spectrum. The result is shown in figure 5.10 until figure 5.12. Here the empirical model function of equation 5.6 was used. Overall, this fit agrees well with the data as shown in table 5.2.

Table 5.2: FWHM of the energy spectra of the three different pixels after calibration with Gaussian functions. The reduced χ^2 is also given. In this case, the β parameter of the M diffusion part was not constrained.

Pixel	FWHM (eV)	Red. χ^2
16	(329.2 ± 1.6)	1.1
23	(334.4 ± 1.7)	1.1
28	(330.2 ± 1.3)	1.1

The width β in equation 5.3 for the M line is significantly larger than it physically would be meaningful. This can be seen in the significantly greater width of the β
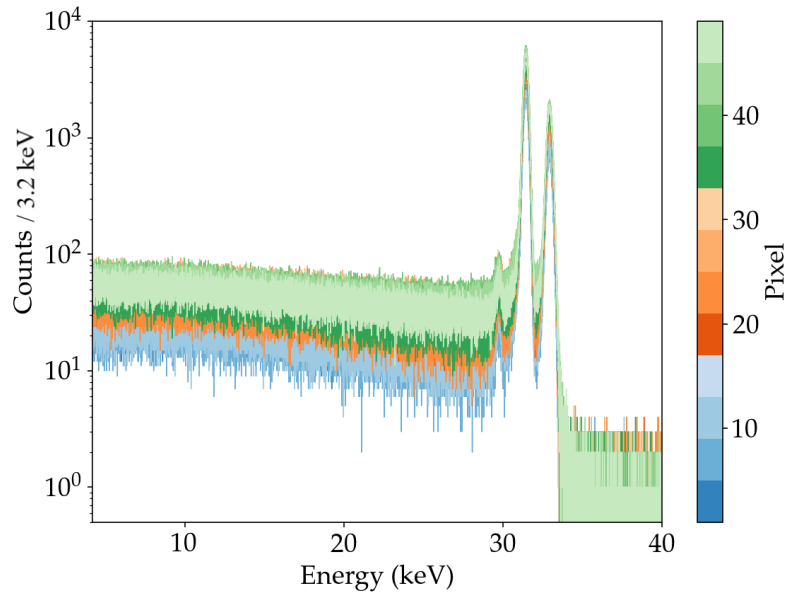
Figure 5.9: Calibrated energy spectra of all working pixels. Calibration was done with two simple Gaussian equations (see equation 4.2) for the L and the M line peak and a linear function (see equation 4.7) to convert the ADC values to keV. As expected all peaks are at the same x-position.

compared to the β of the L line diffusion part which should have a similar value. To match the values the β parameter was constrained. For a smaller β value, the reduced χ^2 and the value of the FWHM increase. These values show that the theory function agrees worse with the data, which could be due to the simplified calibration with the Gaussian functions. Examples for the three different pixels can be found in figure 5.10b, figure 5.11b and figure 5.12b. The obtained FWHM and reduced χ^2 from the fit are shown in table 5.3. Both values worsen with this constrained parameter.
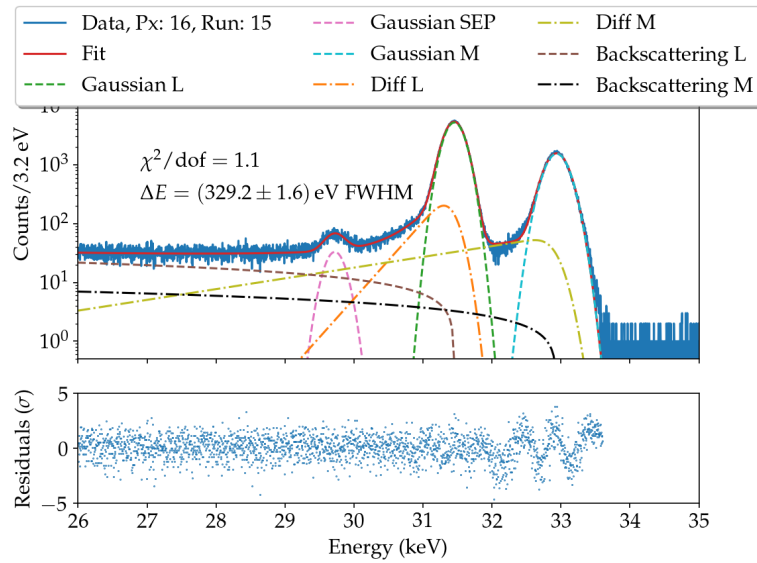
(a) Despite the small reduced $\chi^2 = 1.1$ and FWHM of (329.2 ± 1.6) eV, the width β of the diffusion part of the M line is different to the β term of the L line. One would expect similar values for both lines.
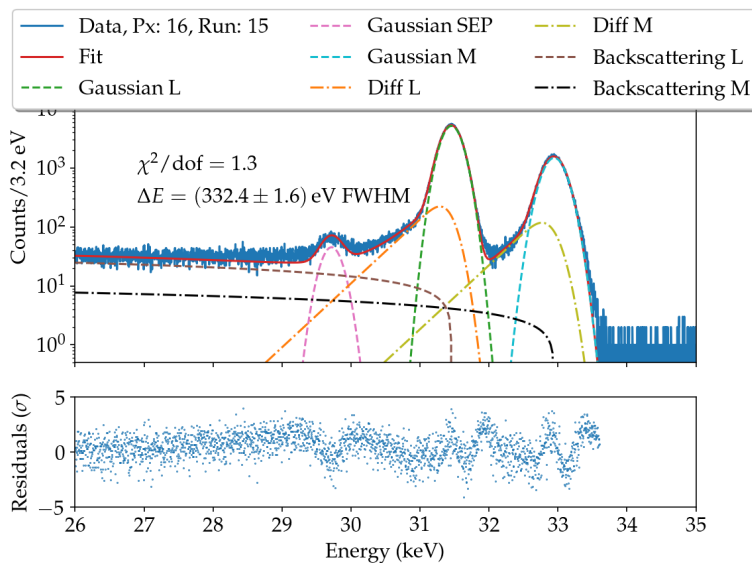
(b) A smaller width of β of the M line diffusion part, worsens the reduced $\chi^2 = 1.3$ and also the FWHM to (332.4 ± 1.6) eV.

Figure 5.10: Energy spectrum of pixel 16 with fitted empirical model function (see equation 5.6) after calibration with two simple Gaussian functions. Two different fit possibilities are shown. In a) plot there was no restriction of the fit parameter β of the M line diffusion term, while b), β of the M line diffusion term got the same limits as β from the L line diffusion part. The single parts are plotted for clarification. Run 15 means the one hour data taken after measuring 14 times one hour.
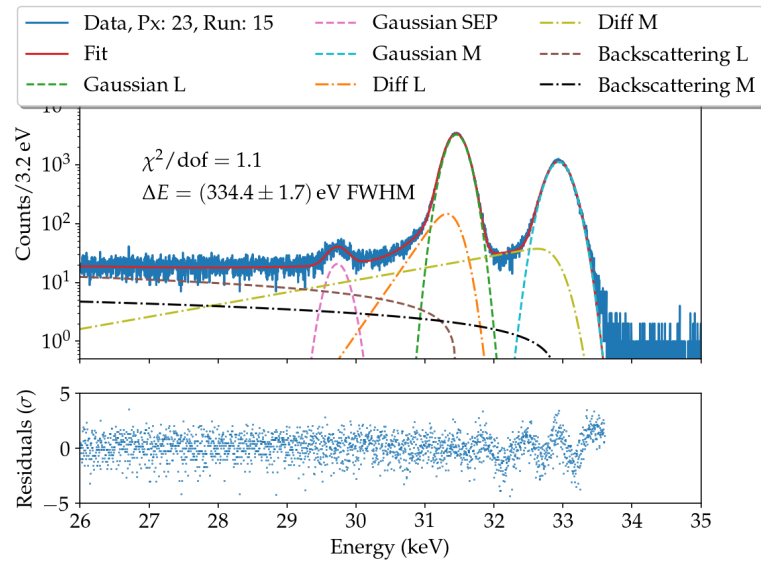
(a) Despite the small reduced $\chi^2 = 1.1$ and FWHM of (334.4 ± 1.7) eV, the width β of the diffusion part of the M line is different to the β term of the L line. One would expect similar values for both lines.
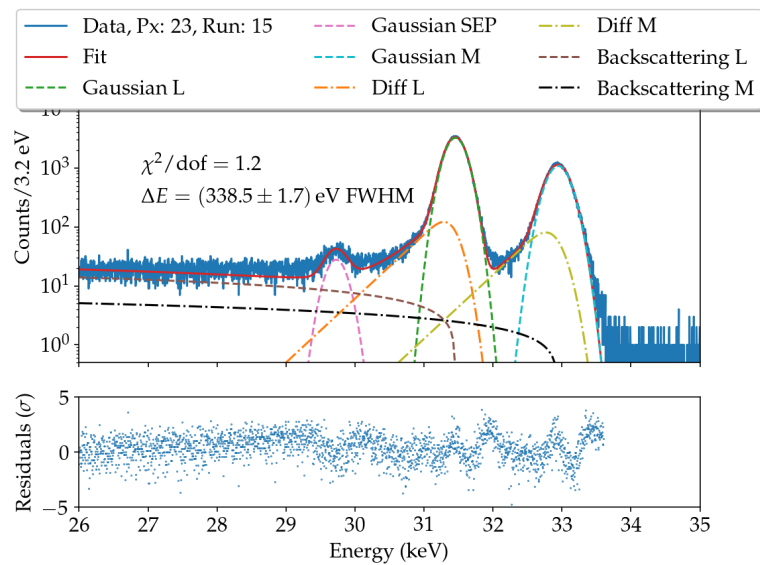
(b) A smaller width of β of the M line diffusion part, worsens the reduced $\chi^2 = 1.2$ and also the FWHM to (338.5 ± 1.7) eV.

Figure 5.11: Energy spectrum of pixel 23 with fitted empirical model function (see equation 5.6) after calibration with two simple Gaussian functions. Two different fit possibilities are shown. In a) plot there was no restriction of the fit parameter β of the M line diffusion term, while b), β of the M line diffusion term got the same limits as β from the L line diffusion part. The single parts are plotted for clarification. Run 15 means the one hour data taken after measuring 14 times one hour.
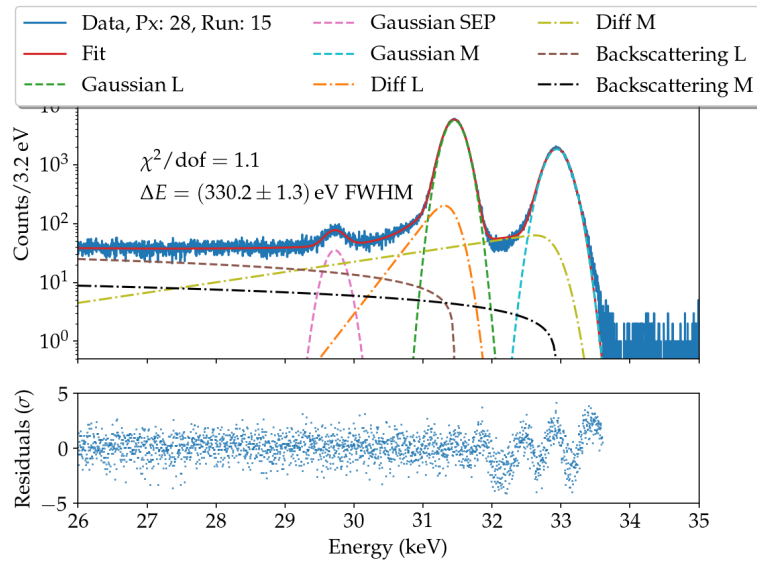
(a) Despite the small reduced $\chi^2 = 1.1$ and FWHM of (330.2 ± 1.3) eV, the width β of the diffusion part of the M line is different to the β term of the L line. One would expect similar values for both lines.
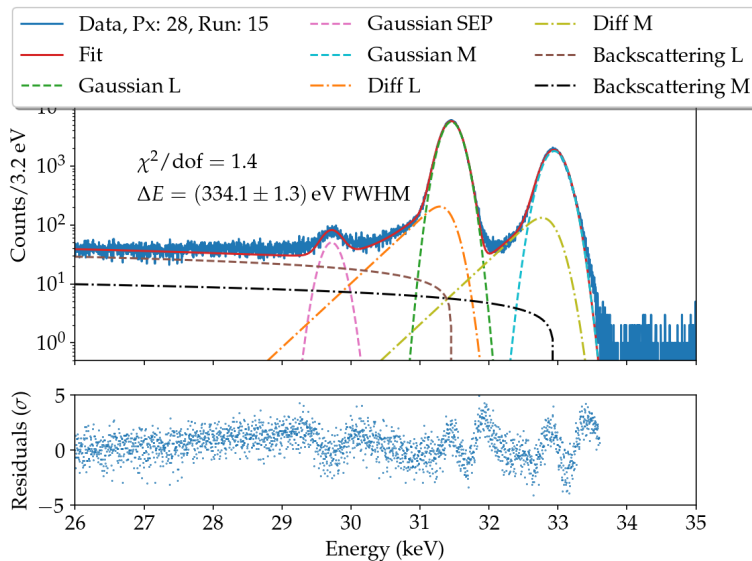
(b) A smaller width of β of the M line diffusion part, worsens the reduced $\chi^2 = 1.4$ and also the FWHM to (334.1 ± 1.3) eV.

Figure 5.12: Energy spectrum of pixel 28 with fitted empirical model function (see equation 5.6) after calibration with two simple Gaussian functions. Two different fit possibilities are shown. In a) plot there was no restriction of the fit parameter β of the M line diffusion term, while b), β of the M line diffusion term got the same limits as β from the L line diffusion part. The single parts are plotted for clarification. The single parts are also plotted for clarification. Run 15 means the one hour data taken after measuring 14 times one hour.

Table 5.3: FWHM of the energy spectra of the three different pixels after calibration with the Gaussian functions. The reduced χ^2 is also given. The β parameter of the M diffusion part was constrained to match the value of the β parameter of the L diffusion part.

Pixel	FWHM (eV)	Red. χ^2
16	(332.4 ± 1.6)	1.3
23	(338.5 ± 1.7)	1.2
28	(334.1 ± 1.3)	1.4

Pixel maps with the FWHM obtained with each fit are shown in figures 5.13 and 5.14. Both pixel maps are color-indexed. For both fits, the FWHM is distributed over a narrow range between 324 eV and 348 eV or 328 eV and 350 eV, respectively. The mean value of the FWHM of (335.5 ± 0.3) eV is overall smaller for the fit without limitation of the β parameter in the equation of the M line Diffusion part 5.3. The mean value of the worse FWHM is (338.8 ± 0.3) eV.
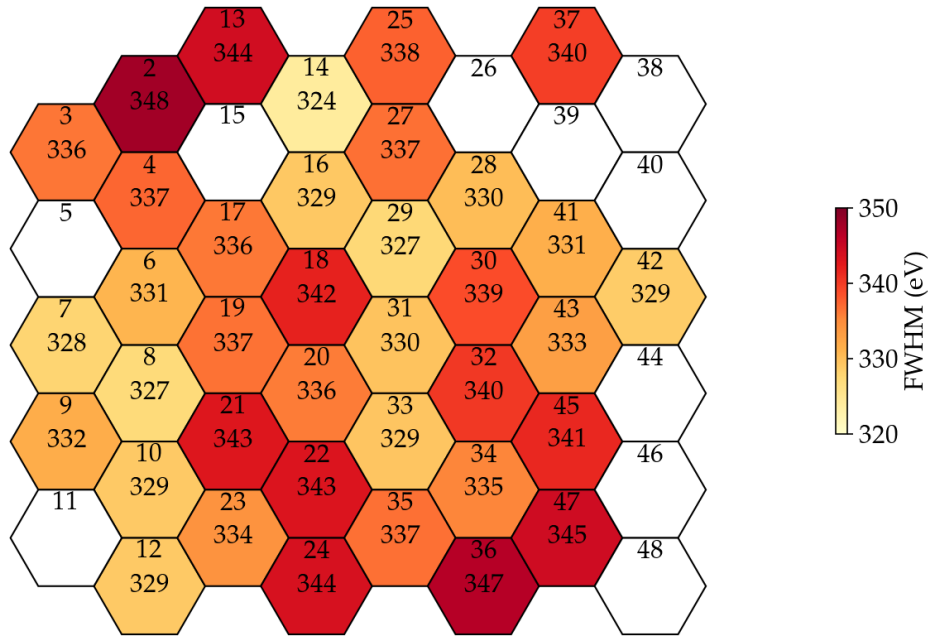
Figure 5.13: Color-indexed pixel map of the FWHM obtained with the empirical model fit (see equation 5.6) without constraining the β parameter of the M line Diffusion part (see equation 5.3) after calibration with the Gaussian functions.
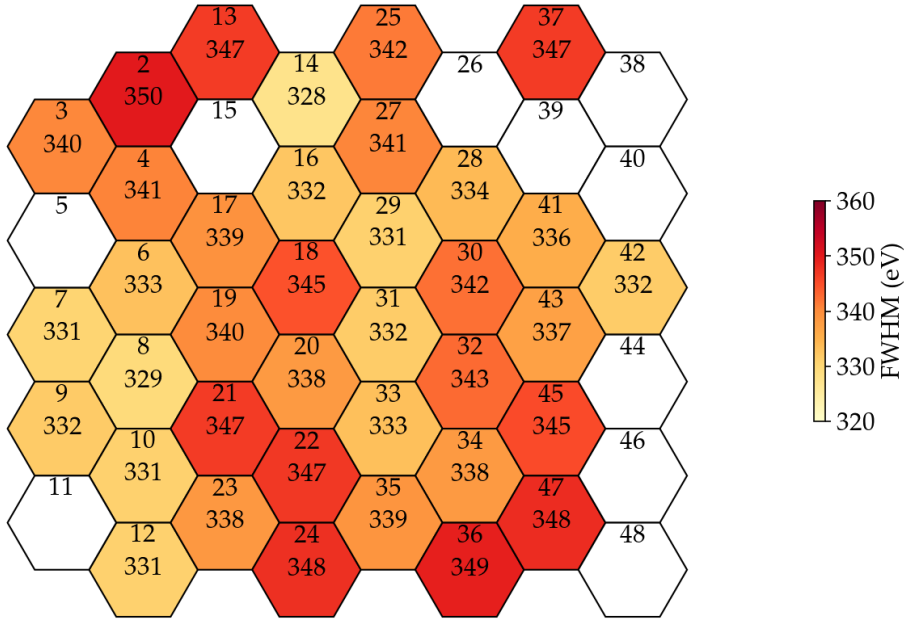
Figure 5.14: Color-indexed pixel map of the FWHM obtained with the empirical model fit (see equation 5.6) with constraining the β parameter of the M line Diffusion part (see equation 5.3) after calibration with the Gaussian functions. The values of the FWHM are overall a few eV higher than the values obtained with the constrained fit.

5.3.2 Calibration with Empirical Model Function

To describe the mono-energetic electrons originating from wall electrons or a ^{83m}Kr source, a special empirical model function is constructed, which is introduced first and then used for calibration and characterization in the following. It is fitted in the energy spectra and is adjustable to different spectral changes of the detector response. For example, different incident energies can be described. It takes four main characteristics into account.

The first characteristic is the main peak in the energy spectrum. Most of the electrons deposit almost their entire energy in the sensitive volume of the detector [56]. Its shape can be approximated as a Gaussian function, see equation 5.2.

$$I_G(E) = A_G \cdot \exp\left(-\frac{(E - E_0)^2}{2\sigma^2}\right) \tag{5.2}$$

Here A_G is the amplitude, E_0 is the mean, and σ, the width of the Gaussian, considers the noise and statistical fluctuations in the production of secondary electrons.

Without effects caused by the entrance window, this part would represent the electrons that deposited their entire energy in the detector [35].

The second characteristic is the low-energy tail. It is an asymmetry of the main peak and shows as a low-energy shoulder. Undetected energy depositions due to an incomplete charge collection at the entrance window cause this tail. Inside this layer, deposited charges can not be detected, and electrical fields inside the silicon volume close to this layer are too weak to transport the charge carriers to the read out contact efficiently. The low-energy tail is also called the diffusion part (see equation 5.3) and is described by a step function, especially an error function and exponential tail of low energies with A_D, the amplitude, and β, the steepness of the function [56].

$$I_D(E) = A_D \cdot \exp\left(\frac{E - E_0}{\beta}\right)\left(1 - \text{erf}\left[\frac{E - E_0}{\sqrt{2\sigma^2}} + \frac{\sigma}{\sqrt{2}\beta}\right]\right) \tag{5.3}$$

For lower energies or thicker entrance windows, often a second diffusion part I_{D2} is needed for a better agreement between model and data [35].

The following characteristic is the silicon escape peak (SEP). It is described by the Gaussian function 5.4 and is a scaled projection of the main peak.

$$I_{esc}(E) = A_{esc} \cdot \exp\left(-\frac{(E - [E_0 - \Delta E_{esc}])^2}{2\sigma^2}\right) \tag{5.4}$$

A_{esc} is the amplitude and ΔE_{esc} is a shift towards lower energies. It should be noted here that σ and E_0 of the diffusion part and the SEP are the same as those of the Gaussian. The energy shift is caused by incoming radiation, ionizing the silicon atoms in the detector material mostly from the K shell. When the silicon atom de-excites over a K_α transition, an x-ray is emitted with $\Delta E_{esc} = 1.74\,\text{keV}$ [56]. This x-ray photon can leave the detector undetected. The silicon escape peak occurs not only for the $L - 32$ line, but also for the $M - 32$ line. This peak is not visible in the energy spectrum because it is located inside the main peak of the $L - 32$ line [35]. The last main characteristic is the backscattering tail. It is described via equation 5.5 and consists of primary and secondary electrons which scattered back of the detector surface or left the detector.

$$I_B(E) = A_B \cdot \left(\frac{E}{E_0 - a}\right)^b \cdot \left(1 - \frac{E}{E_0}\right)^c \tag{5.5}$$

Thereby, they are not fully depositing their energy. The parameter b describes the shape around the threshold a which is set slightly above the noise in the low energy range. At higher energies c describes the shape of the energy spectrum. Here, the electrons deposit most of their energy in the detector and leave with the remaining energy [35]. Backscattering probability is about 20% for 20 keV electrons at vertical

incidence. This probability increases for larger incident angles [56]. The incoming electrons scatter most likely on the detector surface. When entering the detector, the probability of scattering decreases for larger penetration. A_B is the amplitude of the function. A fifth characteristic neglected in the further analysis is the pileup shoulder. It comes from a relatively large periodic noise during the measurement. As a comparison to the Gaussian calibration, a calibration using the special empirical model function was used. The model consisted of the four different characteristics explained above. It considers the Gaussian parts (equation 5.2) of the L and M lines, the backscattering parts of both lines (equation 5.5), and a Gaussian part (equation 5.4) for the SEP. Furthermore, the Diffusion parts (equation 5.3) for the L and M lines, respectively, were included. The general empirical model function used for the calibration is given in equation 5.6

$$
\begin{aligned}
I_{\text{total}}(E) = {} & I_{G_{\text{L line}}}(E) + I_{D1_{\text{L line}}}(E) + I_{B_{\text{L line}}}(E) + I_{\text{esc}}(E) + \\
& I_{G_{\text{M line}}}(E) + I_{D1_{\text{M line}}}(E) + I_{B_{\text{M line}}}(E)
\end{aligned}
\tag{5.6}
$$

This function was fitted in the energy spectrum of the same pixels used for the Gaussian calibration (see section 5.3.1). This can be seen in figure 5.14.
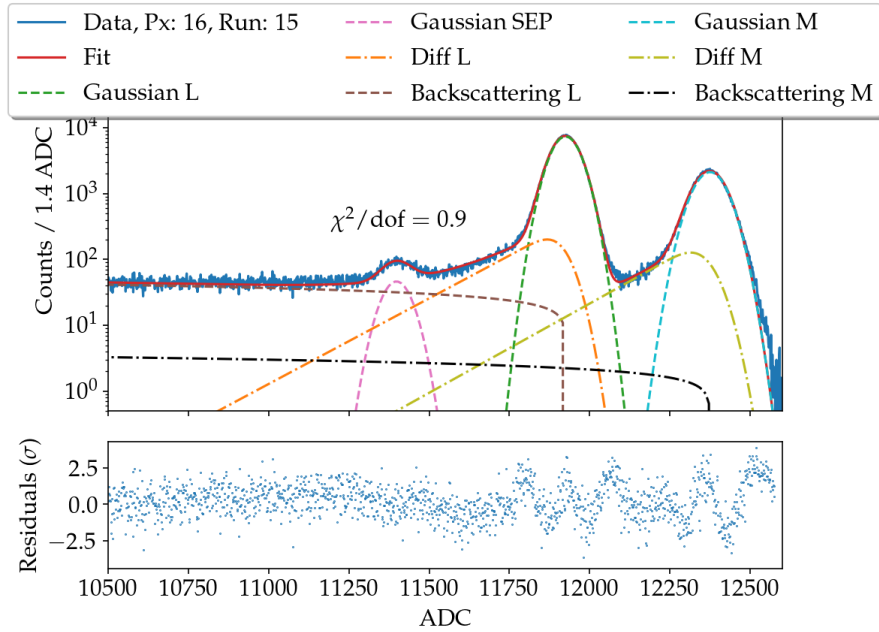
(a) Calibration fit for pixel 16. A small reduced χ^2 of 0.9 was determined.
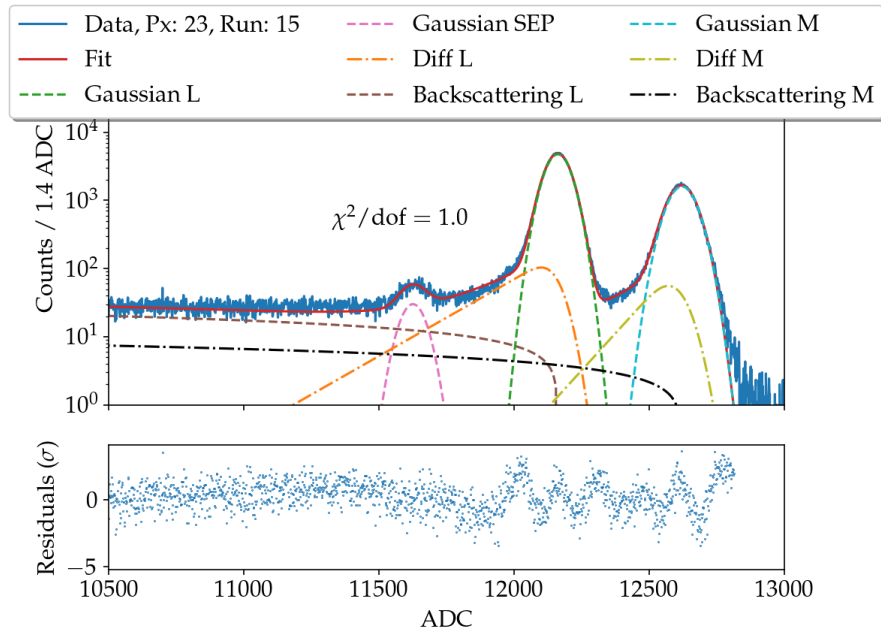
(b) Calibration fit for pixel 23. A small reduced χ^2 of 1.0 was determined.
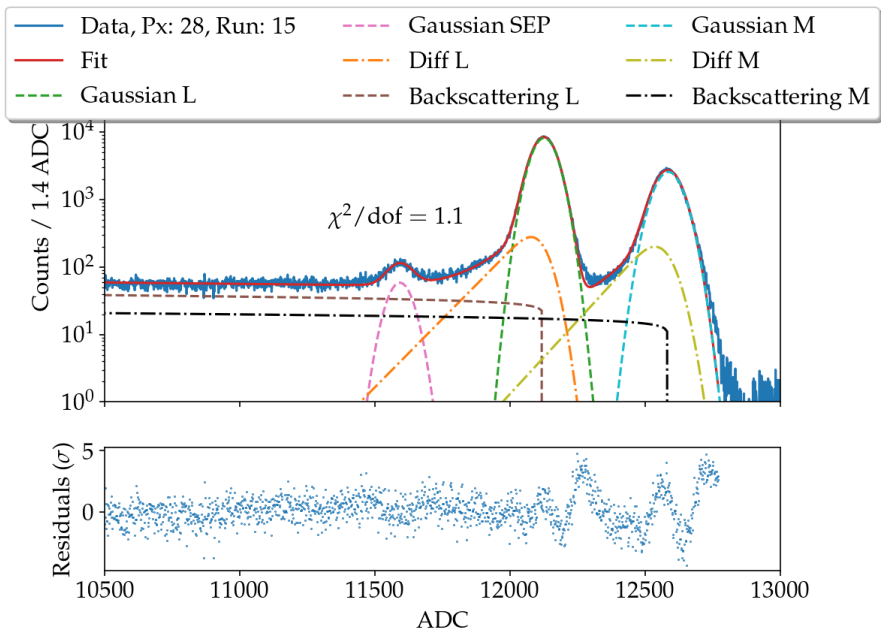
(c) Calibration fit for pixel 28. A small reduced χ^2 of 1.1 was determined.

Figure 5.14: Calibration fit in the energy spectrum obtained with three different pixels at different position in the electron beam coming from the ^{83m}Kr. Pixels 16 and 23 are located slightly outside the beam plane, while pixel 28 is located directly inside the beam plane.

From this fitted empirical function, the peaks of the $L - 32$ and $M - 32$ line were again used to calibrate the energy spectrum. The linear fit, following equation 4.7 is shown in figure 5.15 for all three pixels. The fitting parameters of the linear fit are presented in table 5.4. The values are different from the calibration parameters for the Gaussian calibration (see table 5.1) and therefore affect the further analysis. This becomes clearer when stacking the runs in section 5.4.1.
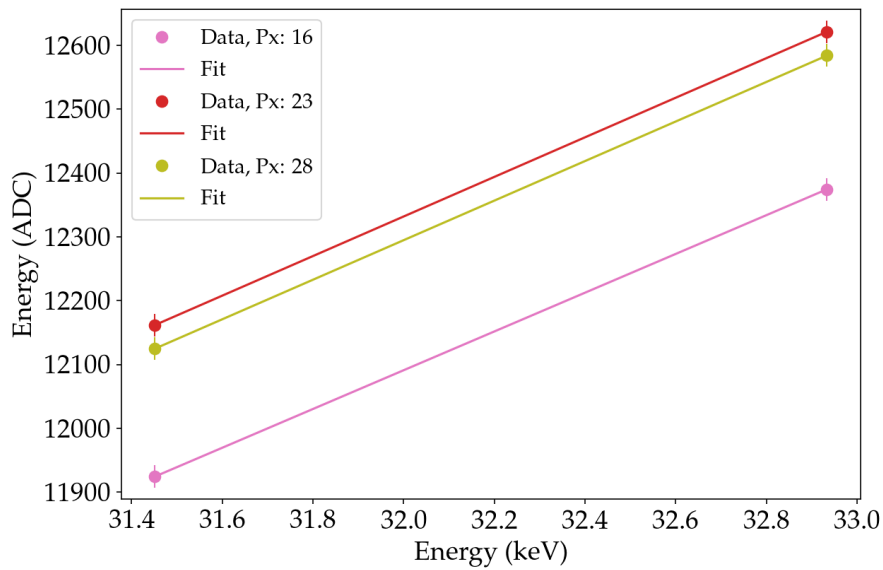
Figure 5.15: Linear fit through the peak positions of the $L - 32$ and $M - 32$ lines of ^{83m}Kr. Three different pixels are shown. The peak positions were obtained by calibration with an empirical model function (see equation 5.6).

Table 5.4: Parameters of the linear fit function for pixels 16, 23 and 28 after calibration with an empirical model function.

Pixel	Slope (eV/ADC)	Offset (ADC)
16	$3.28266673298947(3)$	$-7.6926499902561(3)$
23	$3.240020966357(2)$	$-7.955724651047(3)$
28	$3.24221646476994(3)$	$-7.8589789460469(3)$

Then the empirical function was again fitted in the energy spectrum. This was done again because of interest in the characteristic quantities of the spectrum, such

as the FWHM and direct conversion of the first fit involves a higher uncertainty than a second fit with the calibrated data. In addition, due to the low statistics, it was again unnecessary to include a second diffusion term for both the L and M line, so only one was used for each peak. The fully used empirical model function is shown in equation 5.6.

The fit performed to investigate the detector response can be found in figure 5.16.
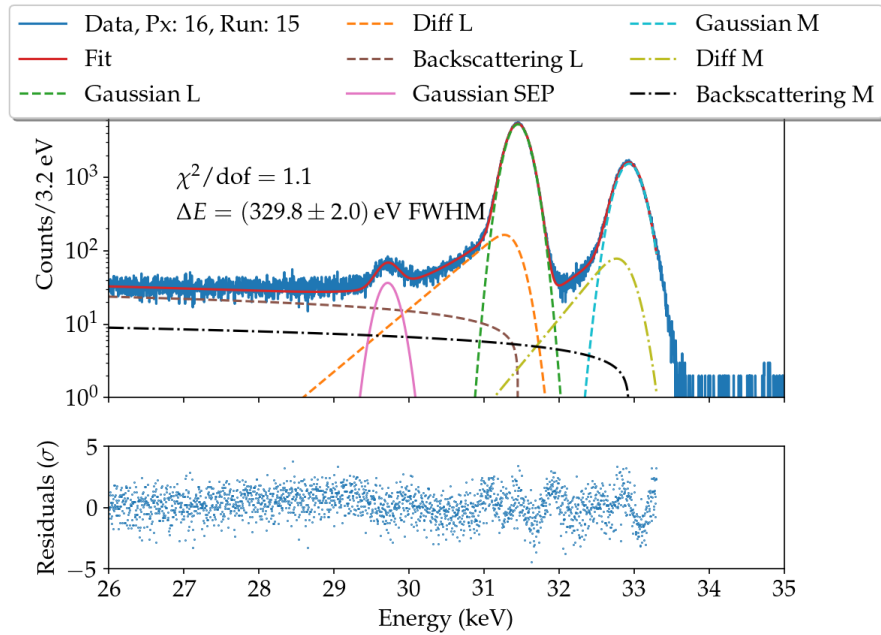
(a) Calibrated energy spectrum for pixel 16. A small reduced $\chi^2 = 1.1$ and a FWHM of (329.8 ± 2.0) eV are obtained.
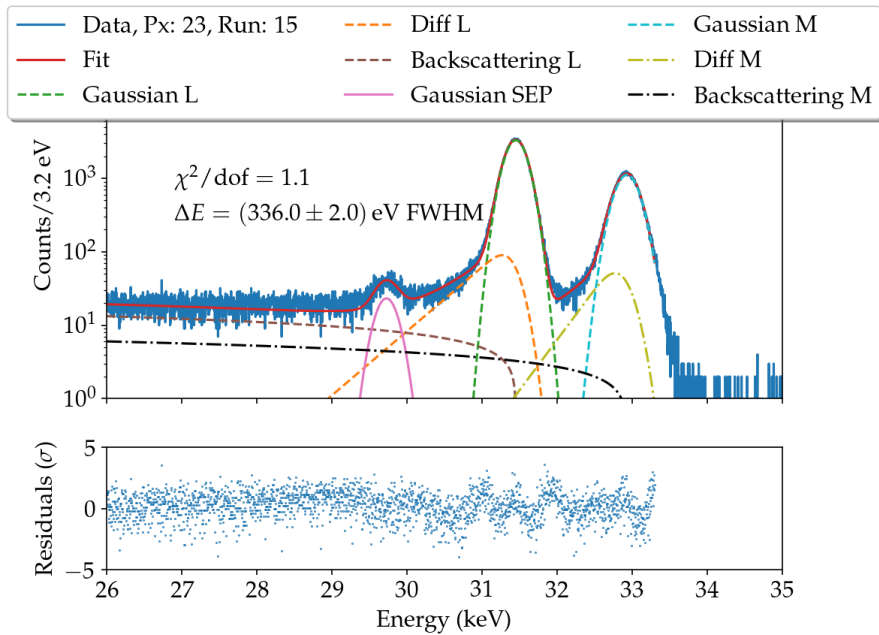
(b) Calibrated energy spectrum for pixel 23. A small reduced $\chi^2 = 1.1$ and a FWHM of (336.0 ± 2.0) eV are obtained.
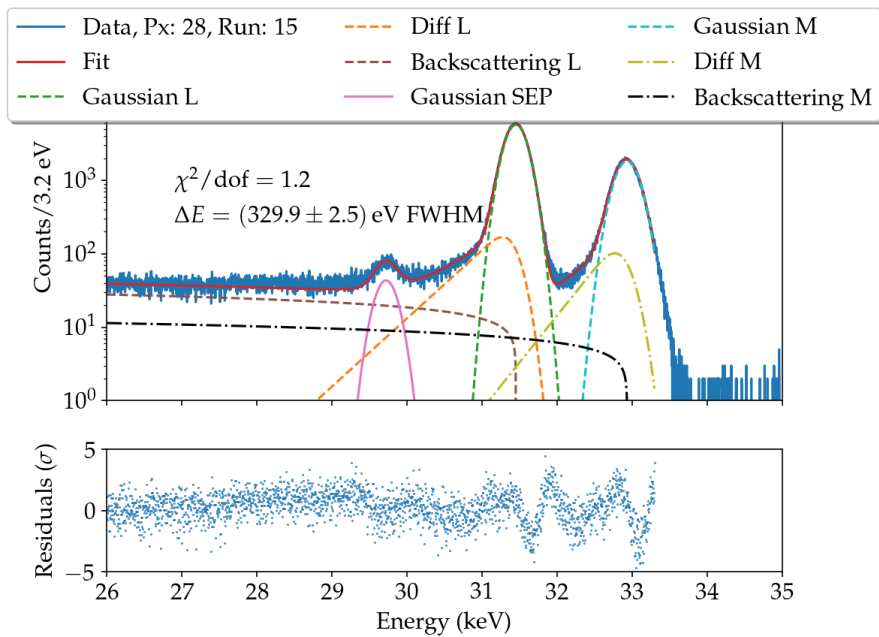
(c) Calibrated energy spectrum for pixel 28. A small reduced $\chi^2 = 1.2$ and a FWHM of (329.9 ± 2.5) eV are obtained.

Figure 5.16: Energy spectra of three different pixels after calibration with an empirical model function. This model function (see equation 5.6) is again fitted into the spectra and the single parts of the function are also plotted.

A color-indexed pixel map (see figure 5.17), shows the obtained FWHMs for all working pixels. With a mean value of (337.0 ± 0.4) eV it lies between the two mean values of the FWHM obtained with the Gaussian calibration, (335.5 ± 0.3) eV and (338.8 ± 0.3)eV.
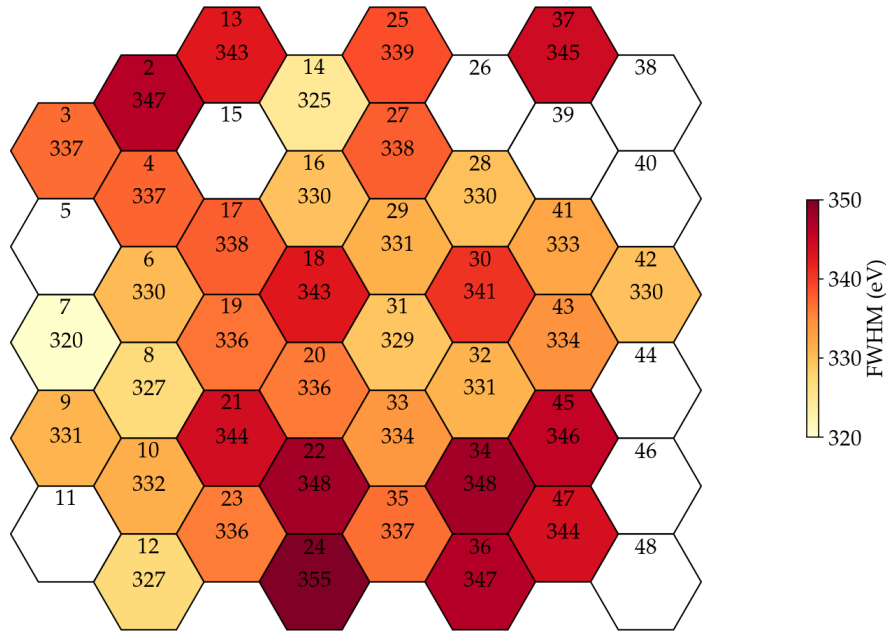
Figure 5.17: Color-indexed pixel map of the FWHM obtained with the empirical model fit (see equation 5.6).

5.3.3 Conclusion

Comparing both calibrated energy spectra with the fitted empirical model function shows an agreement of the FWHM values. The FWHMs over all working pixels for the three different calibrations is shown in figure 5.18.
Although they also have small reduced χ^2, the single fits show deviations. This becomes most clear for the diffusion term of the M line. A disadvantage of calibration with the empirical function is the longer computing time and the lower robustness. Nevertheless, the calibration with the empirical model function is more suitable for a meaningful analysis. This becomes especially relevant when stacking runs or

pixels are considered, which can also partially deform the spectrum, making a pure description with Gaussian functions insufficient.
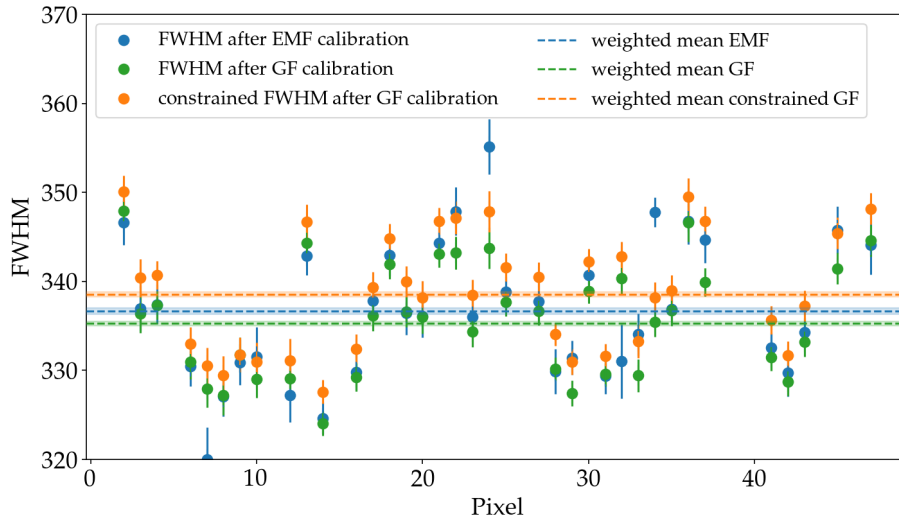
Figure 5.18: FWHMs for the different working pixels. Three calibrations are shown. EMF stands for the calibration with the empirical model function, GF stands for the calibration with the Gaussian functions. The constrained parameter in the second GF calibration, was the β parameter of the M line diffusion term.

5.4 Data Combination and Analysis

5.4.1 Stacking of Runs

After calibrating and fitting all individual pixels and runs, the time stability of the calibration was investigated. At first, the Gaussian calibrated spectra were used, then the one calibrated with the empirical model function. The calibration from the first run was determined and applied to the subsequent runs.

Calibration with Gaussian functions

To investigate the time stability, the peak positions of the $L - 32$ and $M - 32$ lines were plotted over the time as shown in figure 5.19 for pixel 14, a representative for all working pixels.
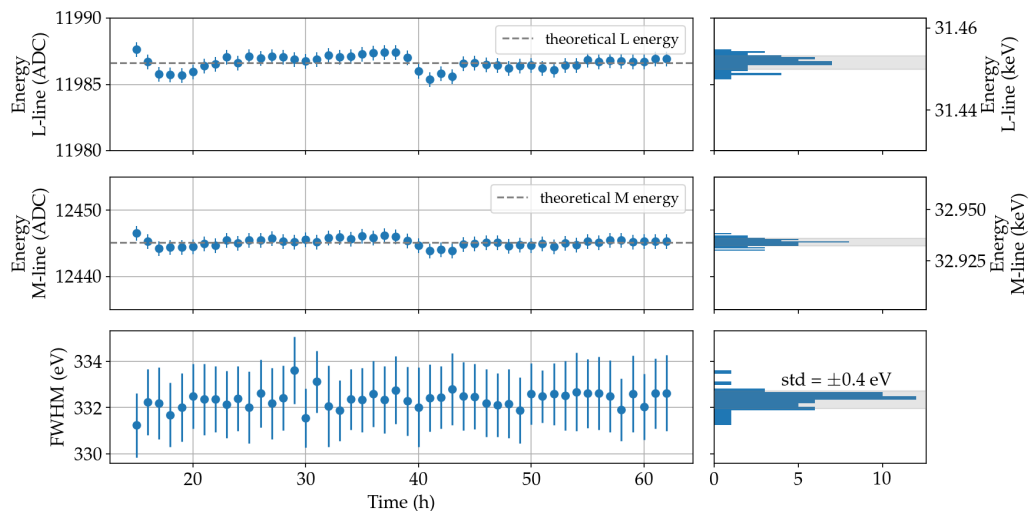
Figure 5.19: Time stability investigation plot of the calibration. Pixel 14 is representative of all working pixels. The two upper plots show the peak position of the $L - 32$ and $M - 32$ line, respectively, in energy (left: ADC, right: keV) over time (h). The mean peak positions in keV were calculated with the mean of the calibration parameters and the theoretical peak positions for both lines calculated in section 5.2. The bottom plot shows the FWHM in eV over time (h). The weighted mean was (332.1 ± 0.3) eV. Overall the deviation of the peak positions of the $L - 32$ and $M - 32$ line from the value obtained with the mean of the calibration parameters is less than 5 eV in both cases. This is a small value in comparison to the FWHM. Also looking at the histogram on the right shows that the values are approximately Gauss distributed.

Here, in the upper plot, the left axis indicates the peak position of the $L - 32$ line represented by the energy in ADC. On the right axis, the peak position of the $L - 32$ line represented by the energy in keV is displayed calulated with the mean of the calibration parameters. A theoretical $L - 32$ line energy of (31.4515 ± 0.0004) keV as calculated in section 5.2 was converted with the calibration parameters from keV to ADC. The same applies to the middle plot, except the peak position of the $M - 32$ line was used. Here, the theory line was set to (32.9339 ± 0.0005) keV, also calculated in section 5.2. The bottom plot shows the FWHM over time with the weighted mean. The statistical uncertainties obtained by the fit were also plotted for all data points. On the right the histograms of each plot are shown.

The maximum deviation of both transition lines from their calculated values is less than 5 eV. This deviation is negligible compared to the mean energy resolution of (332.1 ± 0.3) eV. Also the histogram was approximately Gauss distributed, and therefore, it was concluded that stacking of the runs is reasonable. Hence, it was performed for further investigations.
To illustrate the effects of the $M - 32$ line backscattering part, a reduced version of the empirical function was first fitted into the energy spectrum. The used empirical function is composed of the Gaussian function (equation 5.2) for the $L - 32$ line and the related Diffusion function (equation 5.3). Furthermore a Gaussian function for the silicon escape peak (equation 5.2) and the backscattering function (equation 5.5) for the $L - 32$ line were used. The entire used empirical function is shown in equation 5.7.

$$I_{\text{SimplifiedEF}}(E) = I_{G_{\text{L line}}}(E) + I_{D1_{\text{L line}}}(E) + I_{B_{\text{L line}}}(E) + I_{\text{esc}}(E) \qquad (5.7)$$

As can be seen in figure 5.20, this empirical model function fitted in the energy spectrum leads to a structure in the residuals of the backscattering part.
There could be three reasons for this. One is the neglect of the $M - 32$ line. This line also consists of a backscattering part, contributing to the overall backscattering tail. Also, the high statistics could cause that the model is insufficient. This gets even clearer when looking at the strong structure in the residuals of the diffusion part in figure 5.20. The last reason could be the calibration with the Gaussian function.
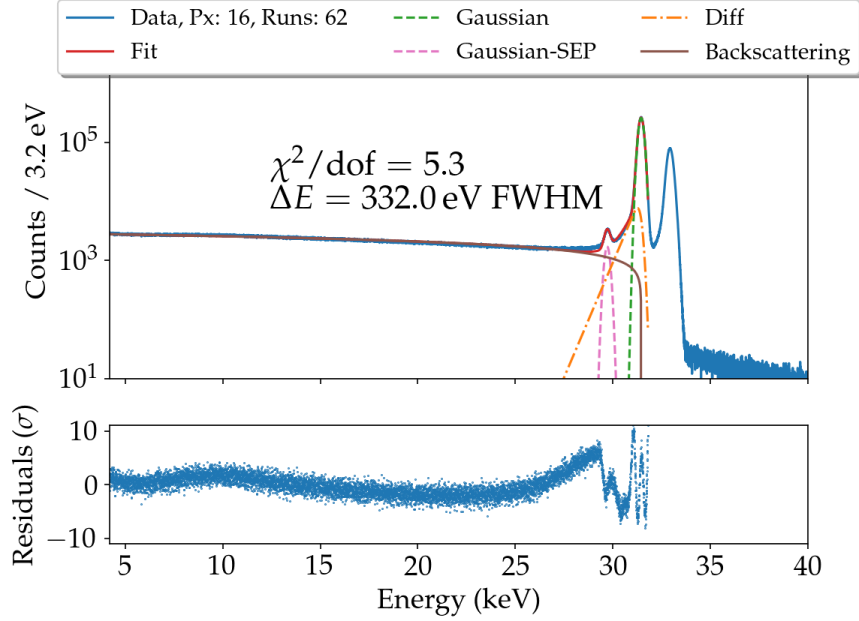
Figure 5.20: Simplified empirical model function (see equation 5.7) fitted into the Gaussian calibrated energy spectrum of pixel 16. The taken data was stacked over the runs. For the fit only Gaussian functions for the $L - 32$ line and the silicon escape peak, and a Diffusion and Backscattering function for the $L - 32$ line were used. A structure in the residuals of the backscattering part and the one in residuals of the diffusion part indicate a missing part in the empirical model function. This is shown in the bottom plot of the figure. The single parts of the empirical function are plotted in the energy spectrum.

To investigate the entire $L - 32$ and $M - 32$ line spectrum, the empirical model function was used to describe all parts. Therefore the equation 5.8 consisted of two backscattering parts, two Gaussian parts and two Diffusion parts for both the $L - 32$ and $M - 32$ lines and also a Gaussian part for the silicon escape peak.

$$
\begin{aligned}
I_{\text{total}}(E) = \ & I_{G_{\text{L line}}}(E) + I_{D1_{\text{L line}}}(E) + I_{D2_{\text{L line}}}(E) + I_{B_{\text{L line}}}(E) + I_{\text{esc}}(E) + \\
& I_{G_{\text{M line}}}(E) + I_{D1_{\text{M line}}}(E) + I_{D2_{\text{M line}}}(E) + I_{B_{\text{M line}}}(E)
\end{aligned}
\tag{5.8}
$$

In figure 5.21, this fitted empirical function is shown for the three different pixels at different positions on the detector.
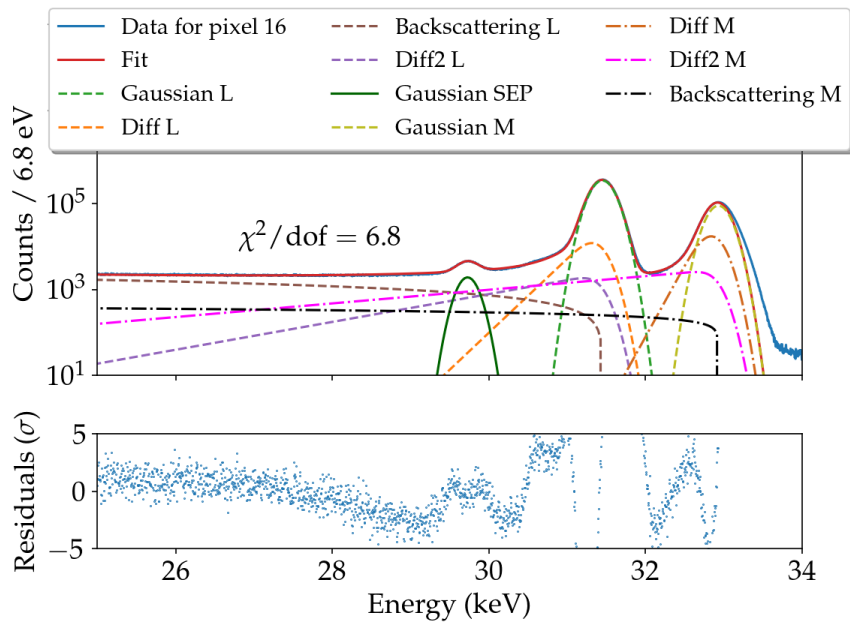
(a) Gaussian calibrated energy spectrum of pixel 16 with fitted empirical function. The data was stacked over the runs.
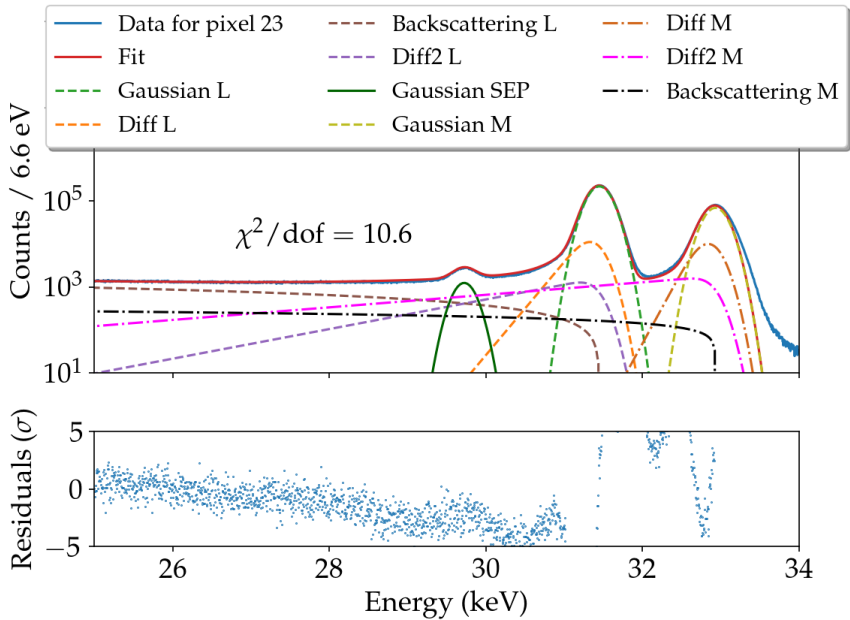
(b) Gaussian calibrated energy spectrum of pixel 23 with fitted empirical function. The data was stacked over the runs.
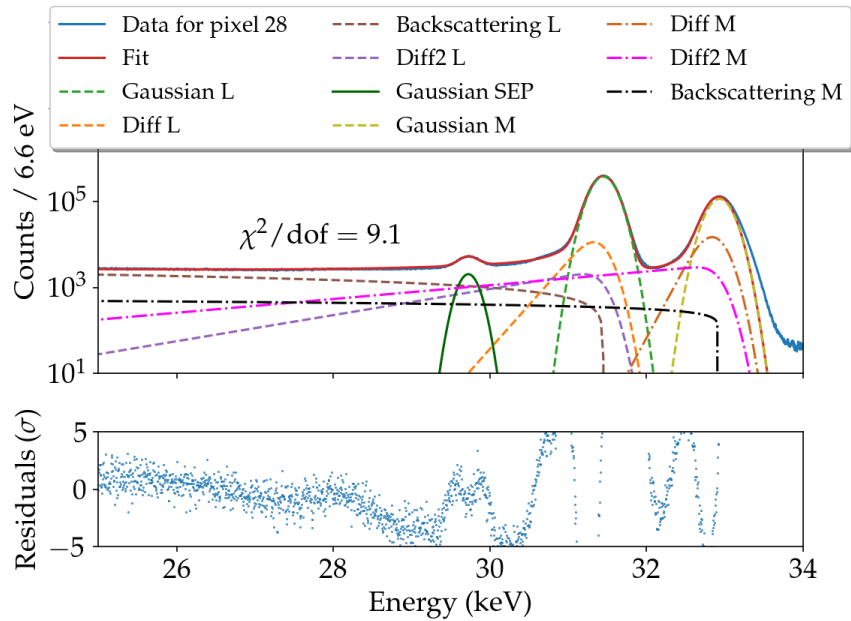
(c) Gaussian calibrated energy spectrum of pixel 28 with fitted empirical function. The data was stacked over the runs.

Figure 5.21: Empirical model function (see equation 5.6) fitted in Gaussian calibrated energy spectra of three different pixels. The single parts of the empirical model are plotted in the energy spectrum and the residuals are shown in the bottom plots.

Also the single parts of the entire function are plotted. In the lower plots, it can be seen, that the residuals still show a slight structure. Therefore it can be concluded, that the omission of the $M - 32$ line was not the main reason causing this structure in the first place. The reduced χ^2 of 6.8 for pixel 16, 10.6 for pixel 23 and 9.1 for pixel 28 are relatively high compared to the ones before stacking the runs. This also points out that the statistics could resolve structures not sufficiently described by the model function.

A pixel map with the energy resolution after stacking all runs is shown in figure 5.22. Equally to the FWHM of the single runs (see figure 5.14), the values are in the range 320 eV and 360 eV. A mean value of (336.36 ± 0.07) eV is obtained for the energy resolution when calibration with two Gaussian functions and stacking the runs. Comparing this value to the FWHMs obtained by the Gaussian calibrated energy spectra for the single runs shows only a slight deviation (see table 5.5).
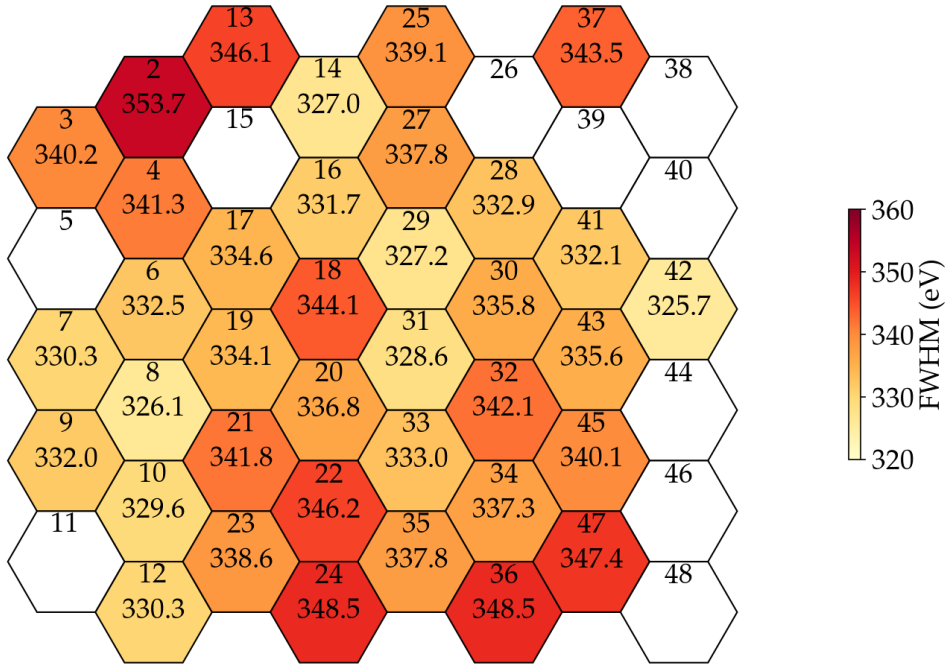
Figure 5.22: Color-indexed pixel map of the FWHM obtained after stacking all runs and calibrating the energy spectra with two Gaussian functions. The values of the FWHM are in the same range as the ones before stacking the runs, between 320 eV and 360 eV (see figure 5.14). The mean value of the energy resolution after stacking the runs is (336.36 ± 0.07) eV FWHM.

Table 5.5: Mean FWHM values and reduced χ^2 of unstacked energy spectrum for both calibration methods, Gaussian function (GF) and empirical model function (EMF). Also the mean FWHM value and the reduced χ^2 of the energy spectrum with stacked runs and calibration with the Gaussian functions are shown. The values are given for pixel 28.

	GF FWHM (eV)	EMF FWHM (eV)	GF red. χ^2	EMF red. χ^2
Unstacked	(338.8 ± 0.3)	(329.9 ± 2.5)	1.4	1.2
Stacked Runs	(336.36 ± 0.07)		9.1	

Because the calibration with the constrained β parameter in the M line diffusion part was used, the comparison with the worse FWHM is more meaningful. The higher statistics due to the stacking leads to a more accurate value, but only for the FWHM. The overall spectrum is worse described by the function.

For clarification of the worsening of the reduced χ^2 with the number of stacked runs for pixel 28, representing all working pixels, a plot was created in figure 5.23.
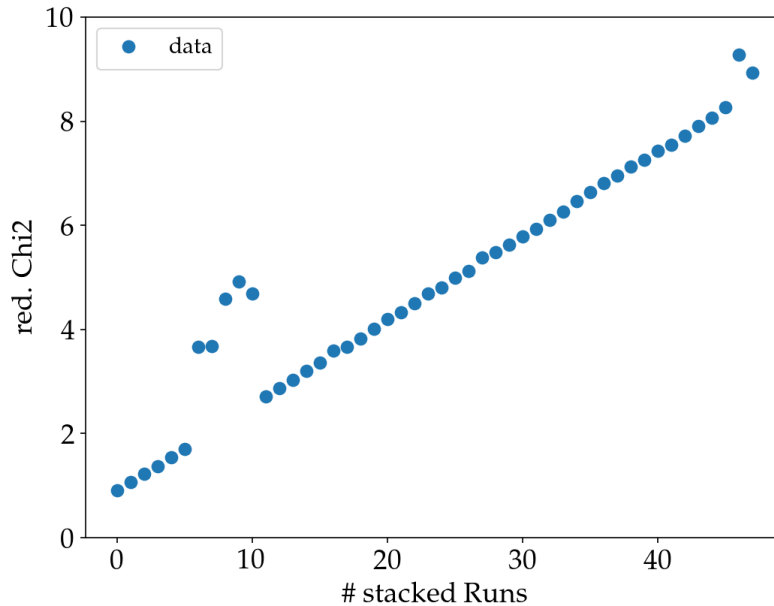
Figure 5.23: Reduced χ^2 over number of stacked runs for pixel 28. This course represents the agreement of the empirical model function (see equation 5.6) and the data after calibration with two Gaussian functions. Seven outliers can be identified. They could be caused by external influences on the data.

In total, the reduced χ^2 worsens over time, caused by the increasing statistics. With these increasing statistics, the empirical function could need more free parameters. The reason is that more statistics resolve substructures in the energy spectrum that are not described by the empirical model function. Seven outliers can be observed in the figure 5.23. They could be caused by external influences, leading to variations in the data and therefore worsen the agreement between the model fit and the data. A possible explanation is that the fit did not find the right minimum, but a local one. These seven outliers can also be identified in figure 5.24.
Here, the energy resolution in terms of the FWHM is plotted versus the number of stacked runs for pixel 28. In total, the FWHM follows a constant course. The uncertainties decrease with the number of stacked runs because the statistic increases, so the FWHM gets more accurate.
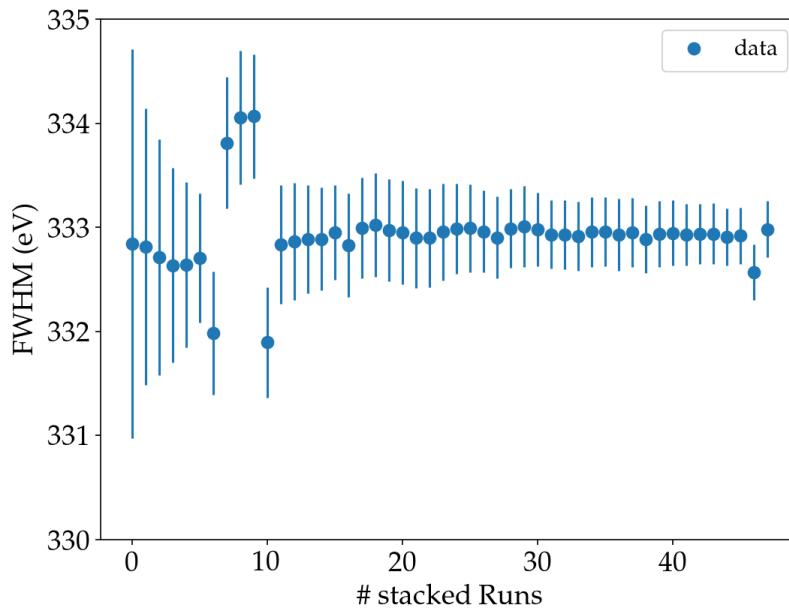
Figure 5.24: Energy resolution represented by the FWHM (eV) over the number of stacked runs for pixel 28. The more runs were stacked, the smaller the uncertainty became. This is caused by an increasing statistics. Also in this plot the seven outliers can be identified.

Calibration with empirical model function

The same procedure was used for the energy spectra calibrated with the empirical function. First, the peak positions of the $L - 32$ and $M - 32$ line were plotted over the time for pixel 14 in figure 5.25.

Also, the energy resolution in terms of the FWHM is shown for the different hours. The deviation of the peak positions is again less than $5\,\text{eV}$ and therefore negligible compared to the mean value of the FWHM of $(332.3 \pm 0.2)\,\text{eV}$. The deviation in keV can be read on the right axis. The mean peak positions in keV were calculated with the mean of the calibration parameters and the theoretical values derived in section 5.2 with $(31.4515 \pm 0.0004)\,\text{keV}$ for the $L - 32$ line and with $(32.9339 \pm 0.0005)\,\text{keV}$ for the $M - 32$ line with the added source voltage. On the right side, the histograms of all plots are shown and indicate an approximate Gauss distribution. With this result, the energy spectra of three pixels at different positions on the detector were stacked over the runs before they were calibrated. The resulting spectra with the fitted empirical model function (see equation 5.8) after calibration are shown in figure 5.26.
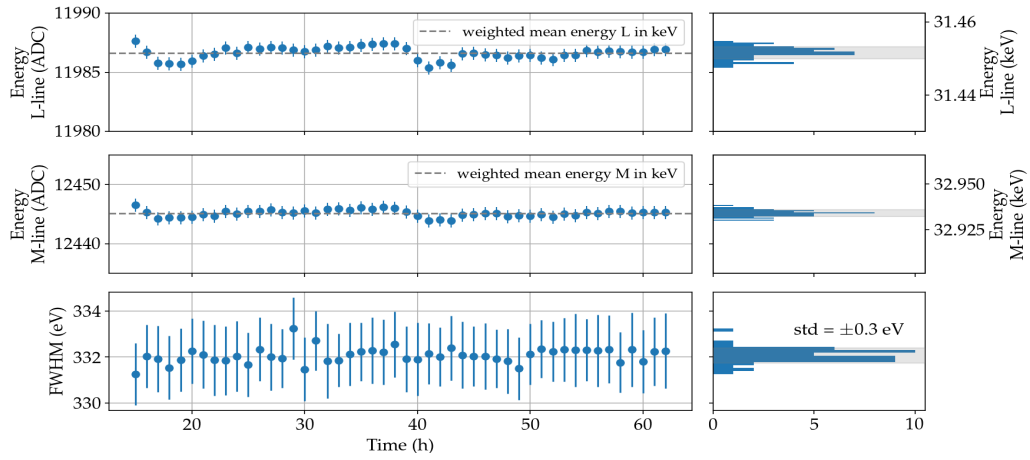
Figure 5.25: Time stability investigation plot of the calibration. Pixel 14 is representative of all working pixels. The two upper plots show the peak position of the $L - 32$ and $M - 32$ line, respectively, in energy (left: ADC, right: keV) over time (h). The theoretical peak positions, that were derived with the mean of the calibration parameters for both lines, were calculated in section 5.2. The bottom plot shows the FWHM in eV over time (h). The weighted mean was calculated to (332.3 ± 0.2) eV. Overall the deviation of the peak positions of the $L - 32$ and $M - 32$ line from the calculated theoretical line is less than 5 eV in both cases. On the right side histograms show that one can assume a Gauss distribution of the data points.
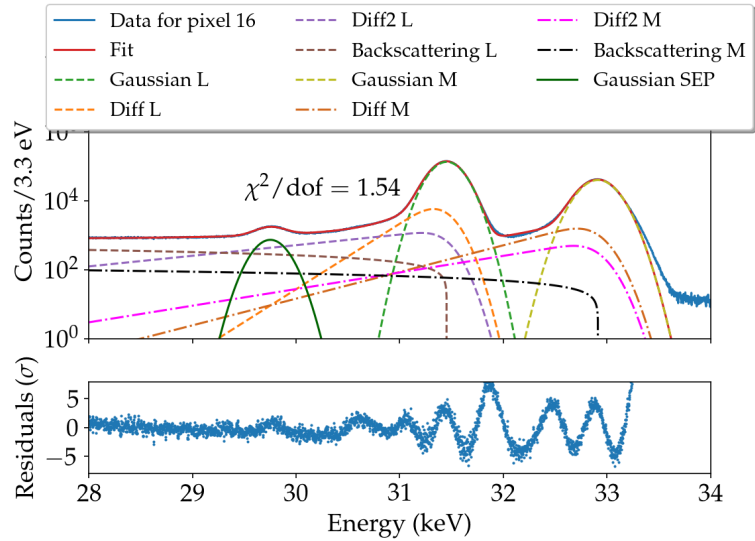
(a) Energy spectrum of pixel 16 with fitted empirical function after calibration with the same function. The data was stacked over the runs.
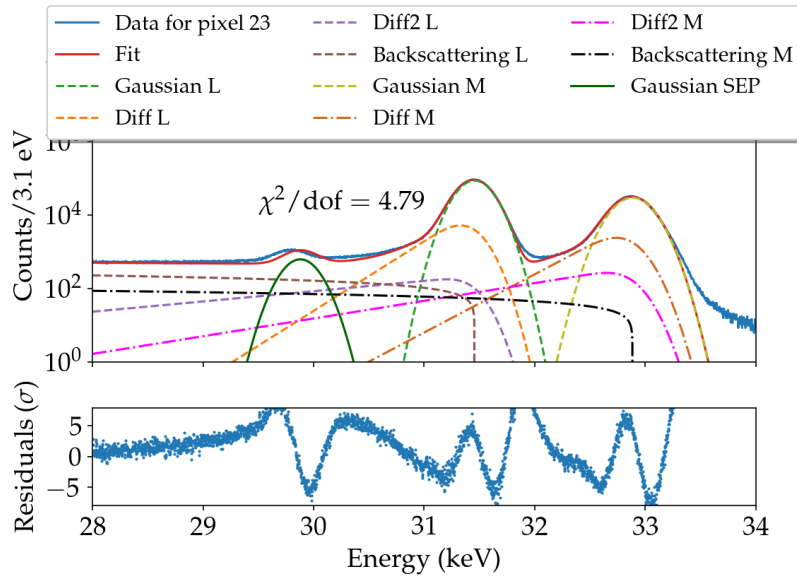
(b) Energy spectrum of pixel 23 with fitted empirical function after calibration with the same function. The data was stacked over the runs.
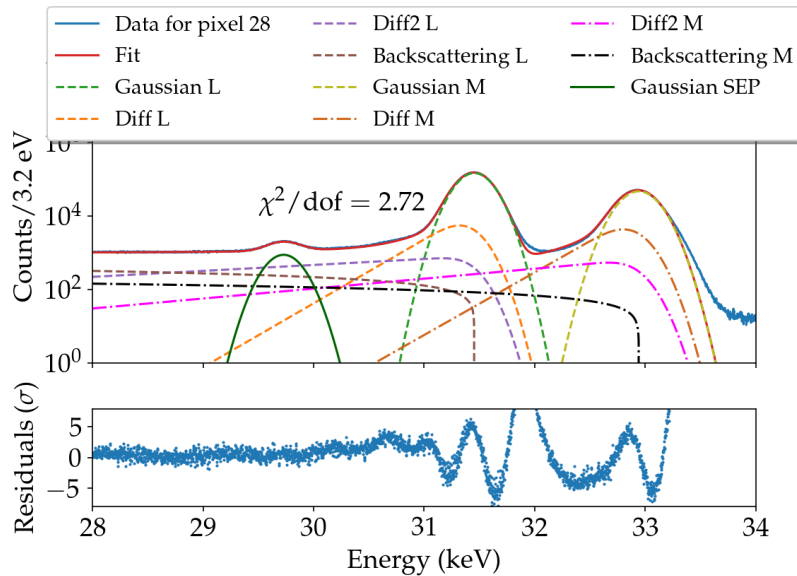
(c) Energy spectrum of pixel 28 with fitted empirical function after calibration with the same function. The data was stacked over the runs.

Figure 5.26: Empirical model function (see equation 5.6) fitted in the energy spectra of three different pixels. The spectra were calibrated with the same empirical model function before stacking over the runs. The single parts of the empirical model are plotted in the energy spectrum, and the residuals are shown in the bottom plots.

All three pixels have smaller reduced χ^2 than when calibrated with the Gaussian functions. Pixel 16 has a reduced χ^2 of 1.54, pixel 23 of 4.79 and pixel 28 of 2.72. This leads to a lower value of approximately a factor of 3 compared to the Gaussian calibrated energy spectra. In the bottom plots of figure 5.26, it can also be seen that the structure in the residuals of the backscattering part more or less vanished. After stacking all runs of each pixel, a color-indexed pixel map was created and is shown in figure 5.27.
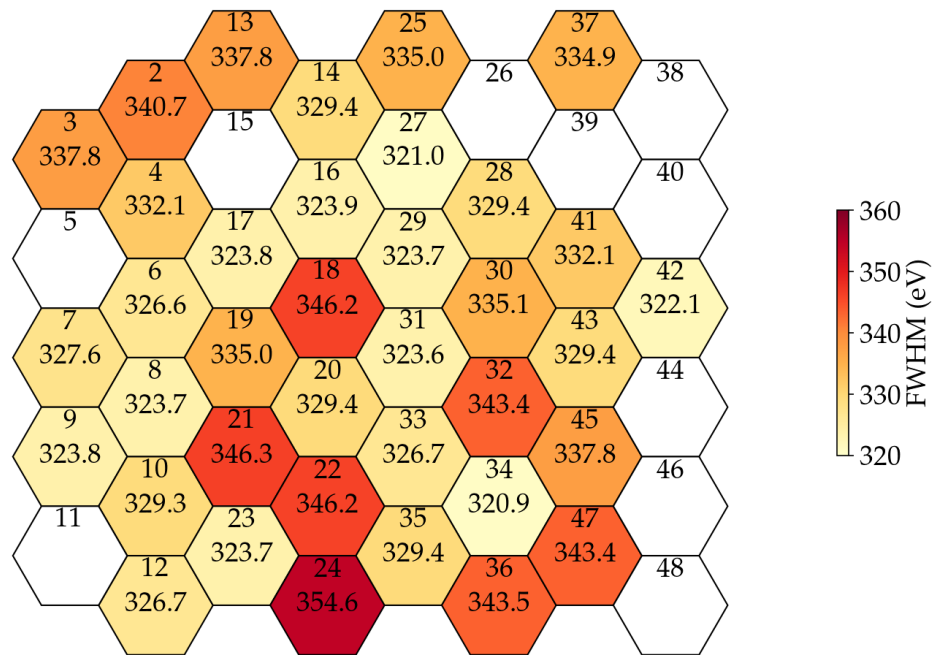
Figure 5.27: Color-indexed pixel map of the FWHM obtained after stacking all runs and calibrating the energy spectra with the empirical model function. The values of the FWHM are in the same range as the ones before stacking the runs, between 320 eV and 360 eV (see figure 5.17). The mean value of the energy resolution after stacking the runs is (331.53 ± 0.06) eV FWHM.

With a mean value of (331.53 ± 0.06) eV for the energy resolution, stacking of the runs did not worsen the FWHM. On the contrary, the range of the values stayed the same, between 320 eV, and 360 eV. Also, in comparison to the FWHM obtained after the Gaussian calibration (see figure 5.22), the values of the FWHM even slightly improved. This can be seen in table 5.6.

Table 5.6: Mean FWHM values and reduced χ^2 of unstacked energy spectrum for both calibration methods, Gaussian function (GF) and empirical model function (EMF). Also the mean FWHM value and the reduced χ^2 of the energy spectrum with stacked runs are shown. The values are given for pixel 28.

	GF FWHM (eV)	EMF FWHM (eV)	GF red. χ^2	EMF red. χ^2
Unstacked	(338.8 ± 0.3)	(329.9 ± 2.5)	1.4	1.2
Stacked Runs	(336.36 ± 0.07)	(331.53 ± 0.06)	9.1	2.72

A look at the course of the reduced χ^2 over the number of stacked runs in figure 5.28 shows a flatter slope than for the Gaussian calibrated spectra. The rough change in the reduced χ^2 per run is about 0.17 for figure 5.23. This is about a factor of 2.5 worse for the Gaussian calibrated reduced χ^2 than for the empirical function's calibration, which has a value of 0.07 per run.
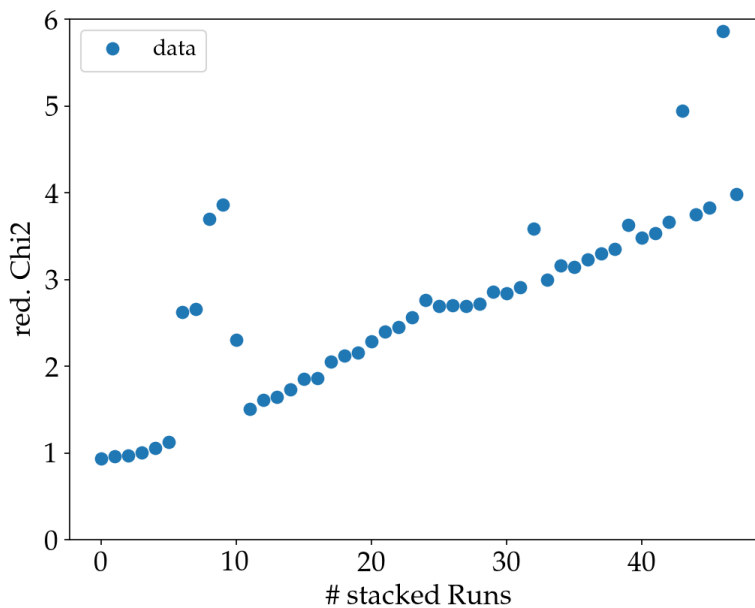
Figure 5.28: Reduced χ^2 over number of stacked runs for a pixel. This course represents the agreement of the empirical model function (see equation 5.6) and the data after calibration with the same empirical function. Nine outliers can be identified. External influences on the data could cause them. The course is flatter than for the reduced χ^2 obtained by the Gaussian calibrated energy spectra with stacked runs. This shows that the calibration with the empirical model function leads to more meaningful results.

Therefore, it can be concluded that the data after calibration with the empirical model function when stacking the runs agrees better with the same empirical model function. A few outliers, present in the course of the reduced χ^2, indicate some external effects on the energy spectrum.

The course of the FWHM with the number of stacked runs indicates the correctness of the statement. Figure 5.29, also shows some outliers.
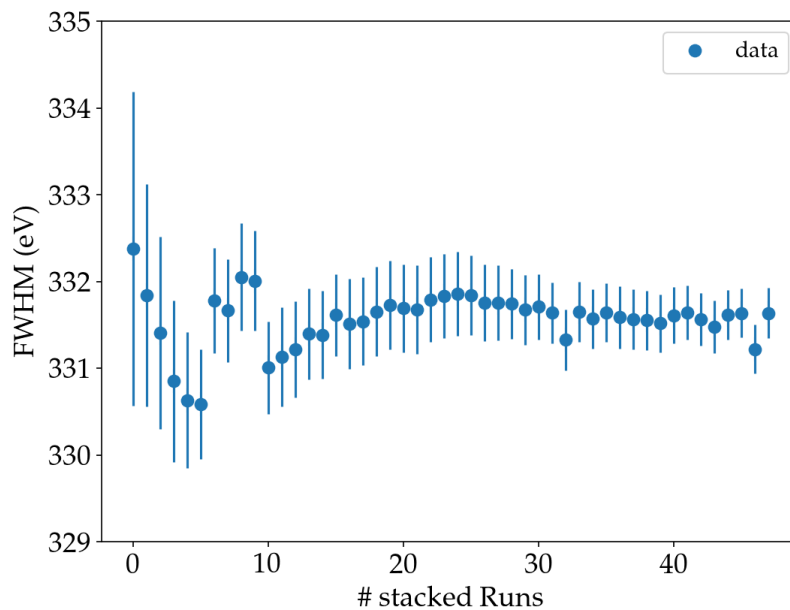
Figure 5.29: Energy resolution represented by the FWHM (eV) over the number of stacked runs for pixel 28. The more runs were stacked, the smaller the uncertainty became. This is caused by an increasing statistics. Four of the nine outliers identified in figure 5.28 can also be seen in this plot.

Although the deviation of the FWHM seems higher than in figure 5.24, the maximum value is smaller. The smaller values of the reduced χ^2, and the reduction of the structure in the residuals of the backscattering part suggest that using the empirical function for the calibration and stacking the runs is a reasonable approach to reduce free parameters.

5.4.2 Stacking of Pixels

For the investigation of stacking the pixels, at first stacking before calibration was examined. Then the Gaussian calibrated energy spectra were used for stacking.

After that, the energy spectra calibrated with the empirical model function were investigated. In all cases, the energy spectra after stacking the runs were used.

Stacking before calibration

The first step was to check the deviation of the peak position between the different pixels. Therefore, the energy spectra were stacked over the runs. The peak positions of the $L - 32$ and $M - 32$ lines were plotted over the pixel number before the calibration. This is shown in the two upper plots in figure 5.30.
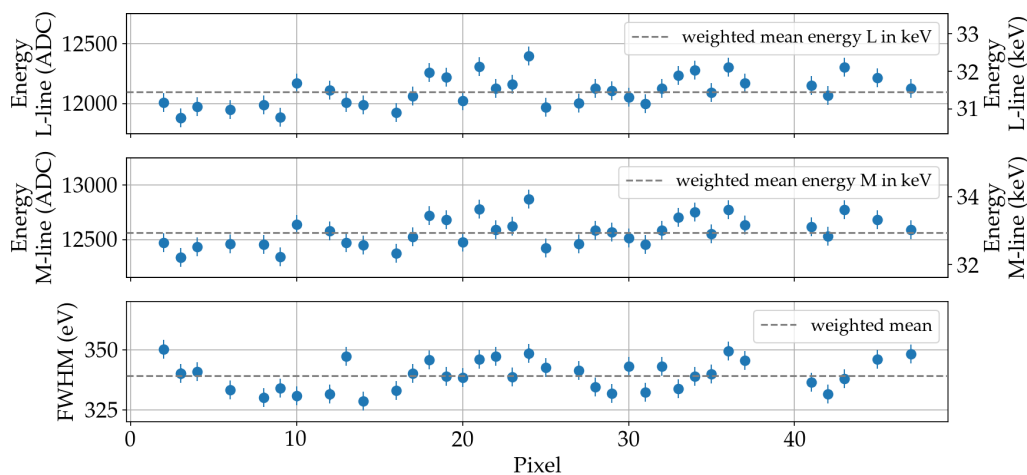
Figure 5.30: Investigation of pixel stacking. The peak positions of the $L - 32$ line in the uncalibrated energy spectra for the different pixels are plotted in the upper plot. The middle plot shows the peak positions of the $M - 32$ line in the uncalibrated energy spectra for the different pixels. The left y-axes show the energy representing the peak position in ADC, the right y-axes in keV. In the bottom the FWHM is plotted against the pixels and the weighted mean of (338.76 ± 0.28) eV is marked. The peak positions of both the $L - 32$ and $M - 32$ lines are largely distributed up to 1 keV. Compared to the smaller FWHM obtained from the stacked runs after calibration with the Gaussian function, the value shows that stacking of the pixels is not reasonable. The calibration parameters of the first pixel were used.

On the left axis the peak positions in ADC can be seen, while on the right axis, the peak positions in keV are shown. In the bottom plot, the FWHM in eV is plotted over the pixels together with the weigthed mean at (338.76 ± 0.28) eV. The large distribution of both peak positions between the pixels of up to 1 keV in comparison to the smaller FWHM value indicates that stacking of the pixels is in general not

meaningful before the calibration. Also a high spread of these FWHM values of about 20 eV at maximum suggests that the pixels are too different to calibrate them together. These values were obtained with the stacked runs and Gaussian calibration with calibration parameters of the first pixel. This difference becomes even clearer when looking at the energy spectra of four stacked pixels in figure 5.31.
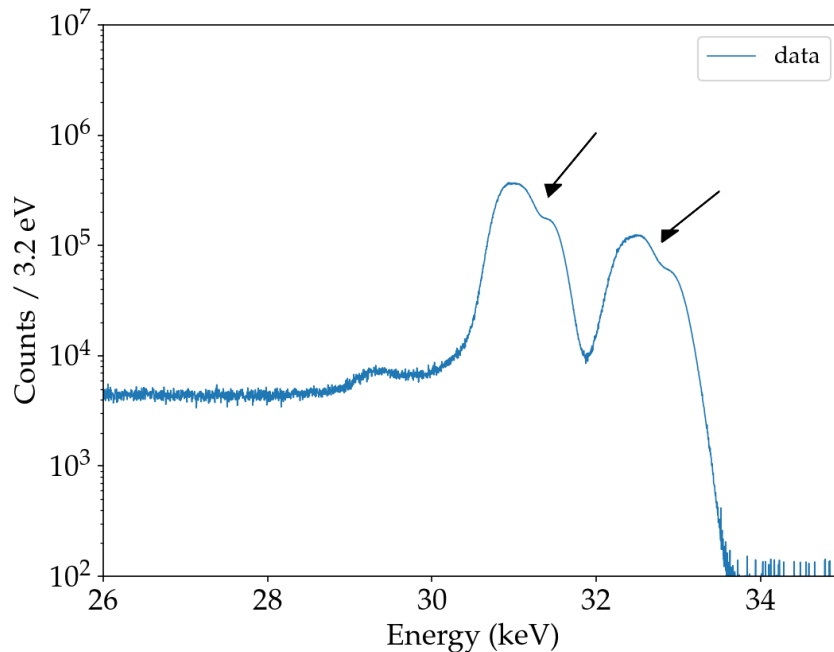
Figure 5.31: Energy spectrum of four stacked pixels. On top of the pixel with the best FWHM, a pixel with a worse FWHM was stacked. The FWHM values were determined from the energy spectra after stacking the runs. The spectra were calibrated after stacking runs and pixels. A bump is showing in the $L - 32$ and $M - 32$ line peaks. This bump is caused by the different behaviour of the pixels. It can be concluded that stacking of pixels is not reasonable before calibrating each pixel separately.

The pixels were successively stacked with worsening FWHM. This value was taken from the energy spectra with stacked runs. The spectra were then calibrated. This procedure leads to a bump in the $L - 32$ and $M - 32$ lines. From this it can be concluded that the pixels behave too differently for stacking them before the calibration.

Calibration with Gaussian functions - Stacking after calibration

Alternatively the pixels can be stacked after the calibration. After each stacked pixel, the empirical model function was fitted in the energy spectrum to look at the course of the detector response. Herewith the peak positions of both the $L - 32$ and $M - 32$ lines are fixed to the expected energy values. An important aspect is that the FWHM of the single pixels obtained after Gaussian calibration and stacking of runs do not agree within their uncertainty. This larger distribution of the FWHM values suggests that stacking the pixels might be smeared out the spectrum in a non Gaussian way. Nonetheless, the assumption has been verified by first, stacking all working pixels shown in figure 5.32 after calibration with two Gaussian functions in the order from best FWHM value to worst FWHM value.
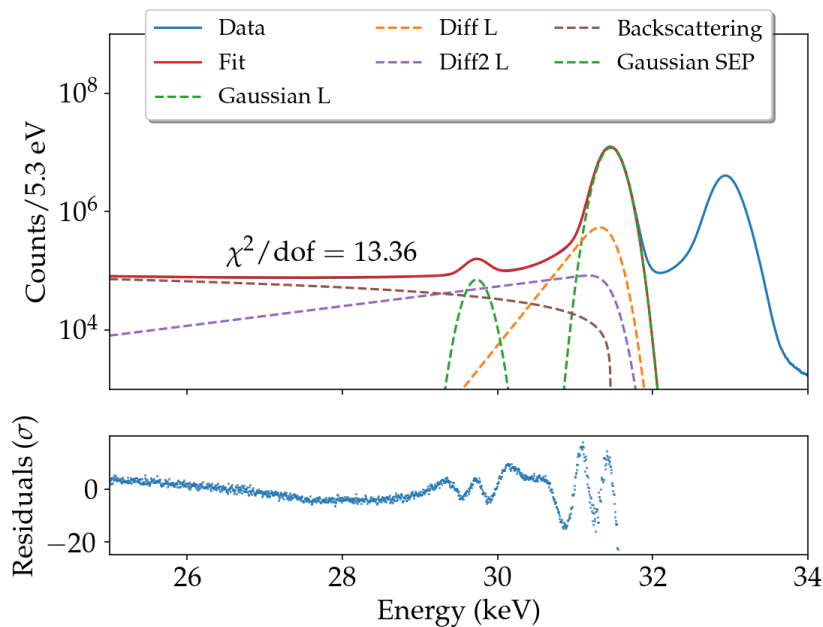
Figure 5.32: Calibrated energy spectrum after stacking all working pixels from best to worst FWHM. The FWHM was obtained by the energy spectra with stacked runs. In the upper part the adjusted special empirical model function is fitted into the spectrum. It consists of the Gaussian function, two diffusion functions and a backscattering function for the $L - 32$ line, and also a Gaussian function for the silicon escape peak (see equation 5.9). For simplicity, the $M - 32$ line was not fitted. A reduced $\chi^2 = 13.36$ and a FWHM of $(333.8 \pm 0.2)\,\text{eV}$ were obtained. In the bottom, the residuals are shown.

These values were taken from the energy spectra with stacked runs. In the figure, also a simplified empirical model function is fitted in the energy spectrum consisting of a Gaussian function, two diffusion functions and a backscattering function for the $L - 32$ line and a Gaussian function for the silicon escape peak (see equation 5.9).

$$I_{\text{L line}}(E) = I_{G_{\text{L line}}}(E) + I_{D1_{\text{L line}}}(E) + I_{D2_{\text{L line}}}(E) + I_{B_{\text{L line}}}(E) + I_{\text{esc}}(E) \qquad (5.9)$$

Although the value of the FWHM with $(333.8 \pm 0.2)\,\text{eV}$ is in the order of the previous energy resolutions, the obtained reduced χ^2 of 13.36 is too high to get a meaningful information about the detector response. This high value is caused by the high statistics obtained through stacking of runs and pixels. The empirical model function is not sufficient to describe the energy spectrum of all runs and pixels stacked. That is due to the fact that tiniest and more detailed structures are revealed. The sequence of the stacked pixels plays a rather subordinate role here. This is not relevant for the final result, but it makes the fit more robust. In figure 5.33, the pixels were stacked numerically from 2 to 47.
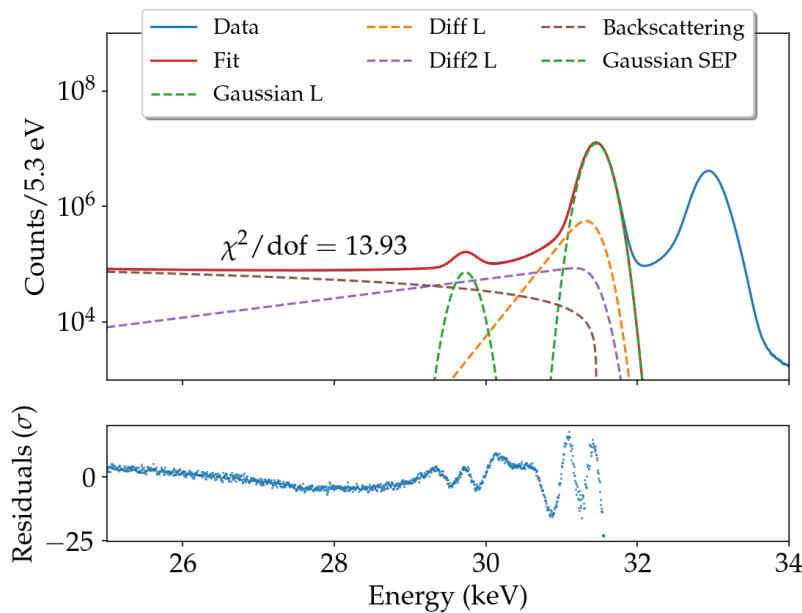
Figure 5.33: Calibrated energy spectrum after stacking all runs of the working pixels and then all working pixels from 2 to 47. In the upper part the adjusted special empirical model function is fitted into the spectrum. It consists of the Gaussian function, two diffusion functions and a backscattering function for the $L - 32$ line, and also a Gaussian function for the silicon escape peak (see equation 5.9) . For simplicity, the $M - 32$ line was not fitted. A reduced $\chi^2 = 13.93$ and a FWHM of $(338.8 \pm 0.3)\,\text{eV}$ were obtained. In the bottom, the residuals are shown.

The value of the reduced $\chi^2 = 13.93$ and of the FWHM had slightly deteriorated. In case of the FWHM, the value increased to (338.8 ± 0.3) eV.

Plotting the values of the reduced χ^2 over the number of stacked pixels, as shown in figure 5.34 seems to have a linear behavior as with the stacking of the runs.
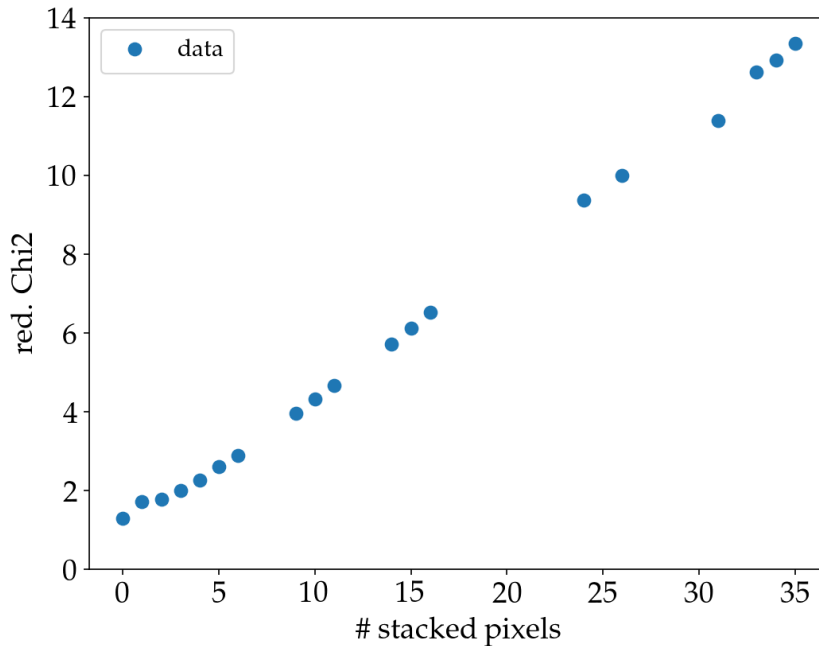
Figure 5.34: Reduced χ^2 over number of stacked pixels. This course represents the agreement of the empirical model function (see equation 5.9) and the data after calibration with the two Gaussian function and stacking of runs. After stacking of $8, 9, 13, 14, 18$ to $24, 26, 28, 29, 30, 31, 33$ pixels, the fit has not converged in between. Adding the next pixel often solved this problem that could come from little structures appearing in the higher statistics energy spectrum and are not described by the empirical model function.

The reduced χ^2 worsens with a factor of about 0.38 per stacked pixel. This is again about a factor of 2.2 worse than for stacking the runs after Gaussian calibration (see figure 5.23).

The energy resolution in terms of the FWHM also slightly increases with the number of stacked pixels. This can be seen in figure 5.35.
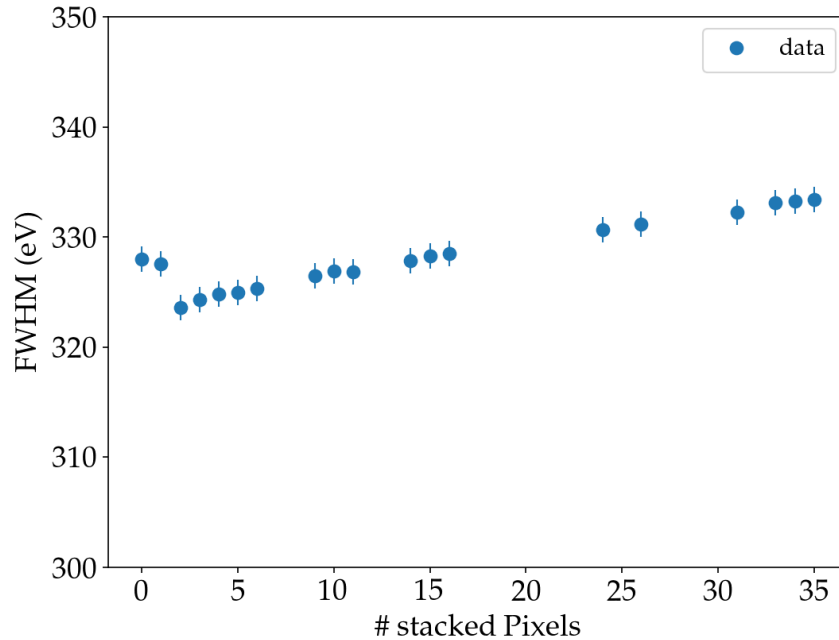
Figure 5.35: Energy resolution represented by the FWHM (eV) over the number of stacked pixels after calibration with two Gaussian functions stacking each run. The overall FWHM worsens with the number of stacked pixels. Here again some pixels are missing because the fit did not converge in these cases.

Both figures are missing values for a certain number of stacked pixels, namely $8, 9, 13, 14, 18$ to $24, 26, 28, 29, 30, 31, 33$ stacked pixels. This is due to the fact that the empirical model function did not converge for these number of pixels.
An alternative to stacking all working pixels, while still limiting the free parameters, would be to stack individual pixel groups. Here, pixels with a similar count rate can be used. The similar count rate comes about as a result of the ring like structure on the detector (see figure 5.1). Well-suited pixels would be, for example pixels $27, 42, 41, 28, 25$ and 37. Their stacked energy spectrum with the fitted simplified empirical function is shown in figure 5.36. The fit gives a reduced χ^2 of 1.63 and a FWHM value of (336.5 ± 0.1) eV. The good agreement of the model fit with the stacked data occurs also for other groups of pixels. Suitable groups are $[17, 19, 20, 33, 34, 47]$, $[14, 16, 29, 30, 43, 2, 4, 21, 36]$ and $[3, 7, 9, 10, 12]$. All fits in the energy spectra of these stacked pixel groups give values for the reduced χ^2 of below 2.
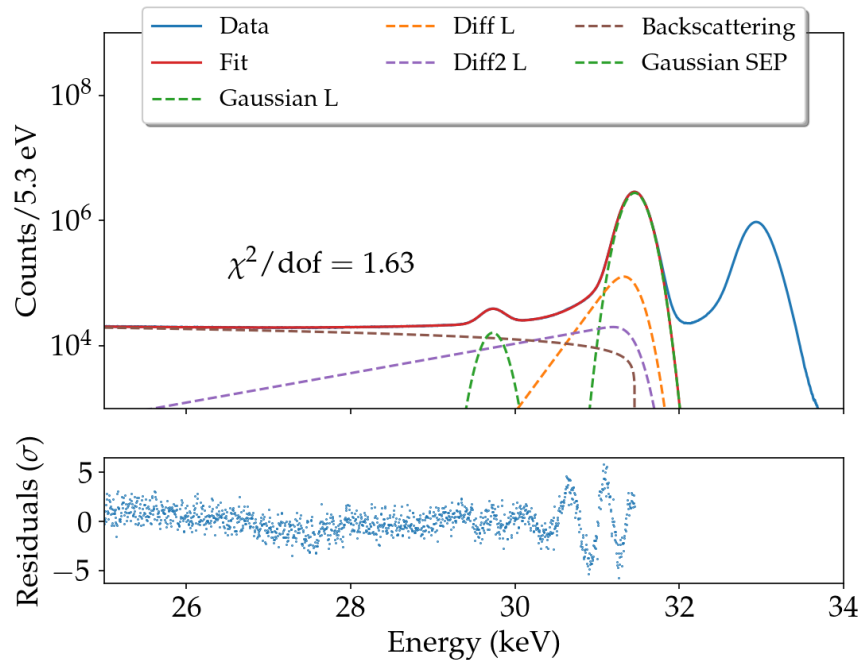
Figure 5.36: Calibrated energy spectrum of a group of stacked pixels. Pixels $27, 42, 41, 28, 25$ and 37 were grouped together because they all had a similar count rate. With this approach the free parameters can be reduced without risking non-convergence. The small reduced $\chi^2 = 1.63$ and the energy resolution of $(336.5 \pm 0.1)\,\text{eV}$ confirm this.

The extension of the model function by the M line does not lead to any result. No fit was converging and therefore no detector response could be obtained. This leads to the assumption that the empirical model function does not yet fully describe the energy spectrum of krypton. One possibility would be to investigate a model extension, the other would be to work only with the L line. With the current empirical model function, however, a stacking of all pixels cannot be evaluated in a meaningful way.

Calibration with empirical model function - Stacking after calibration

The second approach was calibration of the energy spectra with the empirical model function (see equation 5.6) before stacking the runs. The FWHM values obtained from this were then used to obtain a stacking order for the pixels. The energy spectrum after stacking all working pixels in this order is shown in figure 5.37.
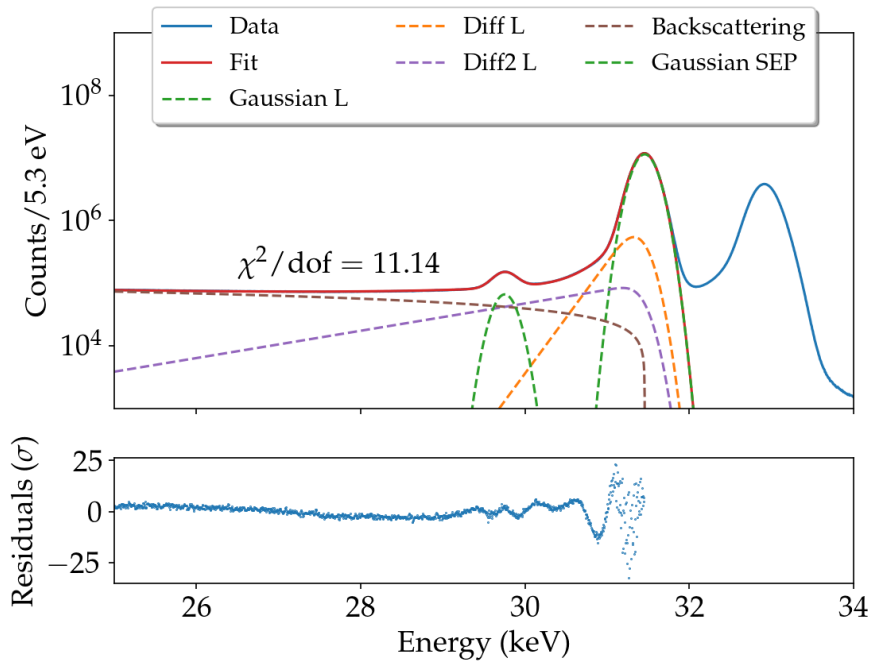
Figure 5.37: Calibrated energy spectrum after stacking all working pixels from best to worst FWHM. The FWHM was obtained by the energy spectra with stacked runs. In the upper part the adjusted special empirical model function is fitted into the spectrum. It consists of the Gaussian function, two diffusion functions and a backscattering function for the $L - 32$ line, and also a Gaussian function for the silicon escape peak. For simplicity, the $M - 32$ line was not fitted. A reduced $\chi^2 = 11.14$ and a FWHM of $(335.3 \pm 0.2)\,\text{eV}$ were obtained. In the bottom, the residuals are shown.

In the energy spectrum the adjusted empirical model function (see equation 5.9) was fitted and the single parts of this functions are plotted. The reduced χ^2 of 11.14 is smaller than the one determined for the Gaussian calibrated energy spectrum. This is because the Gaussian function disregards the other main characteristics and therefore agrees worse the data, leading to more shifts in the calibration depending on the energy resolution or the diffusion term. The value of the FWHM slightly increased to $(335.3 \pm 0.2)\,\text{eV}$. These results were then compared to the values obtained by stacking the pixel numerically, as shown in figure 5.38.
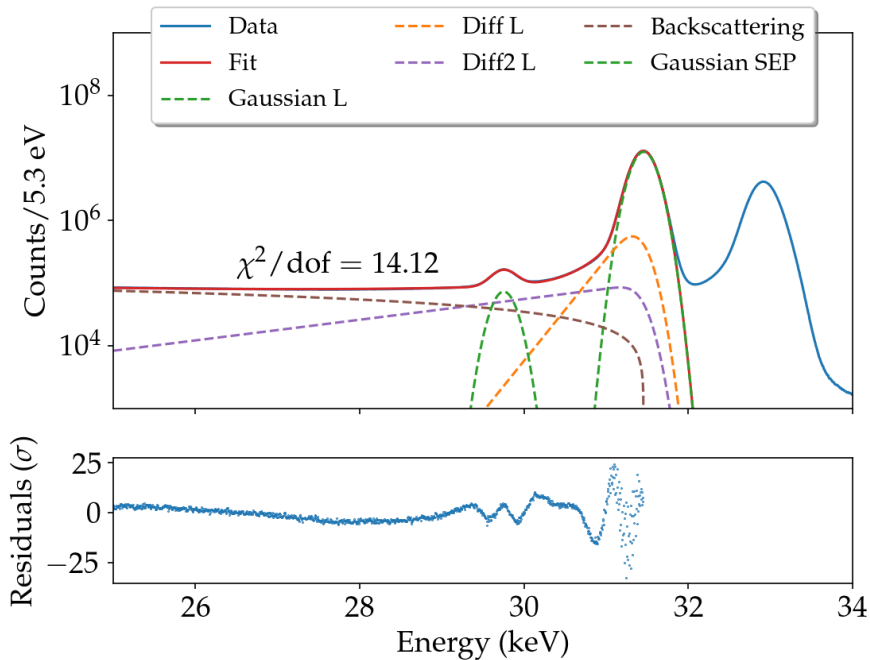
Figure 5.38: Calibrated energy spectrum after stacking all runs of the working pixels and then all working pixels from 2 to 47. In the upper part the adjusted special empirical model function is fitted into the spectrum. It consists of the Gaussian function, two diffusion functions and a backscattering function for the $L - 32$ line, and also a Gaussian function for the silicon escape peak. For simplicity, the $M - 32$ line was not fitted. A reduced $\chi^2 = 14.12$ and a FWHM of $(329.2 \pm 0.4)\,\text{eV}$ were obtained. In the bottom, the residuals are shown.

The plot shows the energy spectrum calibrated with the empirical model function (see equation 5.6) with stacked runs and numerically stacked pixels. The reduced χ^2 deteriorates to a value of 14.12 and thus becomes even worse than the value of the Gaussian calibration (see figure 5.33). A reason could be that for the sorted stacking, pixels with similar FWHM and therefore similar behavior were stacked first and the fit could adapt better. This is an indication that the fit does not converge at the global minima and rather a local one depending on the order of pixels stacked. Plotting the reduced χ^2 over the number of stacked pixels shows again a linear behavior as with the stacking of the runs and stacking of pixels after Gaussian calibration. The reduced χ^2 worsens about 0.39 for every added pixel. This can be seen in figure 5.39.
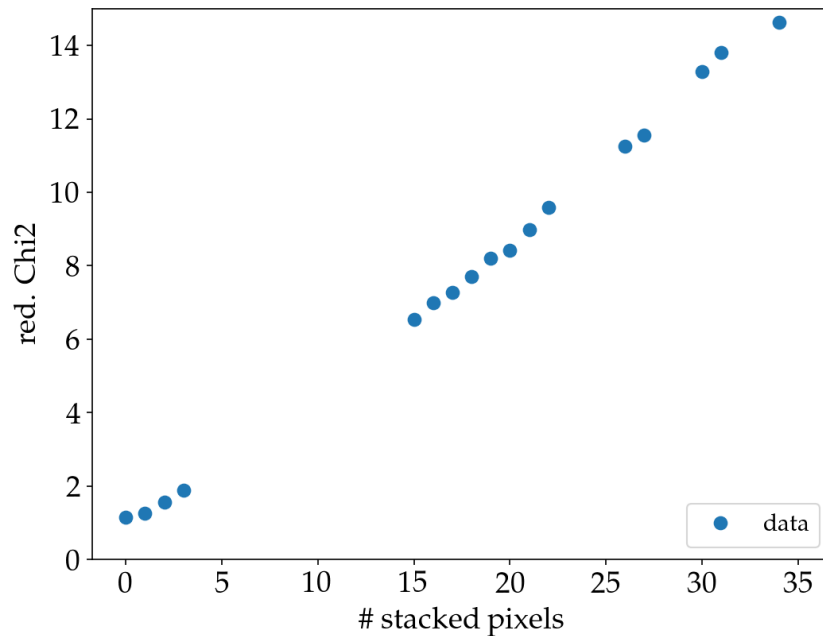
Figure 5.39: Reduced χ^2 over number of stacked pixels. This course represents the agreement of the empirical model function (see equation 5.9) and the data after calibration with the empirical model function and stacking of runs. After stacking of 4 to 14, 23, 24, 25, 28, 29 and 32 pixels, the fit has not converged in between. Adding the next pixel often solved this problem that could come from little structures appearing in the higher statistics energy spectrum and are not described by the empirical model function.

It is almost the same like the change of the reduced χ^2 per pixel when calibrating with the Gaussian functions (see figure 5.34). Also the FWHM worsens with the number of stacked pixels, shown in figure 5.40.
In both cases the fit did not converge after stacking of a certain number of pixels. The number of stacked pixels were 4 to 14, 23, 24, 25, 28, 29 and 32. Again the reason could be substructures revealed with higher statistics by stacking so much data. Here again, stacking of the next pixel often solved the problem. A comparison of the FWHM courses for both calibrations can be found in figure 5.41.
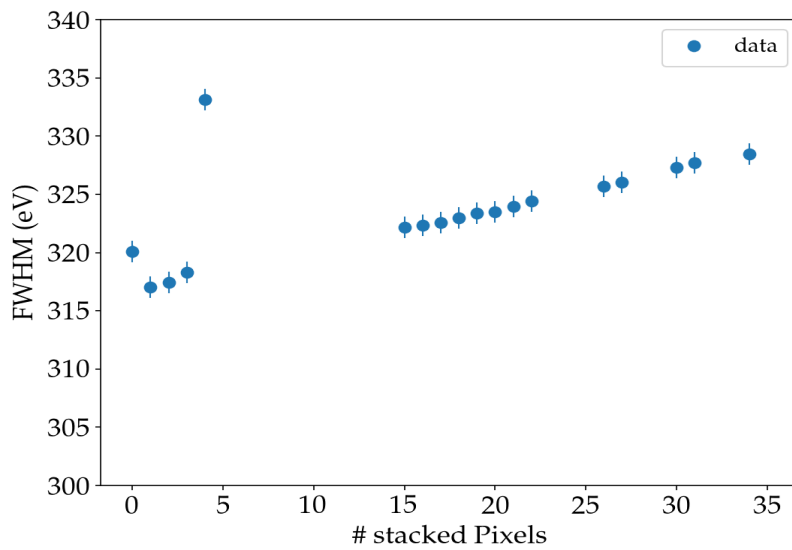
Figure 5.40: Energy resolution represented by the FWHM (eV) over the number of stacked pixels after calibration with the empirical model function and stacking each run. The overall FWHM worsens with the number of stacked pixels. Here again some pixels are missing because the fit did not converge in these cases.
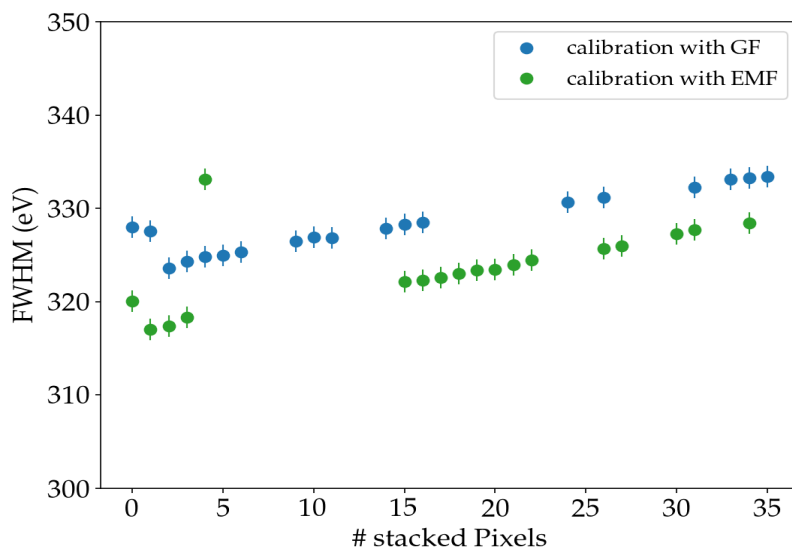
Figure 5.41: FWHMs obtained after stacking of pixels after calibration with both methods, Gaussian functions (GF) and empirical model function (EMF). After each stacked pixel, the FWHM was derived.

The approach of stacking only groups of pixels with similar count rates, is again applied. The calibrated energy spectrum of a group of five pixels stacked in numerical order is shown in figure 5.42.
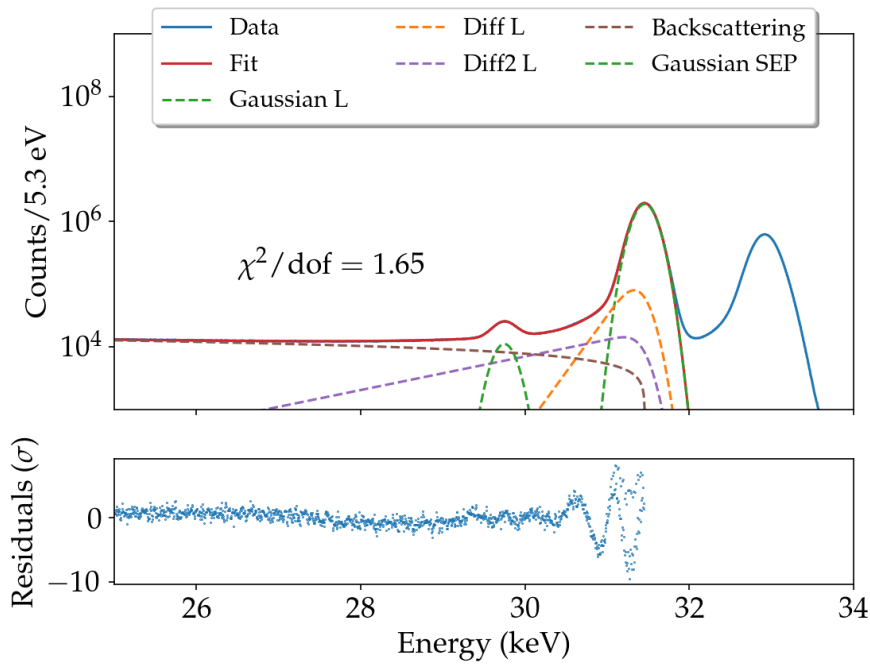
Figure 5.42: Calibrated energy spectrum of a group of stacked pixels in numerical order. Pixels $14, 16, 29, 30$ and 43 were grouped together because they all had a similar count rate. With this approach the free parameters can be reduced without risking non-convergence. The small reduced $\chi^2 = 1.65$ and the energy resolution of (325.5 ± 0.3) eV confirm this.

For the calibration the empirical model function 5.6 was used. The small values for the reduced $\chi^2 = 1.65$ and the FWHM (325.5 ± 0.3) eV confirm this approach. Free parameters can be reduced without compromising in the robustness and the agreement of the data with the fit model.
One of many attempts to fit the entire empirical function (see equation 5.6) into the ordered stacked energy spectrum resulted in a reduced $\chi^2 = 39.15$ and a FWHM of (328.8 ± 0.5) eV. It is shown in figure 5.43.
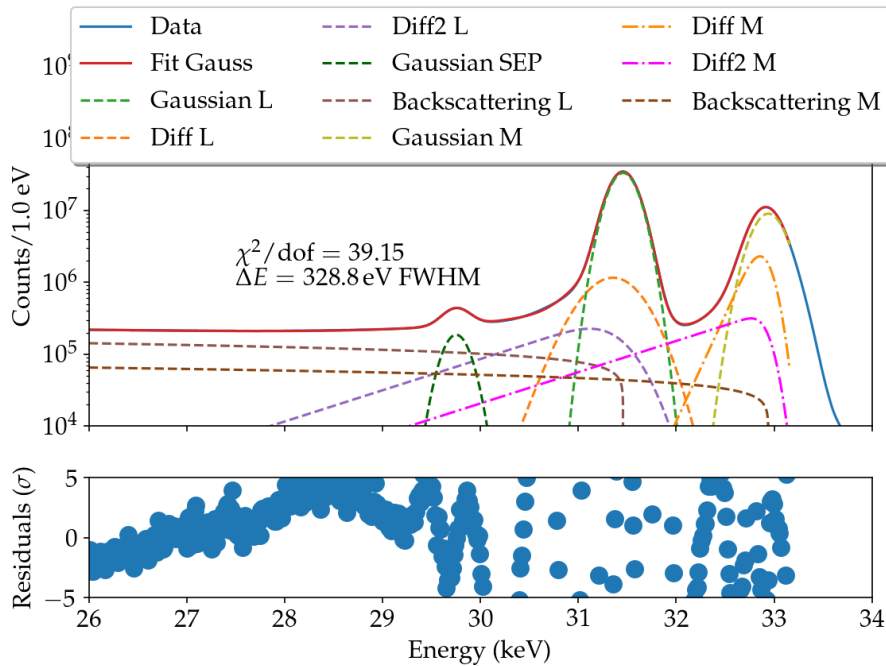
Figure 5.43: Calibrated energy spectrum of all working pixels stacked from best FWHM to worst FWHM. The empirical model function (see equation 5.6) for the $L - 32$ and $M - 32$ line is fitted in the spectrum. The single parts of the function are also plotted. In the bottom the residiuals are shown. The reduced $\chi^2 = 39.15$ and the energy resolution of $(328.8 \pm 0.5)\,\text{eV}$ were not reproducible. The empirical model function is not yet accurate enough for such high statistics.

It is not recommended to work with this approach because the fit is difficult to reproduce. The susceptibility of the fit is caused by the high statistics and the incomplete empirical model function. Either the empirical model function should be expanded or the focus should be on the $L - 32$ line of individually stacked pixel groups. Otherwise, the detector response cannot be described in a meaningful way.

5.4.3 Conclusion

From this section it can be concluded, that stacking the runs could be done before calibration of the energy spectra. The reduced χ^2 when stacking the runs and calibrating with the Gaussian functions is in total over 5 for all pixels, while it is under 5 for the calibration with the empirical function. Also the difference in the change of the reduced χ^2 per run between the two calibrations is not negligible. For

the Gaussian calibration with a change of 0.17 per run, it is a factor of 2.5 worse. In addition, the mean FWHM is about 5 eV smaller for the pixels calibrated with the empirical function. Apart from the lower robustness of the fit, it is still more effective to calibrate with the empirical model function. For a better overview, all FWHM mean values are shown in table 5.7.

Table 5.7: FWHM values of unstacked energy spectra, FWHM after stacking the runs, calibration with Gaussian function (GF) or empirical model function (EMF) after stacking pixels from best FWHM value to the worst FWHM value. Also the reduced χ^2 is shown for each case.

	GF FWHM (eV)	EMF FWHM (eV)	GF red. χ^2	EMF red. χ^2
Unstacked	(338.8 ± 0.3)	(329.9 ± 2.5)	1.4	1.2
Stacked Runs	(336.36 ± 0.07)	(331.53 ± 0.06)	9.1	2.72
Stacked Pixels	(333.8 ± 0.2)	(335.3 ± 0.2)	13.36	11.14

In the case of stacking the pixels, the pixels must be first calibrated individually to compensate for the inequality of the pixels. It is not recommended to stack all pixels neither in the order from best to worst FWHM nor in numerical order. Also the calibration method is not crucial for a better reduced χ^2.
In both cases, however, it makes more sense to stack the pixels in groups of similar count rates. The ring-like structure of the total count rate (see figure 5.1) can be used as a good guide.

6 Conclusions

This thesis investigated the effect of data combination on the energy resolution of the 47-pixel 3D prototype S0-47-3 silicon drift detector in the KATRIN monitor spectrometer. The monitor spectrometer is part of the KATRIN experiment setup and has the same mode of operation. Therefore the monitor spectrometer provides realistic conditions to test the later operation in the KATRIN experiment. Those conditions are an ultra-high vacuum and electric and magnetic fields to guide the electrons adiabatically to the detector.

The aim is to determine the stability and homogeneity of the detector parameters in order to define and reduce calibration intervals. A special empirical model function was used to determine the energy resolution as part of these parameters. This function was used because calibration with two simple Gaussian functions is insufficient to describe the data. The features described by the empirical function are the main peak coming from the electrons deposing almost their entire energy in the detector, the diffusion part considering the dead layer effect, the backscattering part for the backscattered electrons, and the silicon escape peak. The latter describes the energy emitted by the excited detector material.

First, electrons emitted by the spectrometer electrode were used to investigate the detector response. To measure electrons at different energies the spectrometer high voltage was varied. The obtained FWHM was (348.67 ± 0.92) eV for 30 keV electrons and a dead layer of about 80 nm via the energy shift was estimated. This dead layer thickness is in the range that should be achieved for the final TRISTAN detector.

The second electron source used to investigate the stability and the homogeneity was a ^{83m}Kr source. The conversion electrons of the L and M were used to determine the detector parameters. During data selection, 10 pixels out of 47 pixels having issues with the waveform were rejected. Also, the first 14 runs, and the last 3 runs were discarded because the measurement environment was not in a stable condition and the datasets were not complete. A FWHM mean value for the single, unstacked pixels of (337.0 ± 0.4) eV was determined.

The parameters for the investigation of the stability and homogeneity were obtained from calibration with the empirical model function. The parameters were the peak positions of the L and M lines and the energy resolution. This energy resolution had

a deviation of about 5 eV. The variance of the FWHM was ± 0.4 eV. Therefore, it was concluded that stacking the runs over 40 h is possible and should not influence the energy resolution. A correlation with temperature was also seen, but this could be neglected in here due to its low impact on the data. The realization of stacking runs is essential for the TRISTAN project because as a very high number of runs will be recorded here, the calibration intervals should be kept as low as possible.

The possibility of combining the pixels was investigated by looking at the parameter stability and homogeneity. Again the peak positions of the *L* and *M* lines were compared, and the spread of the energy resolution was determined. It was concluded that the pixels are too different for a combination before calibration. Stacking after calibration leads to 1480 times the data obtained at one run for one pixel. With this high statistic, one finds out that the empirical model function is not accurate enough leading to worse fitting results. Nevertheless, the combined energy resolution is more accurate with a value of (335.3 ± 0.2) eV. This value is still to high for the TRISTAN requirement of less than 300 eV at 20 keV, but because the krypton lines are in the region of 30 keV, this is in an expected range.

An alternative for stacking all working pixels at once could be the stacking of pixels in groups with similar count rates.

Within this thesis, it could be shown that stacking individual pixels over time could be feasible when looking at the energy resolution. Nevertheless, an improved model for the detector electron response and further investigations on the temperature dependence of the calibration is required to describe measurements down to a precision in the ppm level.

A Appendix

A.1 Calculation of different Values

A.1.1 Calculation of FWHM and Electronic Fano Noise

The Full Width at Half Maximum (FWHM) was determined algorithmically by first identifying the index of the counts maximum. Then, on the left and on the right side of this index, it was searched for the closest index to half of the count maximum. The difference between the energies at these indices yielded the FWHM.

The electronic noise for the Fano limit was calculated with equation A.1.

$$\sigma_{el} = FWHM_{data} - \sigma_{Fano,FWHM} \tag{A.1}$$

The value $FWHM_{data}$ was the FHWM obtained by the data, while $\sigma_{Fano,FWHM}$ is the calculated Fano limit in terms of FWHM.

A.1.2 Statistics

Data Binning

Data binning was done to reduce small effects in the observed data that occur from errors during data acquisition. Therefore, an flattened array consisting of the cumulative sum of the y dataset is concatenated. The concatenated array and the x dataset are then used for interpolation. Also, the new x bins are interpolated and then used to calculate the discrete difference along the flattened y axis. This new array is then the binned y dataset.

Weighted Mean

All weighted means $\overline{x}$ were calculated with equation A.2.

$$\overline{x} = \frac{\Sigma_{i=1}^{n} \left(\frac{x_i}{\sigma_i^2} \right)}{\Sigma_{i=1}^{n} \frac{1}{\sigma_i^2}} \tag{A.2}$$

Here, x_i is the data point i and σ_i is the uncertainty of each data point. The standard deviation of the weighted mean $\sigma_{\bar{x}}$ can be calculated over the uncertainty σ_i of data point i with the equation A.3.

$$\sigma_{\bar{x}} = \sqrt{\frac{1}{\Sigma_{i=1}^{n} \sigma_i^{-2}}} \tag{A.3}$$

A.1.3 Calculation of Measurement Uncertainties

Uncertainty of the FWHM

The uncertainty of the FWHM depends only on the error of the width of the Gaussian $\sigma_{Gaussian}$. Equation A.4 shows this relation.

$$\Delta FWHM = 2\sqrt{2\ln 2}\Delta\sigma_{Gaussian} \tag{A.4}$$

Uncertainty of the Weighted Energy of the L and M Lines

With the simplified error propagation, the uncertainty of the weighted energy of the L line $L_{weighted}$ was calculated. The equation is shown in A.5.

$$\Delta L = \sqrt{\Delta E_{L_2}^2 \cdot \left(\frac{dL}{dE_{L_2}}\right)^2 + \Delta I_{L_2}^2 \cdot \left(\frac{dL}{dI_{L_2}}\right)^2 \quad \Delta E_{L_3}^2 \cdot \left(\frac{dL}{dE_{L_2}}\right)^2 + \Delta I_{L_3}^2 \cdot \left(\frac{dL}{dI_{L_3}}\right)^2} \tag{A.5}$$

It depends on the errors of the single energy lines L_2 and L_3 and their corresponding intensities I_2 and I_3 as well as the partial derivative of these values. The single derivation parts are shown in equation A.6 until A.9.

$$\frac{dL}{dE_{L_2}} = \frac{I_{L_2}}{I_{L_2} + I_{L_3}} \tag{A.6}$$

$$\frac{dL}{dI_{L_2}} = \frac{E_{L_2}}{I_{L_2} + I_{L_3}} - \frac{E_{L_2}I_{L_2} + E_{L_3}I_{L_3}}{\left(I_{L_2} + I_{L_2}\right)^2} \tag{A.7}$$

$$\frac{dL}{dE_{L_3}} = \frac{I_{L_3}}{I_{L_2} + I_{L_3}} \tag{A.8}$$

$$\frac{dL}{dI_{L_3}} = \frac{E_{L_3}}{I_{L_2} + I_{L_3}} - \frac{E_{L_2}I_{L_2} + E_{L_3}I_{L_3}}{\left(I_{L_2} + I_{L_2}\right)^2} \tag{A.9}$$

The uncertainty of the weighted energy of the M line can be calculated analogously.

Residuals

Calculation of the residuals were calculated, using equation A.10 with the measured data y_{data} and the data obtained by the fit y_{fit}.

$$Residuals = (y_{data} - y_{fit}) / \sqrt{y_{data}} \tag{A.10}$$

A.2 Python Fitting Package

The Python fitting package used in this thesis applies the Levenberg-Marquardt method for curve fitting. This method is a possible solution for non-linear least squares problems trying to find a local minimizer of the halved induced operator norm squared [57].
For the application of the least squares curve fitting method, the procedure was as follows. First, a model function was defined that describes the data. A fit range was then determined and the Model class of the lmfit package was applied. This class provides the Levenberg-Marquardt that is not only a fast but also a robust and efficient way of curve fitting. It uses variable parameters to fit the model function to the data automatically generating an appropriate residual function. In addition to the parameters, the function is also passed the independent variable.
However, since the parameters are not automatically created with the model, the method make_params must be used. It is important to generate initial values. The name and a floating point value must be passed here. Furthermore, the attribute vary and finite limits can be set to constrain the parameters. One possible attribute that the parameters can receive after fitting is the estimated standard error (stderr). The Model class has further methods that enable the actual fitting to be performed. In addition to the range, the parameters created and the weighting are also passed to lm.Model.fit(). The parameters copied into the input are returned as updated values. Also this method includes the data and methods to change and refit the parameters. Two other important methods of the Model class are redchi and best_fit. The first returns a Model attribute, the floating point reduced χ^2 statistic. It is calculated via equation A.11 [58].

$$\chi_\nu^2 = \frac{\chi^2}{(N - N_{varys})} \tag{A.11}$$

The reduced chi-square χ_ν^2 is composed of the chi-square (see equation A.12) over the difference of the number of observations N and the number of estimated free parameters N_{varys} [58].

$$\chi^2 = \Sigma_i^N [Residual_i]^2 \tag{A.12}$$

The residuals are calculated via equation A.10. The best_fit Model attribute returns an array of the model function with best-fit parameters.

The empirical model function used in this thesis was fitted by adding a part of the final function after each fitting step to determine the best parameters for the next step.

List of Figures

124

List of Tables

Bibliography

[1] T. Houdy et al. 'Hunting keV sterile neutrinos with KATRIN: building the first TRISTAN module'. In: *Journal of Physics: Conference Series* 1468.1 (Feb. 2020), p. 012177. DOI: `10.1088/1742-6596/1468/1/012177`.

[2] [Online; accessed April 15, 2022]. URL: `https://www.hll.mpg.de/`.

[3] L. Oberauer J. Oberauer. *Neutrinophysik*. Springer-Verlag GmbH Deutschland, 2019. ISBN: 978-3-662-59334-9.

[4] J. Chadwick. 'Possible Existence of a Neutron'. In: *Nature* 129.3252 (), p. 312. DOI: `10.1038/129312a0`.

[5] K. von Meyenn. *Wolfgang Pauli, Wissenschaftlicher Briefwechsel mit Bohr, Einstein, Heisenberg u.a.* Band II/Volume II: 1930-1939. Springer-Verlag, 1985. ISBN: 3-540-13609-6.

[6] E. Fermi. 'Versuch einer Theorie der β-Strahlen'. In: *I.Z. Physik* 88.3252 (1934), pp. 161–177. DOI: `10.1007/BF01351864`.

[7] C. L. Cowan et al. 'Detection of the Free Neutrino: a Confirmation'. In: *Science* 124.3212 (1956), pp. 103–104. DOI: `10.1126/science.124.3212.103`. URL: `https://www.science.org/doi/abs/10.1126/science.124.3212.103`.

[8] A. Serenelli L. Oberauer A. Ianni. *Solar Neutrino Physics*. John Wiley & Sons, Incorporated, 2020. ISBN: 9783527412761.

[9] T Morii, C S Lim and S N Mukherjee. *The Physics of the Standard Model and Beyond*. WORLD SCIENTIFIC, 2004. DOI: `10.1142/4655`. URL: `https://www.worldscientific.com/doi/abs/10.1142/4655`.

[10] R. Adhikari et al. 'A White Paper on keV sterile neutrino Dark Matter'. In: *Journal of Cosmology and Astroparticle Physics* 2017.01 (Jan. 2017), pp. 025–025. DOI: `10.1088/1475-7516/2017/01/025`.

[11] T. W. B. Kibble. *The Standard Model of Particle Physics*. 2014. DOI: `10.48550/ARXIV.1412.4094`. URL: `https://arxiv.org/abs/1412.4094`.

[12] R. Davis. 'A review of the homestake solar neutrino experiment'. In: *Progress in Particle and Nuclear Physics* 32 (1994), pp. 13–32. ISSN: 0146-6410. DOI: `https://doi.org/10.1016/0146-6410(94)90004-3`. URL: `https://www.sciencedirect.com/science/article/pii/0146641094900043`.

[13] M. C. Gonzalez-Garcia and Yosef Nir. 'Neutrino masses and mixing: evidence and implications'. In: *Reviews of Modern Physics* 75.2 (Mar. 2003), pp. 345–402. DOI: `10.1103/revmodphys.75.345`.

[14] K. Zuber. *Neutrino Physics*. CRC Press, 2020. ISBN: 978-1-315-19561-2.

[15] Y. Fukuda et al. 'Evidence for Oscillation of Atmospheric Neutrinos'. In: *Physical Review Letters* 81.8 (Aug. 1998), pp. 1562–1567. DOI: `10.1103/physrevlett.81.1562`.

[16] F. P. An et al. 'Observation of Electron-Antineutrino Disappearance at Daya Bay'. In: *Physical Review Letters* 108.17 (Apr. 2012). DOI: `10.1103/physrevlett.108.171803`.

[17] T2K Collaboration et al. 'Precise Measurement of the Neutrino Mixing Parameter θ_{23} from Muon Neutrino Disappearance in an Off-axis Beam'. In: (2014). DOI: `10.48550/ARXIV.1403.1532`. URL: `https://arxiv.org/abs/1403.1532`.

[18] A. Yu. Smirnov. *Solar neutrinos: Oscillations or No-oscillations?* 2016. DOI: `10.48550/ARXIV.1609.02386`. URL: `https://arxiv.org/abs/1609.02386`.

[19] [Online; accessed June 12, 2022]. URL: `https://legend-exp.org/`.

[20] Manfred Lindner, Tommy Ohlsson and Gerhart Seidl. 'Seesaw mechanisms for Dirac and Majorana neutrino masses'. In: *Physical Review D* 65.5 (Feb. 2002). DOI: `10.1103/physrevd.65.053014`. URL: `https://doi.org/10.1103%5C%2Fphysrevd.65.053014`.

[21] A. Boyarsky et al. 'Sterile neutrino Dark Matter'. In: *Progress in Particle and Nuclear Physics* 104 (Jan. 2019), pp. 1–45. DOI: `10.1016/j.ppnp.2018.07.004`. URL: `https://doi.org/10.1016%5C%2Fj.ppnp.2018.07.004`.

[22] Esra Bulbul et al. 'DETECTION OF AN UNIDENTIFIED EMISSION LINE IN THE STACKED X-RAY SPECTRUM OF GALAXY CLUSTERS'. In: *The Astrophysical Journal* 789.1 (June 2014), p. 13. DOI: `10.1088/0004-637x/789/1/13`.

[23] O. Urban et al. *A Suzaku Search for Dark Matter Emission Lines in the X-ray Brightest Galaxy Clusters*. 2014. DOI: `10.48550/ARXIV.1411.0050`. URL: `https://arxiv.org/abs/1411.0050`.

[24] Joshua W. Foster et al. 'Deep Search for Decaying Dark Matter with XMM-Newton Blank-Sky Observations'. In: *Physical Review Letters* 127.5 (June 2021). DOI: `10.1103/physrevlett.127.051101`. URL: `https://doi.org/10.1103%5C%2Fphysrevlett.127.051101`.

[25] A. A. Aguilar-Arevalo et al. 'Significant Excess of Electronlike Events in the MiniBooNE Short-Baseline Neutrino Experiment'. In: *Physical Review Letters* 121.22 (Nov. 2018). DOI: `10.1103/physrevlett.121.221801`. URL: `https://doi.org/10.1103%5C%2Fphysrevlett.121.221801`.

[26] J. M. Conrad and M. H. Shaevitz. *Sterile Neutrinos: An Introduction to Experiments*. 2016. DOI: `10.48550/ARXIV.1609.07803`. URL: `https://arxiv.org/abs/1609.07803`.

[27] B. Abi et al. *Deep Underground Neutrino Experiment (DUNE), Far Detector Technical Design Report, Volume II: DUNE Physics*. 2020. DOI: `10.48550/ARXIV.2002.03005`. URL: `https://arxiv.org/abs/2002.03005`.

[28] [Online; accessed Mai 13, 2022]. URL: `https://www.katrin.kit.edu/`.

[29] M. Aker et al. *KATRIN: Status and Prospects for the Neutrino Mass and Beyond*. 2022. DOI: `10.48550/ARXIV.2203.08059`. URL: `https://arxiv.org/abs/2203.08059`.

[30] M. Aker et al. 'The design, construction, and commissioning of the KATRIN experiment'. In: *Journal of Instrumentation* 16.08 (Aug. 2021), T08015. DOI: `10.1088/1748-0221/16/08/t08015`.

[31] Alexey Lokhov et al. 'Background reduction at the KATRIN experiment by the shifted analysing plane configuration'. In: *The European Physical Journal C* 82.3 (Mar. 2022). DOI: `10.1140/epjc/s10052-022-10220-4`. URL: `https://doi.org/10.1140%5C%2Fepjc%5C%2Fs10052-022-10220-4`.

[32] Jan Behrens et al. 'A pulsed, mono-energetic and angular-selective UV photoelectron source for the commissioning of the KATRIN experiment'. In: *The European Physical Journal C* 77 (2017), pp. 1–20.

[33] KATRIN Collaboration. *KATRIN design report 2004*. Tech. rep. 51.54.01; LK 01. Forschungszentrum Jülich, 2005. 245 pp. DOI: `10.5445/IR/270060419`.

[34] T. Brunst et al. 'Measurements with a TRISTAN prototype detector system at the "Troitsk nu-mass" experiment in integral and differential mode'. In: *Journal of Instrumentation* 14.11 (Nov. 2019), P11013–P11013. DOI: `10.1088/1748-0221/14/11/p11013`.

[35] D. Siegmann. 'Investigation of the Detector Response to Electrons of the TRISTAN Prototype Detectors'. Master's Thesis. Technische Universität München, 2019.

[36] S. Mertens et al. 'Sensitivity of next-generation tritium beta-decay experiments for keV-scale sterile neutrinos'. In: *Journal of Cosmology and Astroparticle Physics* 2015.02 (Feb. 2015), pp. 020–020. DOI: 10.1088/1475-7516/2015/02/020.

[37] P. Renschler. 'KESS - A new Monte Carlo simulation code for low-energy electron interactions in silicon detectors'. Ph.D. Thesis. Karlsruhe Institute of Technology, 2011.

[38] S. Mertens et al. 'A novel detector system for KATRIN to search for keV-scale sterile neutrinos'. In: *Journal of Physics G: Nuclear and Particle Physics* 46.6 (May 2019), p. 065203. DOI: 10.1088/1361-6471/ab12fe.

[39] M. Korzeczek. 'Sterile neutrino search with KATRIN – modeling and design-criteria of a novel detector system'. Ph.D. Thesis. Karlsruhe Institute of Technology, 2020.

[40] T. Fließbach. *Quantenmechanik: Lehrbuch zur theoretischen Physik 3*. Springer Spektrum, 2018. ISBN: 978-3-662-58030-1.

[41] Kwok K. Ng S.M. Sze. *Physics of Semiconductor Devices*. John Wiley & Sons, Inc., 2007. ISBN: 978-0-47 1-1 4323-9.

[42] [Online; accessed April 15, 2022]. URL: https://www.electronics-tutorials.ws/diode/diode_2.html.

[43] M. Lebert. 'Characterization of the Detector Response to Electrons and Test of a New Entrance Window Technology of Silicon Drift Detectors for the TRISTAN Project'. Master's Thesis. Technische Universität München, 2019.

[44] P. Lechner et al. 'Silicon drift detectors for high count rate X-ray spectroscopy at room temperature'. In: *Nuclear Instruments and Methods in Physics Research Section A: Accelerators, Spectrometers, Detectors and Associated Equipment* 458.1 (2001). Proc. 11th Inbt. Workshop on Room Temperature Semiconductor X- and Gamma-Ray Detectors and Associated Electronics, pp. 281–287. ISSN: 0168-9002. DOI: https://doi.org/10.1016/S0168-9002(00)00872-X.

[45] D. Spreng. 'Energy Calibration of the TRISTAN Silicon Drift Detectors'. Bachelor's Thesis. Technische Universität München, 2020.

[46] J. D. Goullon. 'Installation and comissioning of the monitor spectrometer of KATRIN'. Diplomarbeit. Karlsruher Institut für Technologie, 2010.

[47] M. Slezàk. 'Monitoring of the energy scale in the KATRIN neutrino experiment'. Doctoral Thesis. Charles University in Prague, 2015.

[48] P. King et al. 'Design and characterization of Kerberos: a 48-channel analog pulse processing and data acquisition platform'. In: *Journal of Instrumentation* 16.07 (July 2021), T07007. DOI: 10.1088/1748-0221/16/07/t07007.

[49] Doctoral Dissertation of Pietro King. 2020–2021.

[50] K. M. Altenmüller. 'Search for sterile neutrinos in β-decays'. Doktorarbeit. Technische Universität München, 2019.

[51] Filippo Schembari et al. 'SFERA: An Integrated Circuit for the Readout of X and γ -Ray Detectors'. In: *IEEE Transactions on Nuclear Science* 63 (2016), pp. 1797–1807.

[52] T. Eggert. 'Die spektrale Antwort von Silizium-Röntgendetektoren'. PhD thesis. Technische Universität München, 2004.

[53] D. Vénos et al. 'Properties of ^{83m}Kr conversion electrons and their use in the KATRIN experiment'. In: *Journal of Instrumentation* 13.02 (Feb. 2018), T02012–T02012. DOI: `10.1088/1748-0221/13/02/t02012`.

[54] M Erhard et al. 'High-voltage monitoring with a solenoid retarding spectrometer at the KATRIN experiment'. In: *Journal of Instrumentation* 9.06 (June 2014), P06022–P06022. DOI: `10.1088/1748-0221/9/06/p06022`. URL: `https://doi.org/10.1088/1748-0221/9/06/p06022`.

[55] *MPP krypton measurements*. Presentation at TRISTAN Detector Meeting. Feb. 2019.

[56] S Mertens et al. 'Characterization of silicon drift detectors with electrons for the TRISTAN project'. In: *Journal of Physics G: Nuclear and Particle Physics* 48.1 (Dec. 2020), p. 015008. DOI: `10.1088/1361-6471/abc2dc`.

[57] Jorge J. Moré. 'The Levenberg-Marquardt algorithm: Implementation and theory'. In: *Numerical Analysis*. Ed. by G. A. Watson. Berlin, Heidelberg: Springer Berlin Heidelberg, 1978, pp. 105–116. ISBN: 978-3-540-35972-2.

[58] Matthew Newville et al. *LMFIT: Non-Linear Least-Square Minimization and Curve-Fitting for Python*. Version 0.8.0. Sept. 2014. DOI: `10.5281/zenodo.11813`. URL: `https://doi.org/10.5281/zenodo.11813`.

[59] M. Descher. 'High rate systematic effects for keV sterile neutrino searches at KATRIN'. Master's Thesis. Karlsruhe Institute of Technology, 2019.

[60] M. Grundmann. *The Physics of Semiconductors An Introduction Including Nanophysics and Applications*. third. Springer International Publishing, 2016. ISBN: 978-3-319-23880-7.

[61] F. Hartmann. *Evolution of Silicon Sensor Technoloy in Particle Physics*. second. Springer International Publishing AG, 2017. ISBN: 978-3-319-64434-9.

Acknowledgements

I am sincerely grateful to all those who have supported me during the work on this thesis. Special thanks go to

- **Susanne Mertens** for the great support and interest in my progress as well as for the opportunity to write my thesis here.

- **Tim Brunst** for his supervision, albeit brief, during the first months of the research phase. Thanks for the introduction to the chair, the help with installing the software and the great and tireless willingness to answer my questions.

- **Daniel Siegmann** for the reliable and quick answers to all my questions, may I have asked them more than once. I am also thankful for the great tips and tricks in programming as well as the very understandable explanations of the physics behind the topic.

- **Frank Edzards** for taking over the supervision of Tim and for the fast, reliable and helpful answers to all my questions, especially for the quick and well-founded help when my code caused problems again.

- **Korbinian Urban** for stepping in when Daniel and Frank didn't have time and for the questions that got me on new tracks.

- **Cynthia Glas** and **Katrin Geigenberger** for the pleasant office atmosphere and the nice and interesting conversations and the many tips.

- **Philipp Rößner**, **Mathilde Wunderl** and **Matthias Wunderl** for proofreading and having my back during this time so that I could fully concentrate on the work. I am also grateful that all my friends have been so patient when I have not had time for them during writing of my master thesis.

- the entire **TRISTAN** and **KATRIN Group** for the pleasant working atmosphere and the interesting discussions and the warm welcome into the group.

- the **Max-Planck Institute for Physics** for this great opportunity to further my education.